Retrospective and Predictive Cost Adaptive Control of Space Systems

by

Nima Mohseni

A dissertation submitted in partial fulfillment
of the requirements for the degree of
Doctor of Philosophy
(Aerospace Engineering)
in The University of Michigan
2023

Doctoral Committee:

Professor Dennis S. Bernstein, Chair
Associate Professor James W. Cutler
Professor Ilya V. Kolmanovsky
Dr. Marco B. Quadrelli, NASA Jet Propulsion Laboratory

Nima Mohseni
nmohseni@umich.edu
ORCID iD: 0000-0002-2031-3763

DEDICATION

I first would like to thank my family for all their love and support and for encouraging me throughout my academic career.

I also would like to thank my advisor Professor Dennis S. Bernstein for giving me a chance at a Ph.D. when no one else would. Your support and mentorship throughout these past years not only helped me become a researcher but also helped shape me as an individual.

Finally, I would like to thank all my friends over the years. Without you all my time at Michigan would definitely not have been as fun. Your collective support throughout this experience helped me grow as a person and let me experience some unforgettable memories.

ACKNOWLEDGMENTS

This work was supported by a NASA Space Technology Graduate Research Opportunity under grant number 80NSSC20K1164.

TABLE OF CONTENTS

LIST OF FIGURES

FIGURE

LIST OF ALGORITHMS

ALGORITHM

LIST OF ACRONYMS

APPC adaptive pole placement control

BOCF block observable canonical form

DTF dereverberated transfer function

DTM dereverberated target model

LMI linear matrix inequality

MIMO multi-input multi-output

MISO multi-input single-output

MRAC model reference adaptive control

MPC model predictive control

NMP nonminimum-phase

PCAC predictive cost adaptive control

RCAC retrospective cost adaptive control

RC-MRAC retrospective cost model reference adaptive control

RLS recursive least squares

RMS root-mean-square

SISO single-input single-output

SNR signal-to-noise ratio

VRF variable-rate forgetting

ZOH zero-order-hold

ABSTRACT

As space missions become increasingly complex and autonomous, more advanced control algorithms will be needed to handle the dynamical uncertainty facing these missions. These future missions will experience unknown disturbances, unmodeled nonlinearities, time-varying parameters such as changes in mass due to fuel usage, or unknown changes in the operating environment.

In this dissertation, we explore the use of adaptive control to allow for spacecraft to adapt online to reject unknown disturbances and maintain performance under dynamic uncertainty. Specifically, we develop and apply the retrospective cost adaptive control (RCAC) and predictive cost adaptive control (PCAC) algorithms for disturbance rejection of lightly damped systems such as space telescopes and for sample gathering from small celestial bodies such as asteroids. For disturbance rejection of lightly damped systems, RCAC requires several hundred impulse response coefficients for its closed-loop target model. We introduce the idea of using a dereverberated transfer function as the modeling information for RCAC to significantly reduce the order of the target model. The resulting algorithm was successfully implemented on an acoustic disturbance rejection experiment.

Next, we consider the model reference adaptive control (MRAC) problem and develop the retrospective cost model reference adaptive control (RC-MRAC) algorithm. MRAC methods allow for robotic systems to adjust to changes while attempting to follow a desired reference trajectory from a predetermined reference model. RC-MRAC enables reference model following of arbitrary linear systems as long as the relative degree, leading numerator coefficient, system order, and nonminimum-phase zeros are known.

We then focus on PCAC, which combines online model identification with model predictive control (MPC). For online identification, PCAC relies on a variable-rate forgetting (VRF) factor to track time-varying parameters. We develop a new VRF factor using the F-test that is more robust to noise and provides faster parameter convergence after a system change compared to the standard constant-rate forgetting factor used in practice. The F-test based VRF factor is a variation of the standard VRF factor used in PCAC. We demonstrate the applicability of PCAC for disturbance rejection of large truss structures representative of space telescopes subject to harmonic and broadband disturbances under aliasing and modal folding.

Finally, we focus on the small celestial body surface sampling problem, where a spacecraft

with a robotic sampling arm descends onto the surface of an asteroid with unknown properties and must maintain a desired contact force to gather a sample before leaving the surface. The contact dynamics of this problem are nonlinear, nonsmooth, and unknown prior to contact. We demonstrate that PCAC can be used to augment a nominal robust controller to improve the overall sampling performance of the spacecraft for a wide variety of surface properties. We then show that the online identification combined with the VRF factor in PCAC can allow the spacecraft to perform multiple sampling maneuvers in regions with different surface properties without loss of performance.

CHAPTER 1

Introduction

1.1 Background and Motivation

In recent years there has been renewed interest in space exploration with spacecraft and robotic missions that push past the capabilities of past missions to accomplish greater scientific goals. Future missions will need to account for increasing dynamical uncertainty due to unknown surface properties of bodies such as the icy surface of Europa or unknown disturbances that can affect the pointing accuracy of large space telescopes. There will also be unmodeled nonlinearities from structural joints, time-varying parameters such as changing mass due to fuel usage, changing environments, as well as sensor and actuator failures. Higher resolution images of the universe will require larger and more complex telescopes, leading to structures that may need to be assembled in orbit with many vibrational modes that cannot be experimentally modeled on Earth.

Vibration suppression for large flexible structures such as space telescopes is a longstanding area of research spanning many decades [1, 2, 3, 4, 5, 6, 7]. For large space structures the launch constraints on mass inevitably lead to low damping and thus high susceptibility to disturbances [8]. The infinite-dimensional nature of continuum bodies has motivated considerable research based on partial differential equations [9]. From a practical perspective, finite-dimensional models obtained from finite-element modeling are needed for computation; however, the use of lumped models entails "spillover," that is, the inadvertent excitation of truncated modes [8, 10].

The issue of modal truncation is exacerbated by uncertainty arising from model errors and sensitivities. For example, modal properties are highly sensitive to boundary conditions, and the need for 1-g testing of lightweight structures designed for a 0-g environment leads to further modeling errors. This means that, at least to some extent, on-orbit system identification is unavoidable.

Although laboratory testing can be performed in a setting that is largely free of disturbances, a realistic challenge of system identification in an operational scenario is the unavoidable presence of disturbances. These disturbances may arise from onboard equipment that cannot be shut down (for example, cryocoolers, control-moment gyros, or flywheels for energy storage), or due to

environmental sources, such as solar pressure, magnetically induced torques, and thermal gradients.

For space robotics missions such as surface sampling missions, the objective is to bring a spacecraft with a sampler in contact with the surface of a celestial body and maintain a desired contact force in order to capture a sample from the surface [11, 12]. The resulting samples are used to further scientific knowledge about the origins of the solar system and universe. Recent missions such as OSIRIS-REx, Hayabusa, and Hayabusa2 have demonstrated the feasibility of such missions and have laid the groundwork for more complex sample return missions as shown by sampling mission concepts using shape memory alloy and harpoon sampling mechanisms [13, 14].

Despite recent successes, surface sampling remains a challenging problem. Before contact with the surface, surface properties such as the compliance are uncertain. Additional challenges arise due to unknown nonlinear contact dynamics such as hysteretic effects, and the inability to use the spacecraft thrusters to augment the contact force. Therefore, the controller must be designed to be robust to a wide variety of surface properties. Additionally, there is an inherent trade-off between robustness and control performance, which may limit the possible scope of the mission to safer, well known and modeled scenarios. If the true surface properties are outside expectations, mission performance will be adversely affected. This was evidenced by the Philae lander, which attempted to land on the comet 67P/Churyumov–Gerasimenko but, due to the surface being softer than expected, instead bounced off of the surface and landed in the shadow of the comet, prematurely ending the planned 10-year-long mission [15].

These difficulties cannot all be planned for, and necessitate a need for autonomy to allow the spacecraft to adjust online without having to wait for commands from Earth or separate on-orbit system identification. One possibility for alleviating these issues is to use controllers that can learn online or adapt. These controllers, called adaptive controllers, can be divided into two categories: direct adaptive control, and indirect adaptive control [16, 17, 18, 19]. In direct adaptive control, the objective is to adjust a controller online without needing an accurate prior model of the system. The parameters of the controller are directly updated based on incoming sensor and performance measurements and the model of the system is not updated. For direct adaptive control, nonminimum-phase (NMP) systems require special consideration. These systems contain zeros outside the unit disk and limit the achievable controller performance [20]. NMP systems also make development of direct adaptive control methods difficult, since these methods tend to cancel unknown NMP zeros with a controller pole, leading to instability. Additionally, sampling a minimum-phase continuous-time system with relative degree greater than 2 leads to NMP discrete-time dynamics [21]. In indirect adaptive control, a model of the system being controlled is identified online which is then used to update the controller coefficients. By identifying a model, indirect adaptive control methods avoid the difficulties posed by NMP systems at the cost of needing to choose a set of basis functions for the model and increased computational cost due to the model

identification.

This dissertation focuses on two adaptive control techniques, retrospective cost adaptive control (RCAC) and predictive cost adaptive control (PCAC). RCAC is a direct adaptive control algorithm developed originally for active noise control experiments [22]. RCAC can perform disturbance rejection and command following with minimal modeling information [23] given in a filter G_{f}. Being a direct adaptive control method, RCAC requires knowledge of the NMP zeros of the system which must be incorporated in the filter G_{f}. The contribution of this dissertation is the development of alternative methods for the creation of G_{f} for disturbance rejection of lightweight, high-order, lightly damped structures [24, 25]. RCAC is also extended to the model reference adaptive control (MRAC) problem where a novel algorithm called retrospective cost model reference adaptive control (RC-MRAC) is developed [26, 27]. In the MRAC problem, we wish to have the output of an uncertain system follow the response of a given reference system. The MRAC problem has had vast and varied applications and is one of the original uses of adaptive control [28, 29, 30, 31].

PCAC is an indirect adaptive control that combines concurrent online recursive least squares (RLS) identification with model predictive control (MPC) developed in [32, 33]. MPC has been widely developed for diverse applications [34, 35, 36, 37, 38] and, perhaps with the exception of PID control, is the most widely used control methodology. PCAC employs an input-output model structure whose coefficients are estimated online using recursive least squares. The identified model is then recast as a state space model using a block observable canonical form (BOCF) whose state is an explicit function of past inputs, past outputs, and the current estimated model coefficients. Since the state of the BOCF model is known exactly at each time step, output-feedback MPC can be implemented without the need for an observer.

A key aspect of PCAC is the use of a variable-rate forgetting (VRF) factor in the identification portion of the algorithm. To track time-varying parameters, RLS can incorporate a forgetting factor λ, which discounts past data. Choosing an appropriate λ is typically done through trial and error or, when the identification is performed offline, maximum likelihood methods. Typical values of λ are between 0.98 and 1 [39, 40] When a parameter change occurs and forgetting is not enabled, RLS converges slowly to the new parameter values. On the other hand, the use of forgetting when parameters do not change and the data is not persistently exciting can lead to divergence of the singular values of the RLS covariance matrix [41]. In the context of adaptive control, instability of RLS leads to instability of the controller and catastrophic blow-up. In contrast with constant-rate forgetting, VRF allows the forgetting factor to change during operation. VRF versions of RLS are given in [42, 43, 44]. These formulations were extended in [45] to include criteria for setting the level of forgetting at each step while maintaining convergence and consistency. Increasing interest in VRF is reflected in [46, 47, 48]. The contribution of this work is the development of new VRF factor based on a statistical test called the F-Test, that is more robust to noise and spurious forgetting

compared to past VRF methods [49, 45, 50]. Additionally, the development of the new forgetting factor enabled the use of PCAC for disturbance rejection of large, lightweight structures similar to space telescopes as shown in [51]. For space robotics applications, PCAC was applied to a celestial body surface sampling mission where the surface was unknown before contact. PCAC was used to augment a previously developed robust controller to improve performance over a wide variety of surface properties. The new VRF factor enabled the spacecraft to sample multiple regions of the celestial body with different unknown surface properties without loss in performance [52, 53].

1.2 Dissertation Outline

This dissertation is organized as follows.

Chapter 2 Summary

Chapter 2 presents the framework and development of the main algorithms used in this dissertation. An overview of RLS, RCAC, and PCAC is presented.

Chapter 3 Summary

Chapter 3 focuses on adaptive feedback disturbance rejection for lightly damped structures using RCAC. RCAC uses a target model of the closed-loop dynamics in order to enable controller adaptation. The target model captures specific features of the dynamics of the structure; in the single-input single-output (SISO) case, this information consists of the sign of the leading numerator coefficient, relative degree, and nonminimum-phase zeros of the discretized dynamics. The chapter investigates the feasibility of using a dereverberated transfer function (DTF) as the target model for harmonic disturbance rejection with unknown disturbances. In particular, the dereverberated target model (DTM) obtained by magnitude and phase averaging captures the magnitude and phase trend of the structure but ignores resonances and anti-resonances, thus providing a low-order target model for controller adaptation. The robustness of RCAC is investigated with the target model given by a DTF based on a nominal model with erroneous damping ratio. The technique is implemented experimentally on an acoustic noise control setup.

Chapter 4 Summary

Chapter 4 presents a novel approach to model reference adaptive control inspired by the adaptive pole placement control (APPC) of Elliot and based on RC-MRAC. RC-MRAC is applicable to NMP systems assuming that the NMP zeros are known. Under this assumption, the advantage of RC-MRAC is a reduced need for persistency. The chapter compares APPC and RC-MRAC under

various levels of persistency in the command for minimum-phase and NMP systems. It is shown numerically that the model-following performance of RC-MRAC is less sensitive to the persistency of the command compared to APPC at the cost of knowledge of the NMP zeros. RC-MRAC is also shown to be applicable for disturbance rejection under unknown harmonic disturbances.

Chapter 5 Summary

Chapter 5 develops a variable-rate forgetting factor for recursive least squares for parameter identification of time-varying systems. The variable-rate forgetting factor uses the F-test to compare short- and long-term variances of the one-step prediction errors of RLS. If the short-term error variance is statistically larger than the long-term error variance, then it is assumed that the underlying parameters have changed and forgetting is required. The level of forgetting is proportional to how far the ratio of the short-term and long-term error variances deviate from the expected ratio given by the F-distribution. RLS with F-test variable-rate forgetting (RLS/FTVRF) is shown to generalize an existing variable-rate forgetting factor that uses a ratio of the root-mean-square (RMS) performance error and noise standard deviation. The approach is applied to a parameter identification task and is compared to a constant-rate forgetting factor and the RMS performance error and noise standard-deviation-based forgetting factor.

Chapter 6 Summary

Chapter 6 considers indirect adaptive control of flexible structures under harmonic and broad-band disturbances. Limited prior modeling information is assumed, and system identification with an input-output model structure is performed online in the presence of the exogenous disturbance. By realizing the input-output model structure in block observable canonical form, the full state is available, which facilitates output-feedback control without the need for an observer. The control input is determined by MPC using quadratic programming for receding horizon optimization. The resulting sampled-data controller is implemented at a fixed sample rate, where the frequencies of some of the modes may lie above the Nyquist rate, thus emulating spillover. The approach is applied to a truss structure with 16 lightly damped modes.

Chapter 7 Summary

Chapter 7 develops an adaptive force-control augmentation for small celestial body sampling for a variety of surface properties. The control algorithm consists of a nominal robust controller augmented with an adaptive controller combined with feedback linearization. When a spacecraft makes contact with the surface, it must maintain a desired contact force in order to capture a sample. The properties of the surface are unknown or uncertain before contact with the surface is made.

Since the nominal robust controller may have poor performance in some surface property regimes, the goal is to improve performance using an adaptive controller. The adaptive controller performs system identification online to create an input-output model of the feedback-linearized system. From the input-output model, a block-observable canonical form is realized, and the control input augmentation is determined by MPC. The resulting augmentation is added to the input of the robust controller to improve the closed-loop performance and maintain a desired contact force despite the unknown surface properties. The approach is applied to a variety of surface properties with linear and nonlinear contact models and multiple surface sampling maneuvers.

CHAPTER 2

Preliminaries

In this chapter we state the equations of RCAC and PCAC which will be used throughout the dissertation. The algorithms will be presented with respect to a specific problem setup that is applicable to the standard use of the algorithm. Additionally, the RLS algorithm is presented, which is an important component in both RCAC and PCAC. A modification to RLS incorporating a variable-rate forgetting factor is also presented.

2.1 Recursive Least Squares

RLS is widely used for parameter estimation and adaptive control [18, 16]. In many estimation and control problems, we would like to find coefficients $\theta \in \mathbb{R}^{l_\theta}$ such that

$$y_k = \phi_k \theta, \tag{2.1}$$

where $y_k \in \mathbb{R}^{l_y}$ is some measurement or output, and $\phi_k \in \mathbb{R}^{l_y \times l_\theta}$ is a regressor containing some function of past measurements and control inputs [54]. One method of solving this problem is to collect a n data points and solve a regularized batch least squares problem by finding $\hat{\theta}$ that minimizes

$$\begin{aligned} J(\hat{\theta}) &= \sum_{i=1}^{n} (y_i - \phi_i \hat{\theta})^{\mathrm{T}} (y_i - \phi_i \hat{\theta}) + \hat{\theta}^{\mathrm{T}} R_\theta \hat{\theta} \\ &= (Y - \Phi \hat{\theta})^{\mathrm{T}} (Y - \Phi \hat{\theta}) + \hat{\theta}^{\mathrm{T}} R \hat{\theta} \end{aligned} \tag{2.2}$$

where

$$Y = \Phi \hat{\theta}, \tag{2.3}$$

$$Y \triangleq \begin{bmatrix} y_1 \\ y_2 \\ \vdots \\ y_n \end{bmatrix}, \ \Phi \triangleq \begin{bmatrix} \phi_1 \\ \phi_2 \\ \vdots \\ \phi_n \end{bmatrix}, \tag{2.4}$$

and $R_\theta \in \mathbb{R}^{l_\theta \times l_\theta}$ is a positive-definite matrix. The solution is given by

$$\hat{\theta}^* = (\Phi^{\mathrm{T}}\Phi + R_\theta)^{-1}\Phi^{\mathrm{T}}Y, \tag{2.5}$$

which requires an $l_\theta \times l_\theta$ inverse leading to a computational complexity of $O(l_\theta^3)$.

For real-time applications, we would like to use an algorithm with less computational complexity and update our estimate of θ at each measurement step rather than in a batch formulation. This can be accomplished using RLS. RLS attempts find θ to minimize the following cumulative cost function at each step k

$$J_k(\hat{\theta}) \triangleq \sum_{i=1}^{k} \lambda^{k-i}[e_i(\hat{\theta})^{\mathrm{T}} e_i(\hat{\theta})] + \lambda^k(\hat{\theta} - \theta_0)^{\mathrm{T}} P_0^{-1}(\hat{\theta} - \theta_0), \tag{2.6}$$

where

$$e_i(\hat{\theta}) \triangleq y_i - \phi_i\hat{\theta}, \tag{2.7}$$

$\theta_0 \in \mathbb{R}^{l_\theta}$ is an initial estimate of θ, $P_0 \in \mathbb{R}^{l_\theta \times l_\theta}$ is a positive-definite covariance matrix representing the initial uncertainty in the error $\theta - \theta_0$, and $\lambda \in (0, 1]$ is a forgetting factor allowing for discounting of past data in order to track time-varying parameters. The solution is given by the following recursive update of $\hat{\theta}_k$ and P_k

$$\hat{\theta}_{k+1} = \hat{\theta}_k + P_k\phi_k^{\mathrm{T}}\left(\lambda I_{l_y} + \phi_k P_k \phi_k^{\mathrm{T}}\right)^{-1} e_k(\hat{\theta}_k), \tag{2.8}$$

$$P_{k+1} = \frac{1}{\lambda}P_k - \frac{1}{\lambda}P_k\phi_k^{\mathrm{T}}\left(\lambda I_{l_y} + \phi_k P_k \phi_k^{\mathrm{T}}\right)^{-1}\phi_k P_k. \tag{2.9}$$

The resulting algorithm has a computational complexity of $O(l_\theta^2)$ and the parameter estimate θ can be updated as data is measured instead of in batch updates.

2.1.1 Variable-Rate Forgetting

To track time-varying parameters, RLS includes a forgetting factor λ, which discounts past data. Choosing an appropriate λ is typically done through trial and error or, when the identification

is performed offline, maximum likelihood methods. Typical values of λ are between 0.98 and 1 [39, 40]. When a parameter change occurs and forgetting is not enabled, RLS converges slowly to the new parameter values. On the other hand, the use of forgetting when parameters do not change and the data is not persistently exciting can lead to divergence of the singular values of the RLS covariance matrix P_k [41]. In the context of adaptive control, instability of RLS leads to instability of the controller and catastrophic blow-up.

In contrast with constant-rate forgetting, VRF allows the forgetting factor to change during operation. VRF versions of RLS are given in [42, 43, 44], These formulations were extended in [45] to include criteria for setting the level of forgetting at each step while maintaining convergence and consistency.

To generalize (2.6) such that λ can vary as a function of k, let $\beta_k > 0$ and define

$$\rho_k \triangleq \prod_{i=0}^{k} \beta_i. \tag{2.10}$$

As shown in [45], the unique global minimizer of the cost function

$$J_k(\theta) \triangleq \sum_{i=0}^{k} \frac{\rho_i}{\rho_k} e_i^{\mathrm{T}}(\theta) e_i(\theta) + \frac{1}{\rho_k} (\theta - \theta_0)^{\mathrm{T}} P_0^{-1} (\theta - \theta_0) \tag{2.11}$$

is given by

$$\theta_{k+1} = \theta_k + P_{k+1} \phi_k^{\mathrm{T}} (y_k - \phi_k \theta_k) \tag{2.12}$$

where

$$P_{k+1} = L_k - L_k \phi_k^{\mathrm{T}} (I_p + \phi_k L_k \phi_k^{\mathrm{T}})^{-1} \phi_k L_k \tag{2.13}$$

$$L_k \triangleq \beta_k P_k \tag{2.14}$$

The variable rate forgetting factor is then defined as $\lambda_k \triangleq \beta_k^{-1}$. (2.12)-(2.14) are the recursive least squares with variable-rate forgetting (RLS-VRF) equations.

2.2 Retrospective Cost Adaptive Control

In this section we present RCAC and the standard problem setup that RCAC attempts to solve.

2.2.1 Problem Setup

Consider the discrete-time adaptive control problem given in Figure 2.1. RCAC attempts to update the controller $G_{\mathrm{c}}(\mathbf{q}, \theta_k)$ in order to minimize the performance measurement z_k, given the sensor measurements y_k, control inputs u_k.

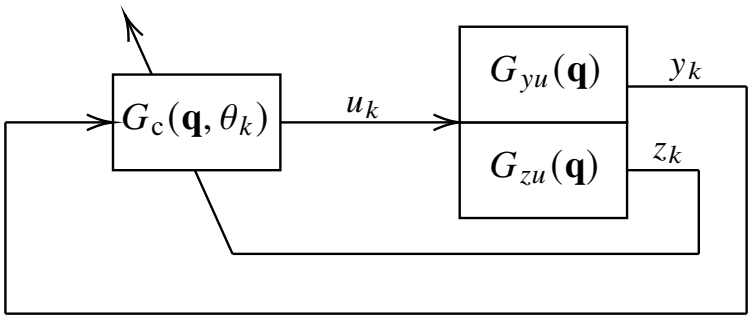

Figure 2.1: RCAC standard problem.

2.2.2 Retrospective Cost Adaptive Control Algorithm

For the current vector θ_k of controller coefficients, $G_{\mathrm{c}}(\mathbf{q}, \theta_k)$ is realized by the linear, time-varying, input-output model

$$u_k = \sum_{i=1}^{n_{\mathrm{c}}} P_{i,k} u_{k-i} + \sum_{i=1}^{n_{\mathrm{c}}} Q_{i,k} y_{k-i}, \tag{2.15}$$

where $P_{i,k} \in \mathbb{R}^{l_u \times l_u}$, $Q_{i,k} \in \mathbb{R}^{l_u \times l_y}$, and n_{c} is the controller order. The startup protocol for (2.15) is given by

$$u_k = \begin{cases} 0, & k < k_{\mathrm{w}}, \\ \Phi_k \theta_k, & k \geq k_{\mathrm{w}}, \end{cases} \tag{2.16}$$

where the regressor matrix Φ_k is defined as

$$\Phi_k \triangleq \begin{bmatrix} u_{k-1} \\ \vdots \\ u_{k-n_{\mathrm{c}}} \\ y_{k-1} \\ \vdots \\ y_{k-n_{\mathrm{c}}} \end{bmatrix}^{\mathrm{T}} \otimes I_{l_u} \in \mathbb{R}^{l_u \times l_\theta}, \tag{2.17}$$

$k_w \geq n_c$ is the number of steps to wait until Φ_k is populated with data, θ_k is the controller coefficient vector defined by

$$\theta_k \triangleq \operatorname{vec}\begin{bmatrix} P_{1,k} & \cdots & P_{n_c,k} & Q_{1,k} & \cdots & Q_{n_c,k} \end{bmatrix}^{\mathrm{T}} \in \mathbb{R}^{l_\theta}, \tag{2.18}$$

and $l_\theta \triangleq n_c l_u (l_u + l_y)$.

The retrospective performance variable is defined by

$$\hat{z}_k(\hat{\theta}) \triangleq z_k - G_f(\mathbf{q})(u_k - \Phi_k \hat{\theta}), \tag{2.19}$$

where $\hat{\theta}$ is the controller coefficient vector to be optimized, and $G_f(\mathbf{q}) \in \mathbb{R}^{l_z \times l_u}$ is a filter. G_f plays the role of the target model for a closed-loop transfer function which contains the same leading numerator coefficient sign, NMP zeros, and relative degree as the plant. Defining the filtered quantities $u_{f,k} \triangleq G_f(\mathbf{q})u_k$ and $\Phi_{f,k} \triangleq G_f(\mathbf{q})\Phi_k$, (2.19) can be written as

$$\hat{z}_k(\hat{\theta}) = z_k - (u_{f,k} - \Phi_{f,k}\hat{\theta}). \tag{2.20}$$

The controller coefficient vector $\hat{\theta}$ is updated by minimizing the cost function

$$J_k(\hat{\theta}) \triangleq \sum_{i=1}^{k} \lambda^{k-i}[\hat{z}_i(\hat{\theta})^{\mathrm{T}} R_z \hat{z}_i(\hat{\theta}) + (\Phi_i \hat{\theta})^{\mathrm{T}} R_u (\Phi_i \hat{\theta})] + \lambda^k (\hat{\theta} - \theta_0)^{\mathrm{T}} R_\theta (\hat{\theta} - \theta_0) \tag{2.21}$$

where $\lambda \in (0, 1]$ is the forgetting factor, $R_\theta \in \mathbb{R}^{l_\theta \times l_\theta}$ and $R_z \in \mathbb{R}^{l_z \times l_z}$ are positive definite, and $R_u \in \mathbb{R}^{l_u \times l_u}$ is positive semidefinite. The cost (2.21) is minimized with respect to $\hat{\theta}$ using RLS.

The update law for the controller coefficient vector is then given by

$$\theta_{k+1} = \theta_k - P_k \begin{bmatrix} \Phi_{f,k} \\ \Phi_k \end{bmatrix}^{\mathrm{T}} \left(\lambda \begin{bmatrix} R_z & 0 \\ 0 & R_u \end{bmatrix}^{-1} + \begin{bmatrix} \Phi_{f,k} \\ \Phi_k \end{bmatrix} P_k \begin{bmatrix} \Phi_{f,k} \\ \Phi_k \end{bmatrix}^{\mathrm{T}} \right)^{-1} \left(\begin{bmatrix} \Phi_{f,k} \\ \Phi_k \end{bmatrix} \theta_k + \begin{bmatrix} z_k - u_{f,k} \\ 0 \end{bmatrix} \right) \tag{2.22}$$

where

$$P_{k+1} = \frac{1}{\lambda} P_k - \frac{1}{\lambda} P_k \begin{bmatrix} \Phi_{f,k} \\ \Phi_k \end{bmatrix}^{\mathrm{T}} \left(\lambda \begin{bmatrix} R_z & 0 \\ 0 & R_u \end{bmatrix}^{-1} + \begin{bmatrix} \Phi_{f,k} \\ \Phi_k \end{bmatrix} P_k \begin{bmatrix} \Phi_{f,k} \\ \Phi_k \end{bmatrix}^{\mathrm{T}} \right)^{-1} \begin{bmatrix} \Phi_{f,k} \\ \Phi_k \end{bmatrix} P_k \tag{2.23}$$

and $P_0 = R_\theta^{-1}$ [54]. The RLS update law has a computational complexity of $O(l_\theta^2)$.

2.3 Predictive Cost Adaptive Control

In this section we present PCAC and the problem setup that PCAC attempts to solve.

2.3.1 Problem Setup

Consider the discrete-time adaptive control problem given in Figure 2.2. PCAC attempts to find control inputs u_k such that the sensor measurements y_k follow a desired command r_k. At each time step, PCAC identifies a state space realization $\hat{A}_k, \hat{B}_k, \hat{C}, \hat{x}_k$ of $G_{yu}(\mathbf{q})$ using past control inputs and measurements. This realization is then used in MPC to generate a control input.

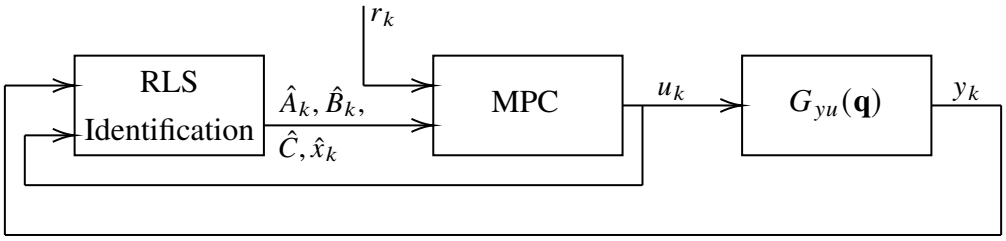

Figure 2.2: PCAC standard problem.

2.3.2 Predictive Cost Adaptive Control Algorithm

PCAC combines online identification using RLS with output-feedback MPC. These operations are described below.

2.3.2.1 RLS Identification

Consider the multi-input multi-output (MIMO) input-output model

$$\hat{y}_k = -\sum_{i=1}^{\hat{n}} \hat{F}_i y_{k-i} + \sum_{i=1}^{\hat{n}} \hat{G}_i u_{k-i}, \tag{2.24}$$

where $k \geq 0$ is the time step, $\hat{n} \geq 1$ is the data window for identification, $\hat{F}_i \in \mathbb{R}^{p\times p}$ and $\hat{G}_i \in \mathbb{R}^{p\times m}$ are the estimated model coefficients, and $u_k \in \mathbb{R}^{m\times 1}$, $y_k \in \mathbb{R}^{p\times 1}$, and $\hat{y}_k \in \mathbb{R}^{p\times 1}$ are the inputs, outputs and predicted outputs at step k.

To estimate the coefficients $\hat{F}_i$ and $\hat{G}_i$ online, we use RLS with variable-rate forgetting [45]. RLS is used to minimize the cumulative cost

$$J_k(\hat{\theta}) = \sum_{i=0}^{k} \frac{\rho_i}{\rho_k} z_i^{\mathrm{T}}(\hat{\theta}) z_i(\hat{\theta}) + \frac{1}{\rho_k}(\hat{\theta} - \theta_0)^{\mathrm{T}} P_0^{-1}(\hat{\theta} - \theta_0), \tag{2.25}$$

where $\rho_k \triangleq \prod_{j=0}^{k} \lambda_j^{-1} \in \mathbb{R}$, $\lambda_k \in (0, 1]$ is the forgetting factor, $P_0 \in \mathbb{R}^{[\hat{n}p(m+p)]\times[\hat{n}p(m+p)]}$ is positive definite, and $\theta_0 \in \mathbb{R}^{[\hat{n}p(m+p)]\times 1}$ is the initial estimate of the coefficient vector. The performance variable $z_i(\hat{\theta}) \in \mathbb{R}^{p\times 1}$ is defined as

$$z_k(\hat{\theta}) \triangleq y_k + \sum_{i=1}^{\hat{n}} \hat{F}_i y_{k-i} - \sum_{i=1}^{\hat{n}} \hat{G}_i u_{k-i}, \tag{2.26}$$

where the vector $\hat{\theta} \in \mathbb{R}^{[\hat{n}p(m+p)]\times 1}$ of coefficients to be estimated is defined by

$$\hat{\theta} \triangleq \operatorname{vec}\begin{bmatrix} \hat{F}_1 & \cdots & \hat{F}_{\hat{n}} & \hat{G}_1 & \cdots & \hat{G}_{\hat{n}} \end{bmatrix}. \tag{2.27}$$

Defining the regressor matrix $\phi_k \in \mathbb{R}^{p\times[\hat{n}p(m+p)]}$ by

$$\phi_k \triangleq \begin{bmatrix} -y_{k-1}^{\mathrm{T}} & \cdots & -y_{k-\hat{n}}^{\mathrm{T}} & u_{k-1}^{\mathrm{T}} & \cdots & u_{k-\hat{n}}^{\mathrm{T}} \end{bmatrix} \otimes I_p, \tag{2.28}$$

the performance variable can then be written as

$$z_k(\hat{\theta}) = y_k - \phi_k \hat{\theta}. \tag{2.29}$$

The global minimizer $\theta_{k+1} \triangleq \operatorname{argmin}_{\hat{\theta}} J_k(\hat{\theta})$ is computed by RLS as

$$L_k = \lambda_k^{-1} P_k \tag{2.30}$$

$$P_{k+1} = L_k - L_k \phi_k^{\mathrm{T}} (I_p + \phi_k L_k \phi_k^{\mathrm{T}})^{-1} \phi_k L_k \tag{2.31}$$

$$\theta_{k+1} = \theta_k + P_{k+1} \phi_k^{\mathrm{T}} (y_k - \phi_k \hat{\theta}), \tag{2.32}$$

where $\theta_{k+1} = \operatorname{vec}\begin{bmatrix} \hat{F}_{1,k+1} & \cdots & \hat{F}_{\hat{n},k+1} & \hat{G}_{1,k+1} & \cdots & \hat{G}_{\hat{n},k+1} \end{bmatrix}$.

The VRF factor λ_k used is developed in [49] and Chapter 5 and is given by

$$\lambda_k = \frac{1}{1 + \eta g(z_{k-\tau_{\mathrm{d}}}, \ldots, z_k) \mathbf{1}[g(z_{k-\tau_{\mathrm{d}}}, \ldots, z_k)]} \tag{2.33}$$

where $\mathbf{1} : \mathbb{R} \to \{0, 1\}$ is the unit step function, and

$$g(z_{k-\tau_d}, \ldots, z_k) \triangleq \sqrt{\frac{\tau_{\mathrm{n}}}{\tau_{\mathrm{d}}} \frac{\operatorname{tr}\left(\Sigma_{\tau_{\mathrm{n}}}(z_{k-\tau_{\mathrm{n}}}, \ldots, z_k) \Sigma_{\tau_{\mathrm{d}}}(z_{k-\tau_{\mathrm{d}}}, \ldots, z_k)^{-1}\right)}{c}} - \sqrt{f}, \tag{2.34}$$

where $\eta > 0$ and $p \leq \tau_{\mathrm{n}} < \tau_{\mathrm{d}}$ represent numerator and denominator window lengths, respectively.

In (2.34), Σ_{τ_n} and $\Sigma_{\tau_\mathrm{d}} \in \mathbb{R}^{p\times p}$ are the sample variances of the respective window lengths, c is a constant given by

$$a \triangleq \frac{(\tau_\mathrm{n}+\tau_\mathrm{d}-p-1)(\tau_\mathrm{d}-1)}{(\tau_\mathrm{d}-p-3)(\tau_\mathrm{d}-p)},\ b \triangleq 4+\frac{(p\tau_\mathrm{n}+2)}{(a-1)},$$
$$c \triangleq \frac{p\tau_\mathrm{n}(b-2)}{b(\tau_\mathrm{d}-p-1)}, \tag{2.35}$$

with $f \triangleq F^{-1}_{p\tau_\mathrm{n},\,b}(1-\alpha)$ being a thresholding constant, where $F^{-1}_{p\tau_\mathrm{n},\,b}(x)$ is the inverse cumulative distribution function of the F-distribution with degrees of freedom $p\tau_\mathrm{n}$ and b, and α is the significance level [55]. By choosing $\tau_\mathrm{d} >> \tau_\mathrm{n}$, Σ_{τ_d} approximates the long-term variance of z_k while Σ_{τ_n} approximates the short-term variance of z_k. Therefore, when $g(z_{k-\tau_d},\ldots,z_k) > 0$, the short-term variance is statistically larger than the long-term variance. In particular, (2.33) suspends forgetting when the short-term variance is statistically smaller than the long-term variance, preventing forgetting in RLS due to sensor noise, and enabling forgetting when the magnitude of the identification error increases.

For receding-horizon control, the input-output model (2.24) is written as the block observable canonical form state-space realization

$$x_{1|k} \triangleq \hat{A}_k\hat{x}_k + \hat{B}_k u_k, \tag{2.36}$$
$$y_k = \hat{C}\hat{x}_k, \tag{2.37}$$

where $x_{1|k} \in \mathbb{R}^{\hat{n}p}$ is the one-step predicted state, $\hat{x}_k \triangleq \begin{bmatrix}\hat{x}_{1,k}^\mathrm{T} & \cdots & \hat{x}_{\hat{n},k}^\mathrm{T}\end{bmatrix}^\mathrm{T} \in \mathbb{R}^{\hat{n}p}$ is the state estimate,

and

$$\hat{x}_{1,k} \triangleq y_k, \tag{2.38}$$

$$\hat{x}_{i,k} \triangleq -\sum_{j=1}^{\hat{n}-i+1} \hat{F}_{i+j-1,k+1} y_{k-j} + \sum_{j=1}^{\hat{n}-i+1} \hat{G}_{i+j-1,k+1} u_{k-j}, \quad i = 2, \ldots, \hat{n} \tag{2.39}$$

$$\hat{A}_k \triangleq \begin{bmatrix} -\hat{F}_{1,k+1} & I_p & \cdots & \cdots & 0_{p\times p} \\ \vdots & 0_{p\times p} & \ddots & & \vdots \\ \vdots & \vdots & \ddots & \ddots & 0_{p\times p} \\ \vdots & \vdots & & \ddots & I_p \\ -\hat{F}_{\hat{n},k+1} & 0_{p\times p} & \cdots & \cdots & 0_{p\times p} \end{bmatrix}, \tag{2.40}$$

$$\hat{B}_k \triangleq \begin{bmatrix} \hat{G}_{1,k+1} \\ \hat{G}_{2,k+1} \\ \vdots \\ \hat{G}_{\hat{n},k+1} \end{bmatrix}, \tag{2.41}$$

$$\hat{C} \triangleq \begin{bmatrix} I_p & 0_{p\times p} & \cdots & 0_{p\times p} \end{bmatrix}, \tag{2.42}$$

2.3.2.2 Model Predictive Control

The ℓ-step predicted output of (2.37) for a sequence of ℓ future controls is given by

$$Y_{1|k,l} = \hat{\Gamma}_{k,\ell} x_{1|k} + \hat{T}_{k,\ell} U_{1|k,\ell}, \tag{2.43}$$

where

$$Y_{1|k,\ell} \triangleq \begin{bmatrix} y_{1|k} \\ \vdots \\ y_{\ell|k} \end{bmatrix} \in \mathbb{R}^{\ell p}, \quad U_{1|k,\ell} \triangleq \begin{bmatrix} u_{1|k} \\ \vdots \\ u_{\ell|k} \end{bmatrix} \in \mathbb{R}^{\ell m}, \tag{2.44}$$

and $\hat{\Gamma}_{k,\ell} \in \mathbb{R}^{\ell p \times \hat{n} p}$ and $\hat{T}_{k,\ell} \in \mathbb{R}^{\ell p \times \ell m}$ are

$$\hat{\Gamma}_{k,\ell} \triangleq \begin{bmatrix} \hat{C} \\ \hat{C}\hat{A}_k \\ \vdots \\ \hat{C}\hat{A}_k^{\ell-1} \end{bmatrix}, \tag{2.45}$$

$$\hat{T}_{k,\ell} \triangleq \begin{bmatrix} 0_{p\times m} & \cdots & \cdots & \cdots & \cdots & \cdots & 0_{p\times m} \\ \hat{H}_{k,1} & 0_{p\times m} & \cdots & \cdots & \cdots & \cdots & 0_{p\times m} \\ \hat{H}_{k,2} & \hat{H}_{k,1} & 0_{p\times m} & \cdots & \cdots & \cdots & 0_{p\times m} \\ \hat{H}_{k,3} & \hat{H}_{k,2} & \hat{H}_{k,1} & 0_{p\times m} & \cdots & \cdots & 0_{p\times m} \\ \hat{H}_{k,4} & \hat{H}_{k,3} & \hat{H}_{k,2} & \ddots & \ddots & & \vdots \\ \vdots & \vdots & \vdots & \ddots & \ddots & \ddots & 0_{p\times m} \\ \hat{H}_{k,\ell-1} & \hat{H}_{k,\ell-2} & \hat{H}_{k,\ell-3} & \cdots & \hat{H}_{k,2} & \hat{H}_{k,1} & 0_{p\times m} \end{bmatrix}, \tag{2.46}$$

where $\hat{H}_{k,i} \in \mathbb{R}^{p\times m}$ is defined by $\hat{H}_{k,i} \triangleq \hat{C}\hat{A}_k^{i-1}\hat{B}_k$.

Let $\mathcal{R}_{k,\ell} \triangleq \begin{bmatrix} r_{k+1}^{\mathrm{T}} \cdots r_{k+\ell}^{\mathrm{T}} \end{bmatrix}^{\mathrm{T}} \in \mathbb{R}^{\ell p_{\mathrm{t}}}$ be the vector of ℓ future commands, $C_{\mathrm{t},\ell} \triangleq I_\ell \otimes C_{\mathrm{t}} \in \mathbb{R}^{\ell p_{\mathrm{t}} \times \ell p}$ where $C_{\mathrm{t}} y_{i|k}$ creates the tracking outputs from $y_{i|k}$, let $Y_{\mathrm{t},1|k,\ell} \triangleq C_{\mathrm{t},\ell} Y_{1|k,\ell}$ be the ℓ-step predicted tracking output, let $C_\ell \triangleq I_\ell \otimes (CC_{\mathrm{c}}) \in \mathbb{R}^{\ell n_{\mathrm{c}} \times \ell p}$ and $\mathcal{D}_\ell \triangleq 1_{\ell\times 1} \otimes \mathcal{D} \in \mathbb{R}^{\ell n_{\mathrm{c}} \times 1}$ where $C_{\mathrm{c}} y_{i|k}$ creates the constrained outputs from $y_{i|k}$, and define $\Delta U_{1|k,\ell} \in \mathbb{R}^{\ell m \times 1}$ as

$$\Delta U_{1|k,\ell} \triangleq \begin{bmatrix} (u_{1|k} - u_k)^{\mathrm{T}} & (u_{2|k} - u_{1|k})^{\mathrm{T}} & \cdots & (u_{\ell|k} - u_{\ell-1|k})^{\mathrm{T}} \end{bmatrix}^{\mathrm{T}}. \tag{2.47}$$

The receding horizon optimization problem is then given by

$$\min_{U_{1|k,\ell}} \left(Y_{\mathrm{t},1|k,\ell} - \mathcal{R}_{k,\ell}\right)^{\mathrm{T}} Q \left(Y_{\mathrm{t},1|k,\ell} - \mathcal{R}_{k,\ell}\right) + \Delta U_{1|k,\ell}^{\mathrm{T}} R \Delta U_{1|k,\ell} \tag{2.48}$$

subject to

$$C_\ell Y_{1|k,\ell} + \mathcal{D}_\ell \leq 0_{\ell n_{\mathrm{c}} \times 1} \tag{2.49}$$

$$U_{\min} \leq U_{1|k,\ell} \leq U_{\max} \tag{2.50}$$

$$\Delta U_{\min} \leq \Delta U_{1|k,\ell} \leq \Delta U_{\max}, \tag{2.51}$$

where $Q \in \mathbb{R}^{\ell p_{\mathrm{t}} \times \ell p_{\mathrm{t}}}$ is the positive definite tracking weight, $R \in \mathbb{R}^{\ell m \times \ell m}$ is the positive definite control move-size weight, $U_{\min} \triangleq 1_{\ell\times 1} \otimes u_{\min} \in \mathbb{R}^{\ell m}$, $U_{\max} \triangleq 1_{\ell\times 1} \otimes u_{\max} \in \mathbb{R}^{\ell m}$, $\Delta U_{\min} \triangleq 1_{\ell\times 1} \otimes \Delta u_{\min} \in \mathbb{R}^{\ell m}$, and $\Delta U_{\max} \triangleq 1_{\ell\times 1} \otimes \Delta u_{\max} \in \mathbb{R}^{\ell m}$.

In summary, at each time step, online identification is performed to find input-output model

coefficients θ_{k+1}, which are then used to create a state space realization $\left(\hat{A}_k, \hat{B}_k, \hat{C}\right)$. The state-space realization is then used in a receding horizon optimization problem to solve for the ℓ-step controls $U_{1|k,\ell}$. The control input for the next step is then given by $u_{1|k}$ and the rest of $U_{1|k,\ell}$ is discarded.

CHAPTER 3

Retrospective Cost Adaptive Control Using Dereverberated Target Models

In this chapter, we apply RCAC to disturbance rejection of lightly damped systems using DTFs. We first explain the sample-data control scenario which is the subject of the sampled-data adaptive disturbance rejection problem. We then explain the concept of DTFs and their applicability and use for disturbance rejection of lightly damped structures. Next, we develop two methods for identification of DTFs. The first using a moving average of the structure's frequency response and the second through constrained optimization from experimental system identification data.

We then discuss the necessary modeling information needed in the target model G_{f} and the retrospective performance variable decomposition for RCAC. The modeling information required by RCAC resides in the *target model* of the closed-loop dynamics; as shown in [23], construction of this model depends on key features of the dynamics of the structure. In the SISO case, this information includes knowledge of the sign of the leading numerator coefficient, relative degree, and nonminimum-phase zeros of the discretized dynamics. In the MIMO case, the required information is obtained through a collection of impulse-response matrices [56]. It is then shown through numerical examples that a DTF with minor modifications can be used as the G_{f} in RCAC for disturbance rejection. For a SISO system we investigate the effect of the magnitude and phase error between the DTF G_{f} and the open-loop transfer function at the frequency of the harmonic disturbance. For many structures, accurate values for the modal damping is unavailable, therefore the target model used for control may not be created from a model with the true value for the damping. We additionally investigate the robustness to mismatches in damping on disturbance rejection for a multi-input single-output (MISO) system. The DTF is created using a nominal model and disturbance rejection is attempted on a structure with varying values of the damping ratio. The resulting asymptotic error is compared to the magnitude and phase error of the target model at the disturbance frequency.

For experimental application, a gradient based RCAC is developed using an instantaneous version of the RCAC cost. An approximate optimal step size is found that is more computationally

efficient than the standard optimal step size for gradient descent. The resulting algorithm is then implemented on a real-time MISO acoustic disturbance rejection experiment.

3.1 Sampled-Data Adaptive Disturbance Rejection

The disturbance rejection problem involves four signals, namely, the performance z, the disturbance w, the output y, and the control u. These signals are related by the transfer functions G_{zu}, G_{zw}, G_{yu}, and G_{yw}, which define the continuous-time, input-output model

$$z(t) = G_{zw}(\mathbf{p})w(t) + G_{zu}(\mathbf{p})u(t), \tag{3.1}$$

$$y(t) = G_{yw}(\mathbf{p})w(t) + G_{yu}(\mathbf{p})u(t), \tag{3.2}$$

where $\mathbf{p}$ is the differentiation operator $\mathrm{d}/\mathrm{d}t$. The signals $y(t)$ and $z(t)$ are sampled instantaneously to obtain $y_k \triangleq y(kT_\mathrm{s}) \in \mathbb{R}^{l_y}$ and $z_k \triangleq z(kT_\mathrm{s}) \in \mathbb{R}^{l_z}$, and the control $u(t) \equiv u_k \in \mathbb{R}^{l_u}$ for all $t \in [kT_\mathrm{s}, (k+1)T_\mathrm{s})$ is reconstructed from u_k using a zero-order-hold (ZOH). The feedback controller $G_\mathrm{c}(\mathbf{q}, \hat{\theta})$, where $\mathbf{q}$ is the forward-shift operator and $\hat{\theta}$ is a vector of controller coefficients that is updated at each step, uses y_k to determine u_k, as shown in Figure 3.1. In order to suppress the effect of the disturbance $w(t)$ on z_k, the adaptive controller uses measurements of z_k to update $G_\mathrm{c}(\mathbf{q}, \hat{\theta})$. The controller update is indicated by the diagonal line in Figure 3.1,

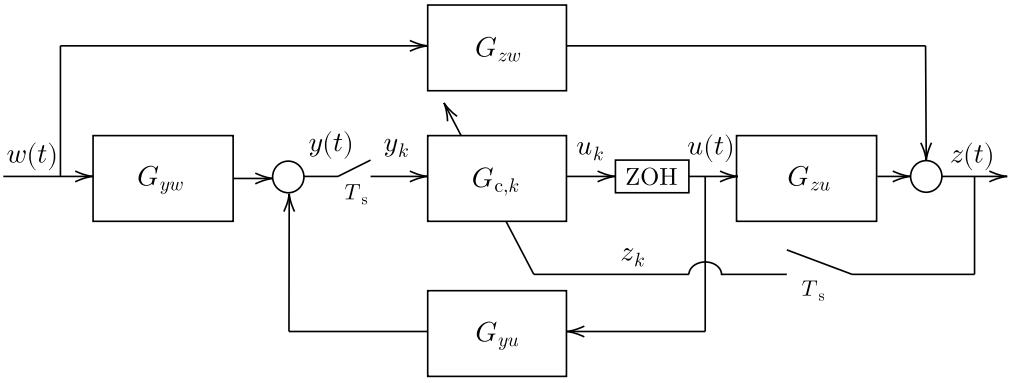

Figure 3.1: Block diagram of the sampled-data adaptive disturbance rejection architecture. The controller $G_{\mathrm{c},k}$ is updated at each time step k.

It follows from (3.1) and (3.2) that z_k and y_k are given by

$$z_k = z_{w,k} + G_{zu,\mathrm{d}}(\mathbf{q})u_k, \tag{3.3}$$

$$y_k = y_{w,k} + G_{yu,\mathrm{d}}(\mathbf{q})u_k, \tag{3.4}$$

where

$$z_{w,k} \triangleq C_{zw} \int_{(k-1)T_s}^{kT_s} e^{A_{zw}(kT_s-t)} B_{zw} w(t)\, \mathrm{d}t + D_{zw} \int_{(k-1)T_s}^{kT_s} w(t)\, \mathrm{d}t, \tag{3.5}$$

$$y_{w,k} \triangleq C_{yw} \int_{(k-1)T_s}^{kT_s} e^{A_{yw}(kT_s-t)} B_{yw} w(t)\, \mathrm{d}t + D_{yw} \int_{(k-1)T_s}^{kT_s} w(t)\, \mathrm{d}t, \tag{3.6}$$

where $(A_{zw}, B_{zw}, C_{zw}, D_{zw})$ and $(A_{yw}, B_{yw}, C_{yw}, D_{yw})$ are realizations of $G_{zu}(\mathbf{p})$ and $G_{yu}(\mathbf{p})$, respectively, and $G_{zu,\mathrm{d}}(\mathbf{q})$ and $G_{yu,\mathrm{d}}(\mathbf{q})$ are the zero-order hold discretizations of $G_{zu}(\mathbf{p})$ and $G_{yu}(\mathbf{p})$, respectively. A block diagram of the discrete-time disturbance rejection problem is shown in Figure 3.2. All simulation based examples in the chapter are conducted in a sample-data feedback loop with integration between samples using *ode45* in order to capture the intersample behavior.

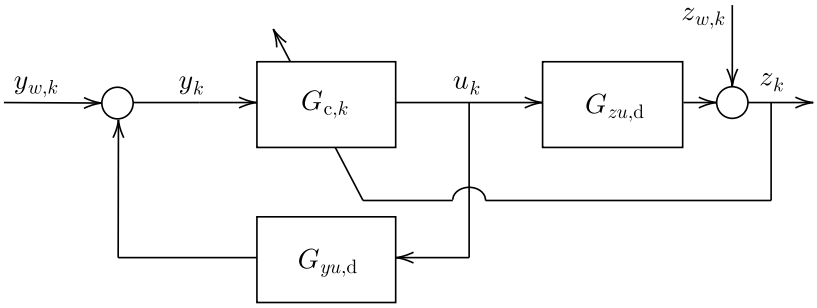

Figure 3.2: Block diagram of the sampled-data adaptive disturbance rejection architecture in discrete time.

3.1.1 Closed-Loop Dynamics with RCAC

From the development of RCAC in Section 2.2 we can write the resulting closed-loop dynamics in the sampled-data adaptive control problem as shown below.

Defining

$$\overline{u}_k(\hat{\theta}) \triangleq \Phi_k \hat{\theta}, \tag{3.7}$$

$$\tilde{u}_k(\hat{\theta}) \triangleq u_k - \overline{u}_k(\hat{\theta}) = u_k - \Phi_k \hat{\theta}, \tag{3.8}$$

(2.19) can be written as

$$\hat{z}_k(\hat{\theta}) = z_k - G_{\mathrm{f}}(\mathbf{q}) \tilde{u}_k(\hat{\theta}). \tag{3.9}$$

Next, using (2.15) and (3.8), the controller $G_{\mathrm{c}}(\mathbf{q},\hat{\theta})$ corresponding to $\hat{\theta}$ is realized as

$$\overline{u}_k(\hat{\theta}) = \sum_{i=1}^{n_{\mathrm{c}}} \hat{P}_i u_{k-i} + \sum_{i=1}^{n_{\mathrm{c}}} \hat{Q}_i y_{k-i} \tag{3.10}$$

$$= \sum_{i=1}^{n_{\mathrm{c}}} \hat{P}_i \overline{u}_{k-i}(\hat{\theta}) + \sum_{i=1}^{n_{\mathrm{c}}} \hat{P}_i \tilde{u}_{k-i}(\hat{\theta}) + \sum_{i=1}^{n_{\mathrm{c}}} \hat{Q}_i y_{k-i}, \tag{3.11}$$

which implies that

$$\overline{u}_k(\hat{\theta}) = D_{\mathrm{c}}^{-1}(\mathbf{q},\hat{\theta})[(\mathbf{q}^{n_{\mathrm{c}}} I_{l_u} - D_{\mathrm{c}}(\mathbf{q},\hat{\theta}))\tilde{u}_k(\hat{\theta}) + N_{\mathrm{c}}(\mathbf{q},\hat{\theta}) y_k], \tag{3.12}$$

where

$$N_{\mathrm{c}}(\mathbf{q},\hat{\theta}) \triangleq \mathbf{q}^{n_{\mathrm{c}}-1}\hat{Q}_1 + \cdots + \hat{Q}_{n_{\mathrm{c}}}, \tag{3.13}$$

$$D_{\mathrm{c}}(\mathbf{q},\hat{\theta}) \triangleq \mathbf{q}^{n_{\mathrm{c}}} I_{l_u} - \mathbf{q}^{n_{\mathrm{c}}-1}\hat{P}_1 - \cdots - \hat{P}_{n_{\mathrm{c}}}. \tag{3.14}$$

Next, defining

$$G_{\mathrm{c}}(\mathbf{q},\hat{\theta}) \triangleq D_{\mathrm{c}}^{-1}(\mathbf{q},\hat{\theta}) N_{\mathrm{c}}(\mathbf{q},\hat{\theta}) \tag{3.15}$$

and substituting (3.8) and (3.12) into (3.3) and (3.4) yields

$$z_k = z_{w,k} + G_{zu,\mathrm{d}}(\mathbf{q}) \left(D_{\mathrm{c}}^{-1}(\mathbf{q},\hat{\theta})[(\mathbf{q}^{n_{\mathrm{c}}} I_{l_u} - D_{\mathrm{c}}(\mathbf{q},\hat{\theta}))\tilde{u}_k(\hat{\theta}) + N_{\mathrm{c}}(\mathbf{q},\hat{\theta}) y_k] + \tilde{u}_k(\hat{\theta}) \right), \tag{3.16}$$

$$y_k = y_{w,k} + G_{yu,\mathrm{d}}(\mathbf{q}) \left(D_{\mathrm{c}}^{-1}(\mathbf{q},\hat{\theta})[(\mathbf{q}^{n_{\mathrm{c}}} I_{l_u} - D_{\mathrm{c}}(\mathbf{q},\hat{\theta}))\tilde{u}_k(\hat{\theta}) + N_{\mathrm{c}}(\mathbf{q},\hat{\theta}) y_k] + \tilde{u}_k(\hat{\theta}) \right), \tag{3.17}$$

where $z_{w,k}$ and $y_{w,k}$ are defined by (3.5) and (3.6). Finally, solving (3.17) for y_k and substituting y_k into (3.16) yields

$$z_k = \xi_k(\hat{\theta}) + \tilde{G}_{z\tilde{u}}(\mathbf{q},\hat{\theta})\tilde{u}_k(\hat{\theta}), \tag{3.18}$$

where

$$\xi_k(\hat{\theta}) \triangleq z_{w,k} + G_{zu,\mathrm{d}}(\mathbf{q}) G_{\mathrm{c}}(\mathbf{q},\hat{\theta})(I_{l_y} - G_{yu,\mathrm{d}}(\mathbf{q}) G_{\mathrm{c}}(\mathbf{q},\hat{\theta}))^{-1} y_{w,k}, \tag{3.19}$$

$$\tilde{G}_{z\tilde{u}}(\mathbf{q},\hat{\theta}) \triangleq \mathbf{q}^{n_c} G_{zu,\mathrm{d}}(\mathbf{q}) \left(D_{\mathrm{c}}^{-1}(\mathbf{q},\hat{\theta}) + G_{\mathrm{c}}(\mathbf{q},\hat{\theta})[I_{l_y} - G_{yu,\mathrm{d}}(\mathbf{q}) G_{\mathrm{c}}(\mathbf{q},\hat{\theta})]^{-1} G_{yu,\mathrm{d}}(\mathbf{q}) D_{\mathrm{c}}^{-1}(\mathbf{q},\hat{\theta}) \right). \tag{3.20}$$

Note that $\xi_k(\hat{\theta})$ is the portion of the measurement z_k due to $w(t)$ when using the controller $G_{\mathrm{c}}(\mathbf{q},\hat{\theta})$.

Finally, note that (3.7)–(3.20) are valid for all $\hat{\theta} \in \mathbb{R}^{l_\theta}$.

3.1.2 Optimal Controller and the Target Model

Now, assume that there exists θ^* that minimizes (2.21) for all k, and define

$$\tilde{u}_k^* \triangleq \tilde{u}_k(\theta^*) = u_k - \overline{u}(\theta^*) = u_k - \Phi_k \theta^*, \tag{3.21}$$

$$\hat{z}_k^* \triangleq \hat{z}_k(\theta^*) = z_k - G_{\mathrm{f}}(\mathbf{q})\tilde{u}_k^*, \tag{3.22}$$

and

$$G_{\mathrm{c}}^*(\mathbf{q}) \triangleq G_{\mathrm{c}}(\mathbf{q}, \theta^*), \tag{3.23}$$

$$\tilde{G}_{z\tilde{u}}^*(\mathbf{q}) \triangleq \tilde{G}_{z\tilde{u}}(\mathbf{q}, \theta^*). \tag{3.24}$$

Since θ^* minimizes (2.21) for all k, for negligible R_u it follows that $\hat{z}_k^* \approx 0$, and thus

$$z_k \approx G_{\mathrm{f}}(\mathbf{q})\tilde{u}_k^*. \tag{3.25}$$

Hence, (3.18) and (3.25) imply

$$\xi_k^* \triangleq \xi_k(\theta^*) \approx [G_{\mathrm{f}}(\mathbf{q}) - \tilde{G}_{z\tilde{u}}^*(\mathbf{q})]\tilde{u}_k^*. \tag{3.26}$$

It follows from (3.25) that $G_{\mathrm{f}}(\mathbf{q})$ is approximately the transfer function from $\tilde{u}_k^*$ to z_k. On the other hand, (3.18) with $\hat{\theta} = \theta^*$ shows that the transfer function from $\tilde{u}_k^*$ to z_k is $\tilde{G}_{z\tilde{u}}^*(\mathbf{q})$. The goal is thus to construct $G_{\mathrm{f}}(\mathbf{q})$ in order to facilitate its approximation by $\tilde{G}_{z\tilde{u}}^*(\mathbf{q})$.

To determine suitable properties of $G_{\mathrm{f}}(\mathbf{q})$, we consider the case where disturbance rejection is approximately achieved, that is, for all $k \geq 0$, $\xi_k^* \approx 0$. Under this assumption, it follows from (3.18) that the transfer function from $\tilde{u}_k^*$ to z_k is $\tilde{G}_{z\tilde{u}}^*(\mathbf{q})$. Now, with θ_{k+1} given by (2.22), it follows that (3.9) and (3.18) become

$$\hat{z}_k(\theta_{k+1}) = z_k - G_{\mathrm{f}}(\mathbf{q})\tilde{u}_k(\theta_{k+1}), \tag{3.27}$$

$$z_k = \xi_k(\theta_{k+1}) + \tilde{G}_{z\tilde{u}}(\mathbf{q}, \theta_{k+1})\tilde{u}_k(\theta_{k+1}). \tag{3.28}$$

Now assuming that $\hat{z}_k(\theta_{k+1}) \to 0$ as $k \to \infty$, (3.27) implies that, for all sufficiently large k,

$$z_k \approx G_{\mathrm{f}}(\mathbf{q})\tilde{u}_k(\theta_{k+1}), \tag{3.29}$$

and thus $G_{\mathrm{f}}(\mathbf{q})$ is approximately the transfer function from $\tilde{u}_k(\theta_{k+1})$ to z_k. Since $\tilde{G}_{z\tilde{u}}(\mathbf{q}, \theta_{k+1})$ is the

actual transfer function from $\tilde{u}_k(\theta_{k+1})$ to z_k, it follows that minimizing (2.21) drives $\tilde{G}_{z\tilde{u}}(\mathbf{q}, \theta_{k+1})$ to $G_{\mathrm{f}}(\mathbf{q})$. Comparing (3.25) to (3.29) implies that

$$G_{\mathrm{f}}(\mathbf{q})\tilde{u}_k(\theta_{k+1}) \approx G_{\mathrm{f}}(\mathbf{q})\tilde{u}_k^*, \tag{3.30}$$

which, under sufficient persistence of excitation, implies that θ_{k+1} converges to θ^*, and thus $\tilde{G}^*_{z\tilde{u}}(\mathbf{q})$ approximates $G_{\mathrm{f}}(\mathbf{q})$. Consequently, $G_{\mathrm{f}}(\mathbf{q})$ serves as a target model for $\tilde{G}^*_{z\tilde{u}}(\mathbf{q})$.

In the case where y_k, z_k, and u_k are scalar, $\tilde{G}_{z\tilde{u}}(\mathbf{q}, \theta_{k+1})$ can be written as

$$\tilde{G}_{z\tilde{u}}(\mathbf{q}, \theta_{k+1}) = \frac{\mathbf{q}^{n_c} N_{zu,\mathrm{d}}(\mathbf{q})}{D(\mathbf{q})D_{\mathrm{c}}(\mathbf{q}, \theta_{k+1}) - N_{yu,\mathrm{d}}(\mathbf{q})N_{\mathrm{c}}(\mathbf{q}, \theta_{k+1})}, \tag{3.31}$$

where $G_{zu,\mathrm{d}}(\mathbf{q}) = N_{zu,\mathrm{d}}(\mathbf{q})/D(\mathbf{q})$ and $G_{yu,\mathrm{d}}(\mathbf{q}) = N_{yu,\mathrm{d}}(\mathbf{q})/D(\mathbf{q})$. Note that the zeros of $\tilde{G}_{z\tilde{u}}(\mathbf{q}, \theta_{k+1})$ include the zeros of $G_{zu,\mathrm{d}}(\mathbf{q})$. Although these zeros do not depend on $G_{\mathrm{c}}(\mathbf{q}, \theta_{k+1})$, they can be canceled by roots of the denominator of $\tilde{G}_{z\tilde{u}}(\mathbf{q}, \theta_{k+1})$. In the case of NMP zeros, this cancellation represents a hidden instability due to the cascade interconnection between the structure and $G_{\mathrm{c}}(\mathbf{q}, \theta_{k+1})$ [20]. As shown in [23], this cancellation can be prevented by ensuring that all NMP zeros of $G_{zu}(\mathbf{q})$ are also zeros of $G_{\mathrm{f}}(\mathbf{q})$.

3.1.3 Retrospective Performance Variable Decomposition

Substituting (3.28) into (3.27) yields

$$\hat{z}_k(\theta_{k+1}) = \xi_k(\theta_{k+1}) + [\tilde{G}_{z\tilde{u}}(\mathbf{q}, \theta_{k+1}) - G_{\mathrm{f}}(\mathbf{q})]\tilde{u}_k(\theta_{k+1}). \tag{3.32}$$

By defining the *one-step predicted performance*

$$\hat{z}_{\mathrm{opp},k}(\theta_{k+1}) \triangleq \xi_k(\theta_{k+1}) \tag{3.33}$$

and the *target-model matching performance*

$$\hat{z}_{\mathrm{tmp},k}(\theta_{k+1}) \triangleq [\tilde{G}_{z\tilde{u}}(\mathbf{q}, \theta_{k+1}) - G_{\mathrm{f}}(\mathbf{q})]\tilde{u}_k(\theta_{k+1}), \tag{3.34}$$

(3.32) can be written as

$$\hat{z}_k(\theta_{k+1}) \triangleq \hat{z}_{\mathrm{opp},k}(\theta_{k+1}) + \hat{z}_{\mathrm{tmp},k}(\theta_{k+1}). \tag{3.35}$$

The decomposition of the retrospective performance in (3.35) shows the interplay between the one-step predicted performance and the target-model matching performance. The one-step predicted

performance represents the closed-loop response of z_k to the disturbance $w(t)$ when the controller θ_{k+1} is used, while the target-model matching performance represents the difference between $\tilde{G}_{z\tilde{u}}(\mathbf{q}, \theta_{k+1})$ and $G_{\mathrm{f}}(\mathbf{q})$ driven by $\tilde{u}_k(\theta_{k+1})$. Minimizing (2.21) with negligible R_u yields

$$\hat{z}_k(\theta_{k+1}) \approx 0 \tag{3.36}$$

which, using (3.35) implies

$$\hat{z}_{\mathrm{opp},k}(\theta_{k+1}) + \hat{z}_{\mathrm{tmp},k}(\theta_{k+1}) \approx 0 \tag{3.37}$$

that is,

$$\hat{z}_{\mathrm{opp},k}(\theta_{k+1}) \approx -\hat{z}_{\mathrm{tmp},k}(\theta_{k+1}) \tag{3.38}$$

3.1.4 Standard Construction of the Target Model

In the SISO case, note that the relative degree of $\tilde{G}_{z\tilde{u}}(\mathbf{q}, \theta_{k+1})$ is equal to the relative degree of $G_{zu,\mathrm{d}}(\mathbf{q})$. Therefore, in order to facilitate model matching between $\tilde{G}_{z\tilde{u}}(\mathbf{q}, \theta_{k+1})$ and $G_{\mathrm{f}}(\mathbf{q})$, we choose the relative degree of $G_{\mathrm{f}}(\mathbf{q})$ to be equal to the relative degree of $G_{zu,\mathrm{d}}(\mathbf{q})$. For the same reason, we also construct $G_{\mathrm{f}}(\mathbf{q})$ to have the same leading numerator coefficient as $G_{zu,\mathrm{d}}(\mathbf{q})$.

Furthermore, it can be seen that the numerator of $\tilde{G}_{z\tilde{u}}(\mathbf{q}, \theta_{k+1})$ contains all of the zeros present in $G_{zu,\mathrm{d}}(\mathbf{q})$. Therefore, as the target-model matching performance is minimized, any NMP zeros that are present in $G_{zu,\mathrm{d}}(\mathbf{q})$, but not in $G_{\mathrm{f}}(\mathbf{q})$ can lead to unstable pole-zero cancellation. Therefore, $G_{\mathrm{f}}(\mathbf{q})$ must be constructed such that all of the NMP zeros of $G_{zu,\mathrm{d}}(\mathbf{q})$ are present in $G_{\mathrm{f}}(\mathbf{q})$.

A straightforward technique for constructing $G_{\mathrm{f}}(\mathbf{q})$ that satisfies these requirements in the SISO case is given by

$$G_{\mathrm{f}}(\mathbf{q}) = \sum_{i=0}^{n_{\mathrm{f}}} \frac{H_i}{\mathbf{q}^i}, \tag{3.39}$$

where H_i is the ith the Markov parameter of $G_{zu,\mathrm{d}}(\mathbf{q})$ and n_{f} is the order of $G_{\mathrm{f}}(\mathbf{q})$. In the case where the structure is minimum phase and asymptotically stable, only the first nonzero Markov parameter is used in the summation. For NMP structures, the order of n_{f} must be large enough such that the NMP zeros of $G_{\mathrm{f}}(\mathbf{q})$ approximate the NMP zeros of $G_{zu,\mathrm{d}}(\mathbf{q})$.

Note that the FIR transfer function (3.39) is a truncated Laurent expansion of $G_{zu,\mathrm{d}}(\mathbf{q})$ [56]. Therefore, by choosing a sufficiently large value of n_{f}, $G_{\mathrm{f}}(\mathbf{q})$ provides an approximation of $G_{zu,\mathrm{d}}(\mathbf{q})$ that is useful in the MIMO case. Unfortunately, for lightly damped structures, several hundred Markov parameters may be needed to approximate the NMP zeros; this number is prohibitively

large in applications. To overcome this difficulty, we use a dereverberated transfer function as the target model.

3.2 Dereverberated Transfer Functions

A dereverberated model of a lightly damped structure captures the magnitude and phase trend but ignores resonances and anti-resonances [57, 58, 59, 60]. A DTF is thus an approximate, low-order model of a lightly damped structure that can easily be obtained in practice and is insensitive to details of lightly damped poles and zeros.

Various techniques have been developed for generating a DTF from an analytical or empirical model of a structure [61, 62, 63, 64]. All of these techniques capture some aspect of the mean of the frequency response, for example, by optimizing the logarithmic-average of the magnitude of the frequency response. Along these lines, the developed methods extend the method used in [57] by accounting for both the magnitude and phase of the frequency response.

3.2.1 Identification Using Complex Windowed Average

The dereverberated transfer function can be constructed by smoothing the frequency response of $G_{\mathrm{d}}(z)$ with a windowed average and using the resulting smoothed frequency response to identify the dereverberated transfer function $\widehat{G}_{\mathrm{d}}(z)$. Given a window size of 2Δ rad s^{-1}, the complex windowed average frequency response is given by

$$\overline{G}_{\mathrm{d}}(\mathrm{e}^{\jmath\theta}) = \frac{1}{\theta_{\min} - \theta_{\max}} \int_{\theta_{\max}}^{\theta_{\min}} G_{\mathrm{d}}(\mathrm{e}^{\jmath v})\, \mathrm{d}v, \tag{3.40}$$

where $\theta_{\min} \triangleq \min(\pi, \theta + \Delta)$ and $\theta_{\max} \triangleq \max(0, \theta - \Delta)$. The dereverberated transfer function $\widehat{G}_{\mathrm{d}}(z)$ is then constructed by fitting $\widehat{G}_{\mathrm{d}}(\mathrm{e}^{\jmath\theta})$ to $\overline{G}_{\mathrm{d}}(\mathrm{e}^{\jmath\theta})$ and enforcing asymptotic stability of $\widehat{G}_{\mathrm{d}}(z)$. The order is chosen to be as low as possible while still capturing the rolloff and phase characteristics of $\overline{G}_{\mathrm{d}}(\mathrm{e}^{\jmath\theta})$, and Δ is chosen such that all the modes in $G_{\mathrm{d}}(\mathrm{e}^{\jmath\theta})$ are smoothed out while maintaining the backbone of the response. The algorithm used to construct $\widehat{G}_{\mathrm{d}}(z)$ from $\overline{G}_{\mathrm{d}}(\mathrm{e}^{\jmath\theta})$ is given by Algorithm 1 of [65] except that the order of $\widehat{G}_{\mathrm{d}}(z)$ is fixed beforehand. For MIMO systems, the method is performed channel by channel.

3.2.1.1 Complex Windowed Averaging Dereverberated Target Model Example

Consider the second-order structure with natural frequency $\omega_n = 20\pi$ rad s^{-1} and damping ratio $\zeta = 0.05$ given by

$$G(s) = \frac{(20\pi)^2}{s^2 + 2\pi s + (20\pi)^2}, \tag{3.41}$$

where s is the Laplace variable. Discretizing (3.41) with sample-rate $T_s = 0.01$ s gives

$$G_d(z) = \frac{0.1871z + 0.1831}{z^2 - 1.569z + 0.9391}. \tag{3.42}$$

The resulting dereverberated transfer function when using complex windowed averaging with $\Delta = 10\pi$ rad s^{-1} and $\hat{n}_{max} = 2$ is given by

$$\widehat{G}_d(z) = \frac{0.1842z + 0.181}{z^2 - 1.333z + 0.6814}. \tag{3.43}$$

From Figure 3.3, the complex windowed average frequency response does not capture the modes of the system, but has two spurious modes beside the true mode at 20π rad s^{-1} due to the window size of 10π rad s^{-1}. Consequently, the dereverberated transfer function resulting from averaging has complex poles, and the spectral radius is reduced compared to G_d with a damping ratio of 0.29.

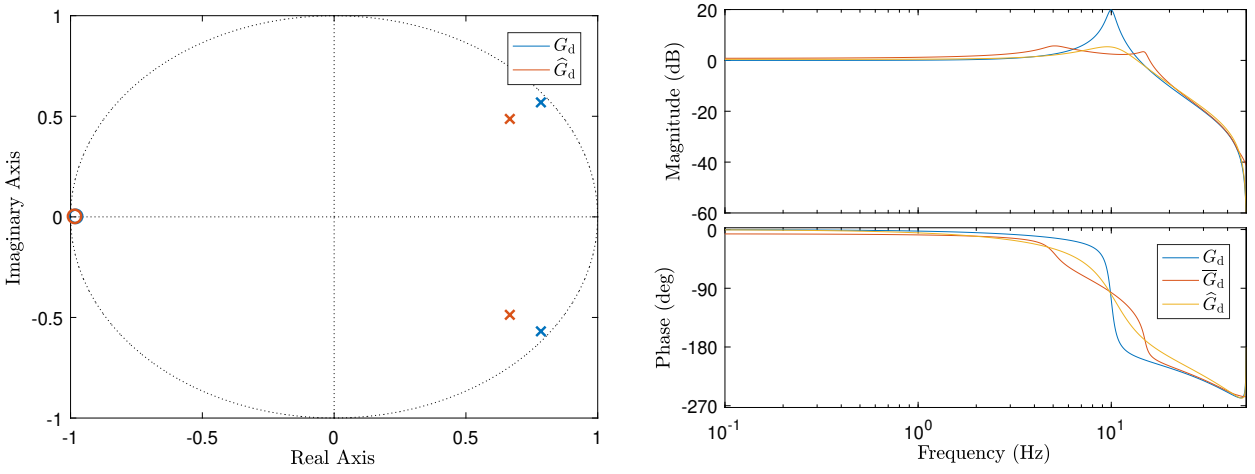

(a) (b)

Figure 3.3: Complex windowed average dereverberated transfer function. a) Poles and zeros of the discretized structural model and the dereverberated transfer function $\widehat{G}_d(z)$ b) Frequency response of $\widehat{G}_d$, $\overline{G}_d(z)$ and $\widehat{G}_d(z)$. Notice that the phase of $\widehat{G}_d(z)$ follows the general trend of the phase of $G_d(z)$.

3.2.2 Identification Using Optimization

Let $G_\mathrm{d}(z)$ be a discrete-time transfer function of order n with frequency response $G_\mathrm{d}(\mathrm{e}^{\mathrm{j}\theta})$, where $\theta \in [0, \pi]$. The goal is to determine a dereverberated transfer function $\widehat{G}_\mathrm{d}(z)$ of order $\hat{n} << n$ whose frequency response approximates the frequency response of $G_\mathrm{d}(z)$. We construct $\widehat{G}_\mathrm{d}(z)$ by minimizing the logarithmic-average of the error between $G_\mathrm{d}(\mathrm{e}^{\mathrm{j}\theta})$ and $\widehat{G}_\mathrm{d}(\mathrm{e}^{\mathrm{j}\theta})$ subject to the constraint that all poles and zeros of $\widehat{G}_\mathrm{d}(z)$ are real and that $\widehat{G}_\mathrm{d}(z)$ is asymptotically stable. By restricting the poles and zeros to be real, we can construct a transfer function that captures the magnitude and phase trend of $G_\mathrm{d}(\mathrm{e}^{\mathrm{j}\theta})$ without resonances and anti-resonances. More formally, for a specified value of the maximum order $\hat{n}_\mathrm{max} << n$ of the dereverberated transfer function $\widehat{G}_\mathrm{d}(z)$, the goal is to solve the optimization problem

$$\min_{k,a,b,\hat{n},\hat{m}} \quad \int_0^\pi |G_\mathrm{d}(\mathrm{e}^{\mathrm{j}\theta}) - \widehat{G}_\mathrm{d}(\mathrm{e}^{\mathrm{j}\theta})|^2 \, \mathrm{d}(\log\theta) \tag{3.44}$$

subject to

$$\widehat{G}_\mathrm{d}(z) = \frac{k \prod_{i=1}^{\hat{m}} (z + b_i)}{\prod_{i=1}^{\hat{n}} (z + a_i)}, \tag{3.45}$$

$$\hat{m} \leq \hat{n} \leq \hat{n}_\mathrm{max}, \tag{3.46}$$

$$\widehat{G}_\mathrm{d}(z) \text{ is asymptotically stable,} \tag{3.47}$$

where $\hat{m} \geq 0$ is the number of zeros, $a \in \mathbb{R}^{\hat{n}}$ is the vector of poles, $b \in \mathbb{R}^{\hat{m}}$ is the vector of zeros, and $k \in \mathbb{R}$ is a scaling factor. If $\hat{m} = 0$, then the numerator of $\widehat{G}_\mathrm{d}(z)$ is k. In order to simplify the optimization, $\hat{m}$ can be fixed beforehand. For example, $\hat{m}$ can be chosen such that the relative degree of the dereverberated transfer function equals the relative degree of the structure. The maximum order $\hat{n}_\mathrm{max}$ of $\widehat{G}_\mathrm{d}(z)$ is typically chosen to be much lower than the order of $G_\mathrm{d}(z)$ in order to obtain a low-order model that efficiently captures the rolloff and phase characteristics of $G_\mathrm{d}(z)$. For MIMO systems, the DTF is formed by solving the above optimization problem channel by channel.

3.2.2.1 Optimization Based Dereverberated Target Model Example

Consider the structure given by (3.41) and discretized at a sample-rate of $T_\mathrm{s} = 0.01$ s such that the resulting discrete-time system is given by (3.42).

The resulting dereverberated transfer function using optimization with $\hat{n}_\mathrm{max} = 1$ is given by

$$\widehat{G}_\mathrm{d}(z) = \frac{0.5126}{z - 0.5544}. \tag{3.48}$$

Figure 3.4 shows that the phase of $\widehat{G}_{\mathrm{d}}(z)$ follows the trend of the phase of $G_{\mathrm{d}}(z)$ without large phase shifts. Note that for bode magnitude plots, dB is $20\log(|T(\mathrm{j}\omega)|)$ for continuous transfer functions and $20\log(|T(\mathrm{e}^{\mathrm{j}\omega T_{\mathrm{s}}})|)$ for discrete transfer functions where T is the respective transfer function.

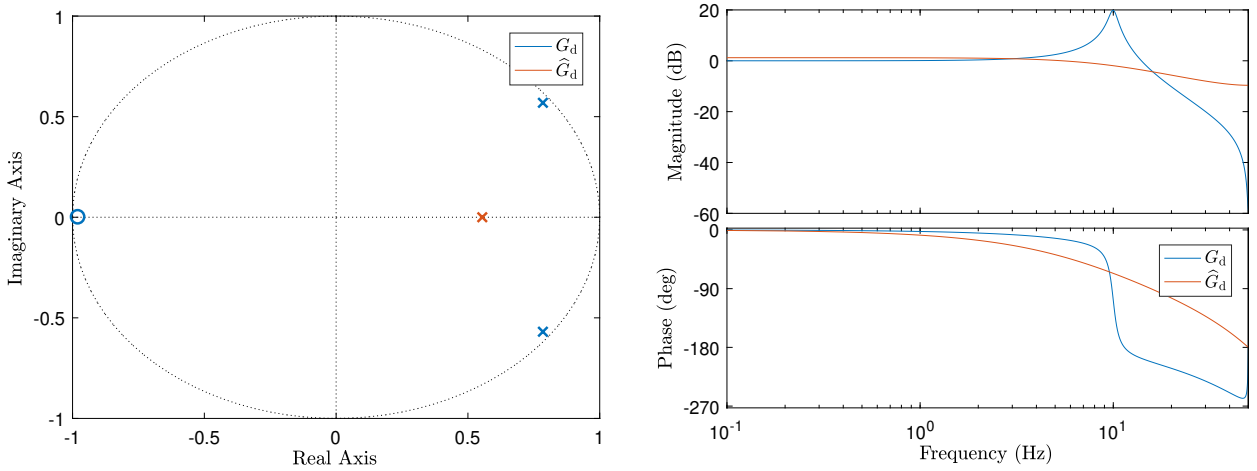

(a) (b)

Figure 3.4: Optimization based dereverberated transfer function: Single-mode SISO Structure a) Poles and zeros of the discretized structural model and the dereverberated transfer function $\widehat{G}_{\mathrm{d}}(z)$, which has one real pole. b) Frequency response of $\widehat{G}_{\mathrm{d}}(z)$. Note that the phase of $\widehat{G}_{\mathrm{d}}(z)$ follows the trend of the phase of $G_{\mathrm{d}}(z)$.

3.2.3 Construction of the Dereverberated Target Model

Directly using a dereverberated transfer function for the target model G_{f} leads to poor disturbance rejection performance. This is due to the DTF being similar to the open loop system in magnitude. However, only a simple adjustment to the DTF is needed to improve the disturbance rejection performance. The adjusted DTF that is used as the target model G_{f} is termed the DTM.

In particular we set,

$$G_{\mathrm{f}}(z) = \beta \widehat{G}_{\mathrm{d}}(z), \tag{3.49}$$

where $\beta \in (0, 1]$. With $\beta \in [0.5, 0.9]$ being the values typically used. The parameter β is a tuning parameter that provides a trade-off between disturbance rejection performance and robustness with smaller values of β providing better disturbance rejection performance.

3.3 Numerical Examples

3.3.1 SISO Adaptive Disturbance Rejection

Let

$$G(s) = \frac{400\pi^2\omega_{\mathrm{p}}^2}{\omega_{\mathrm{z}}^2} \frac{s^2 + 2\zeta\omega_{\mathrm{z}}s + \omega_{\mathrm{z}}^2}{(s + 10\pi)(s + 40\pi)(s^2 + 2\zeta\omega_{\mathrm{p}}s + \omega_{\mathrm{p}}^2)} \tag{3.50}$$

and consider the block diagram in Figure 3.1 with $G(s) = G_{zu}(s) = G_{zw}(s) = G_{yu}(s) = G_{yw}(s)$, $T_{\mathrm{s}} = 0.01$ s, and $\omega_{\mathrm{p}} = 20\pi$ rad s^{-1}. The following subsections investigate the performance of RCAC when using a DTM for harmonic disturbance rejection on (3.50) for various disturbance frequencies and values of ω_{z} and ζ. The simulations are conducted in a sample-data feedback loop with integration between samples in order to capture the intersample behavior of the system. For each case, the harmonic disturbance frequency ω_{d} is swept from 4π to 50π rad s^{-1}, and the asymptotic error at the sample times is plotted against the magnitude and phase error between $G_{\mathrm{f}}(e^{j\omega_{\mathrm{d}}T_{\mathrm{s}}})$ and $G_{zu,\mathrm{d}}(e^{j\omega_{\mathrm{d}}T_{\mathrm{s}}})$.

3.3.1.1 Complex Windowed Averaging

The complex windowed average method is used with $\hat{n}_{\max} = 2$, $\Delta = 8\pi$ rad s^{-1}, and a scaling of $\beta = 1$, along with RCAC being initialized with $n_{\mathrm{c}} = 20$, $\theta_0 = 0_{l_\theta}$, $k_w = 5n_{\mathrm{c}}$, $\alpha = 0.5$, and $R = 0$. The resulting magnitude of the asymptotic closed-loop response at the sample times is plotted along with the magnitude error versus the phase error between $G_{\mathrm{f}}(e^{j\omega_{\mathrm{d}}T_{\mathrm{s}}})$ and $G_{zu,\mathrm{d}}(e^{j\omega_{\mathrm{d}}T_{\mathrm{s}}})$ for various values of ω_{z} and ζ in Figure 3.5. For the specific case where $\omega_{\mathrm{d}} = 21\pi$ rad s^{-1}, $\omega_{\mathrm{z}} = 22\pi$ rad s^{-1}, and $\zeta = 0.01$, the resulting closed-loop dereverberated target model is shown in Figure 3.6 with the resulting closed-loop response in Figure 3.7.

3.3.1.2 Optimization

The optimization method is used with $\hat{n}_{\max} = 2$, and a scaling of $\beta = 0.8$, along with RCAC being initialized with $n_{\mathrm{c}} = 20$, $\theta_0 = 0_{l_\theta}$, $k_w = 5n_{\mathrm{c}}$, $\alpha = 0.5$, and $R = 0$. The resulting magnitude of the asymptotic closed-loop response at the sample times is plotted along with the magnitude error versus the phase error between $G_{\mathrm{f}}(e^{j\omega_{\mathrm{d}}T_{\mathrm{s}}})$ and $G_{zu,\mathrm{d}}(e^{j\omega_{\mathrm{d}}T_{\mathrm{s}}})$ for various values of ω_{z} and ζ in Figure 3.8. For the specific case where $\omega_{\mathrm{d}} = 21\pi$ rad s^{-1}, $\omega_{\mathrm{z}} = 22\pi$ rad s^{-1}, and $\zeta = 0.01$, the resulting closed-loop dereverberated target model is shown in Figure 3.9 with the resulting closed-loop response in Figure 3.10.

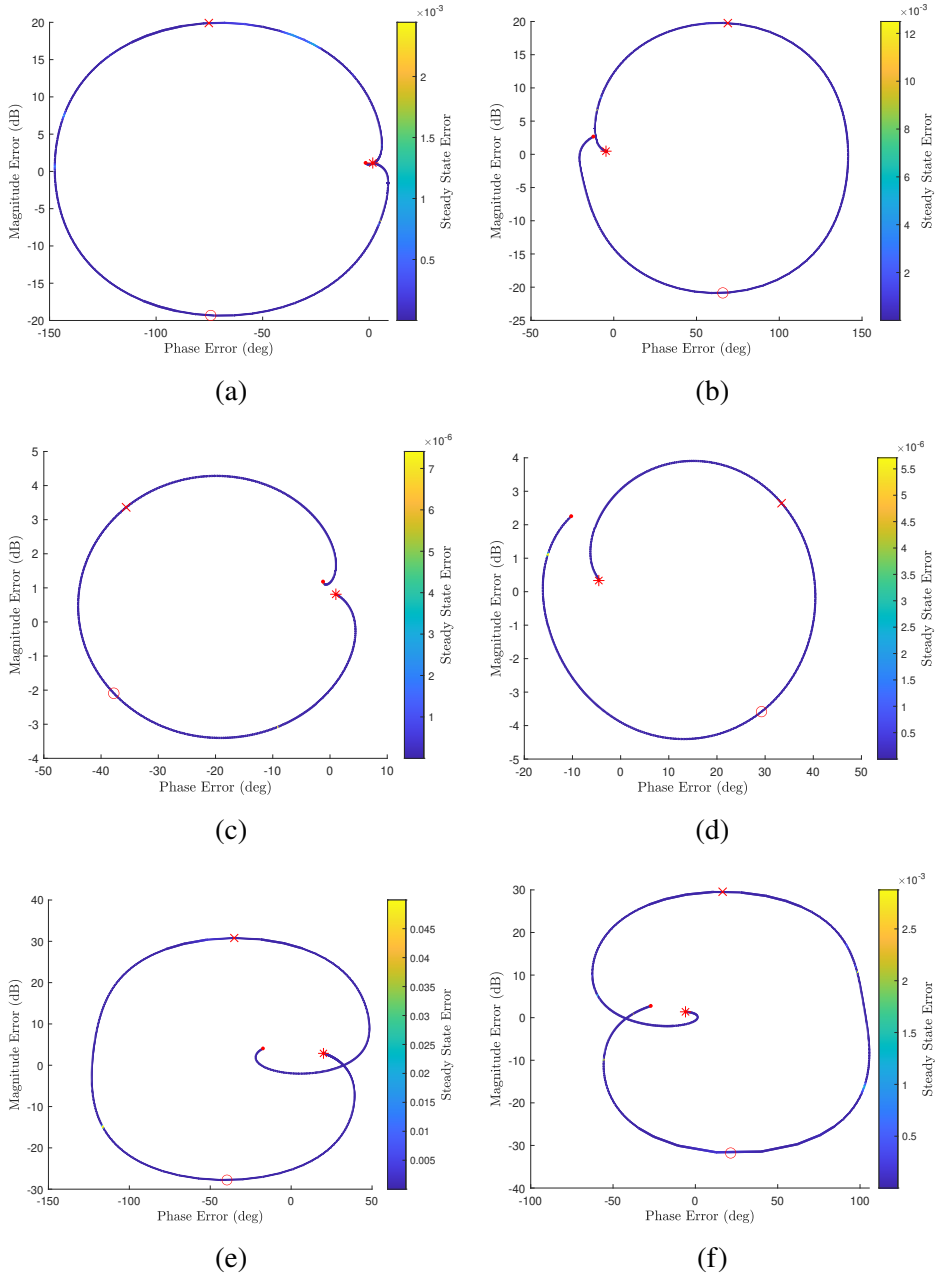

Figure 3.5: SISO example: complex windowed average dereverberated target model. Magnitude of the asymptotic closed-loop response at the sample times along with the magnitude error versus the phase error between $G_{\mathrm{f}}(e^{J\omega_{\mathrm{d}}T_{\mathrm{s}}})$ and $G_{zu,\mathrm{d}}(e^{J\omega_{\mathrm{d}}T_{\mathrm{s}}})$ as ω_{d} is swept from 4π to 50π rad s^{-1} for various values of ζ and ω_{z}. Here, "·" corresponds to the 4π rad s^{-1} disturbance, "*" for the 50π rad s^{-1} disturbance, "x" for the damped frequency of the pole, and "o" for the damped frequency of the zero. a) $\zeta = 0.01$, $\omega_{\mathrm{z}} = 22\pi$ rad s^{-1}; b) $\zeta = 0.01$, $\omega_{\mathrm{z}} = 18\pi$ rad s^{-1}; c) $\zeta = 0.1$, $\omega_{\mathrm{z}} = 22\pi$ rad s^{-1}; d) $\zeta = 0.1$, $\omega_{\mathrm{z}} = 18\pi$ rad s^{-1}; e) $\zeta = 0.01$, $\omega_{\mathrm{z}} = 28\pi$ rad s^{-1}; f) $\zeta = 0.01$, $\omega_{\mathrm{z}} = 12\pi$ rad s^{-1}

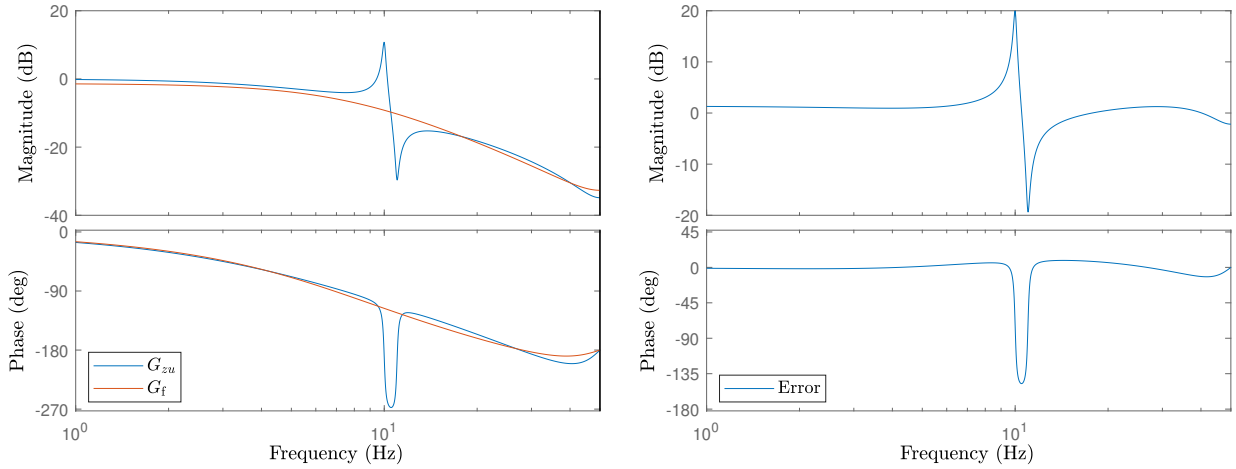

(a) (b)

Figure 3.6: SISO example: complex windowed average dereverberated target model for $\omega_{\mathrm{z}} = 22\pi$ rad s^{-1}, and $\zeta = 0.01$. a) frequency response of the discretized G_{zu} and the closed-loop dereverberated target model G_{f}. The closed-loop dereverberated target model was constructed by using the complex windowed average method with $\hat{n}_{\max} = 2$, and $\Delta = 8\pi$ rad s^{-1}. b) error between the frequency response of the discretized G_{zu} and G_{f}.

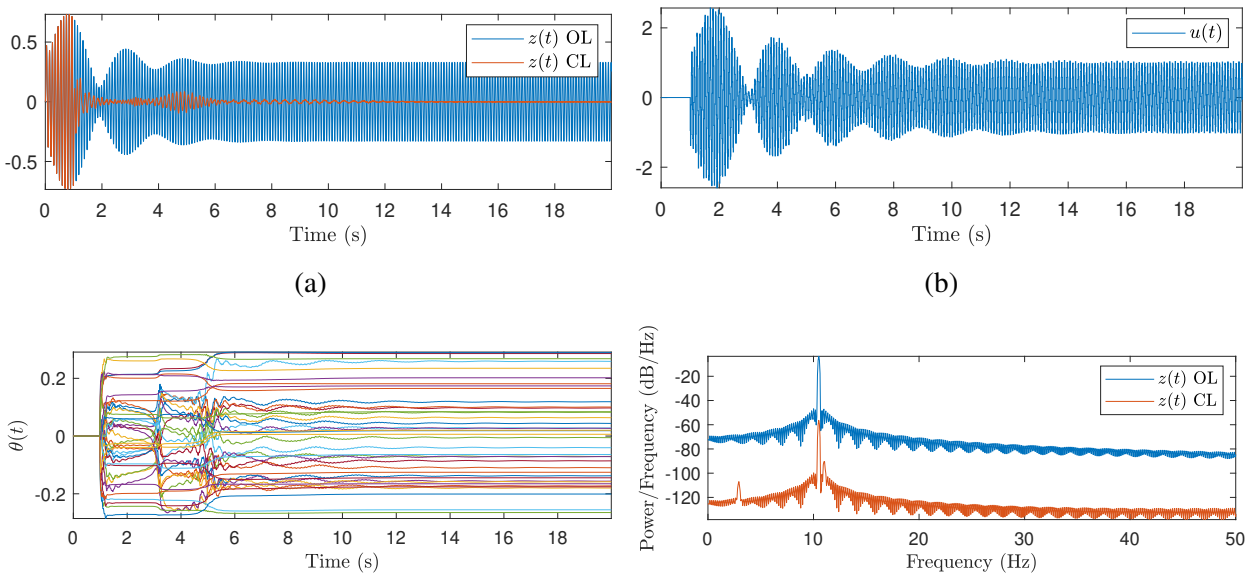

(a) (b)

(c) (d)

Figure 3.7: SISO adaptive disturbance rejection using complex windowed average dereverberated target model. Closed-loop response with $\omega_{\mathrm{d}} = 21\pi$ rad s^{-1}, $\omega_{\mathrm{z}} = 22\pi$ rad s^{-1}, and $\zeta = 0.01$. a) open-loop and closed-loop response of the system subject to the harmonic disturbance. RCAC starts at 1 s. b) RCAC's control input. c) coefficients of RCAC as they converge. d) power spectral density of both the open and closed-loop responses. Notice that the peak in the open-loop response corresponding to the disturbance is suppressed in the closed-loop response.

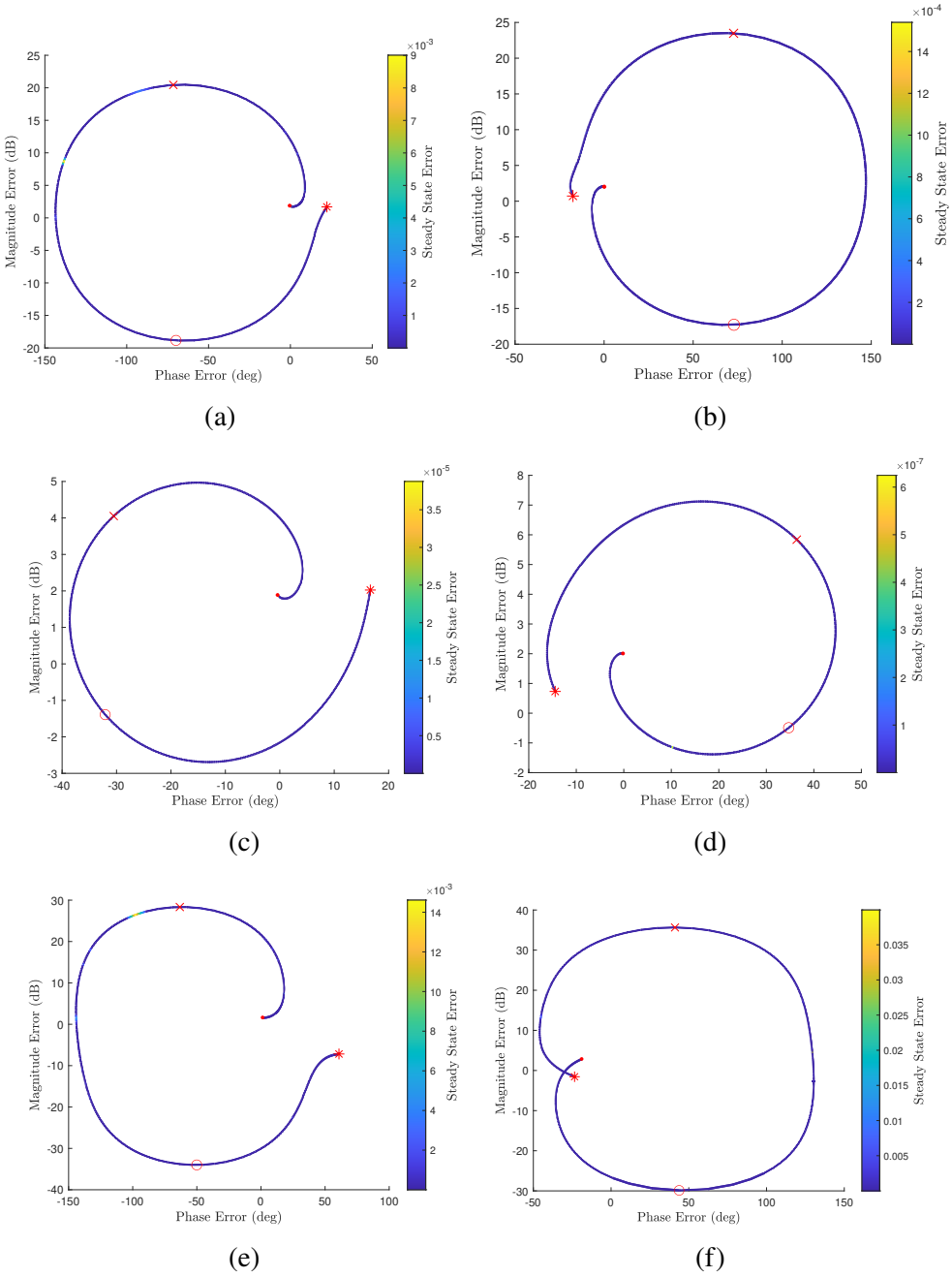

Figure 3.8: SISO example: optimization based dereverberated target model. Magnitude of the asymptotic closed-loop response at the sample times along with the magnitude error versus the phase error between $G_{\mathrm{f}}(e^{J\omega_{\mathrm{d}}T_{\mathrm{s}}})$ and $G_{zu,\mathrm{d}}(e^{J\omega_{\mathrm{d}}T_{\mathrm{s}}})$ as ω_{d} is swept from 4π to 50π rad s^{-1} for various values of ζ and ω_{z}. The labeling and symbols is the same as in Figure 3.5.

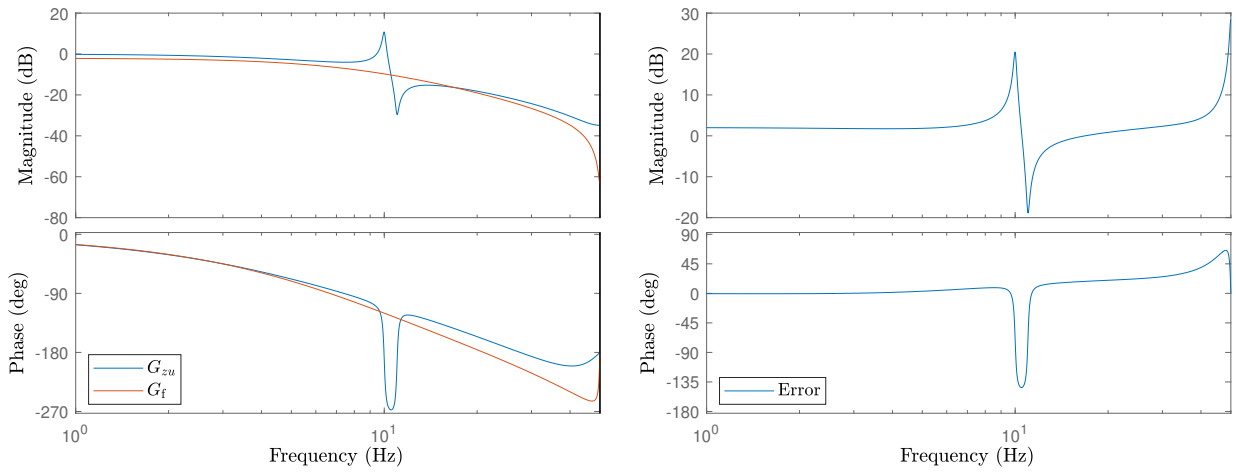

(a) (b)

Figure 3.9: SISO example: optimization based dereverberated target model for $\omega_z = 22\pi$ rad s^{-1}, and $\zeta = 0.01$. a) the frequency response of the discretized G_{zu} and the closed-loop dereverberated target model G_f. The closed-loop dereverberated target model was constructed by using the optimization based method with $\hat{n}_{max} = 2$, and scaling the result by $\beta = 0.8$. b) the error between the frequency response of the discretized G_{zu} and G_f.

3.3.2 MISO Adaptive Disturbance Rejection

Consider the 4-mode, 2-input, 1-output structure MISO in Figure 3.11 and the block diagram in Figure 3.1 with $G(s) = G_{zu}(s) = G_{zw}(s) = G_{yu}(s) = G_{yw}(s)$, and $T_s = 0.01$ s. All poles and zeros have the same damping ratio of $\zeta = 0.1$. The following subsections investigate the performance of RCAC on a structure that has a different damping ratio than the model used to generate the dereverberated target model. Specifically, RCAC is implemented in closed-loop for 50 different values of the structural damping, ζ from 0.01 to 0.5, with a dereverberated target model computed from the nominal $\zeta = 0.1$ model. There are two harmonic disturbances at $\omega_{d1} = 22\pi$ and $\omega_{d2} = 34\pi$ rad s^{-1} with the first input receiving the 22π rad s^{-1} disturbance and the second input receiving the 34π rad s^{-1} disturbance.

3.3.2.1 Complex Windowed Averaging

The complex windowed average method is used with $\hat{n} = 2$, $\Delta = 8\pi$ rad s^{-1}, and $\beta = \gamma = 1$. RCAC is initialized with $n_c = 20$, $\theta_0 = 0_{l_\theta}$, $k_w = 5n_c$, $\alpha = 0.2$, and $R = 0$. Figure 3.12 shows the resulting magnitude of the asymptotic closed-loop response at the sample times along with the magnitude error versus the phase error between $G_f(e^{j\omega_d T_s})$ and $G_{zu,d}(e^{j\omega_d T_s})$ for 50 values of ζ from 0.01 to 0.1. For $\zeta = 0.01$, Figure 3.13 compares the structure and the dereverberated target model constructed from the $\zeta = 0.1$ model, with the resulting closed-loop response shown in Figure 3.14.

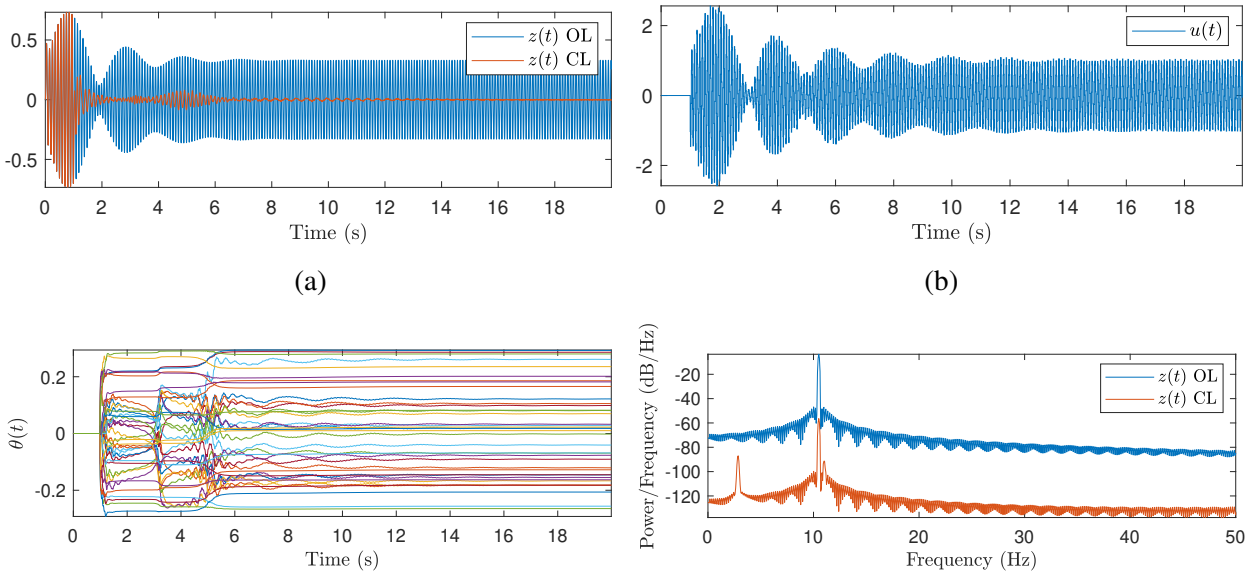

Figure 3.10: SISO adaptive disturbance rejection using optimization based dereverberated target model. Closed-loop response with $\omega_d = 21\pi$ rad s^{-1}, $\omega_z = 22\pi$ rad s^{-1}, and $\zeta = 0.01$. a) shows the open-loop and closed-loop response of the system subject to the harmonic disturbance. RCAC starts at 1 s. b) shows RCAC's control input. c) shows the coefficients of RCAC as they converge. d) shows the power spectral density of both the open and closed-loop responses. Notice that the peak in the open-loop response corresponding to the disturbance is suppressed in the closed-loop response.

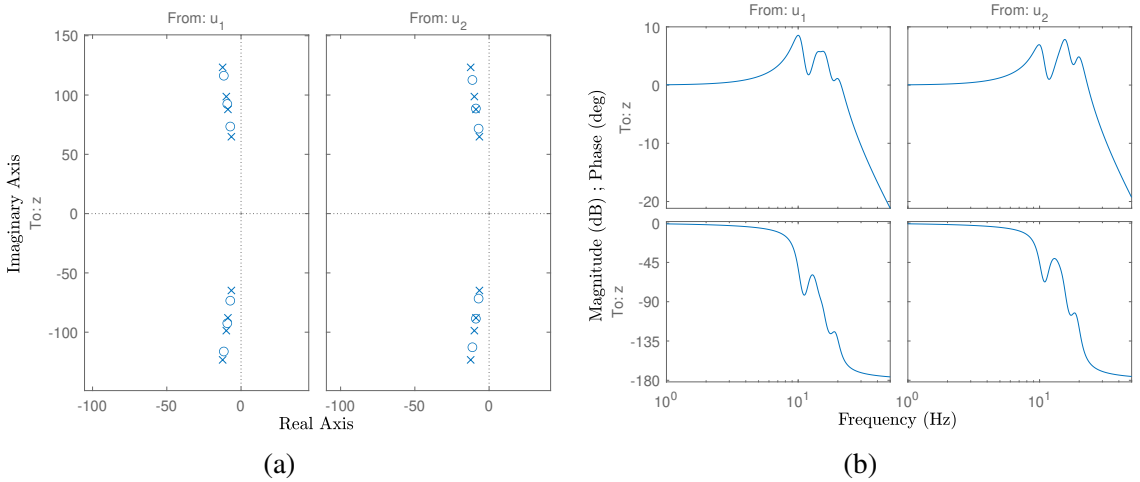

Figure 3.11: MISO structure: 4-mode, 2-input, 1-output structure. All poles and zeros have damping ratio $\zeta = 0.1$. a) Pole-zero plot. b) Frequency response.

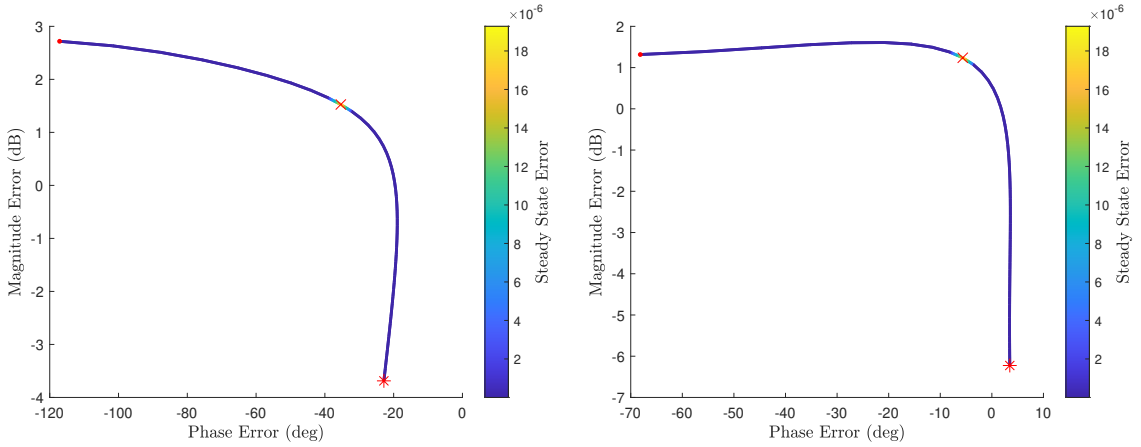

Figure 3.12: MISO example: complex windowed average dereverberated target model. Magnitude of the asymptotic closed-loop response at the sample instances along with the magnitude error versus the phase error between $G_{\mathrm{f}}(e^{\mathrm{j}\omega_{\mathrm{d}}T_{\mathrm{s}}})$ and $G_{zu,\mathrm{d}}(e^{\mathrm{j}\omega_{\mathrm{d}}T_{\mathrm{s}}})$ at the disturbance frequency of the respective channel as ζ is swept between 0.01 to 0.5 when using G_{f} computed from the $\zeta = 0.1$ model. Here, "·" corresponds to $\zeta = 0.01$, "*" for $\zeta = 0.5$, and "x" for $\zeta = 0.1$. a) Magnitude error versus the phase error between $G_{\mathrm{f}}(e^{\mathrm{j}\omega_{\mathrm{d}1}T_{\mathrm{s}}})$ and $G_{zu,\mathrm{d}}(e^{\mathrm{j}\omega_{\mathrm{d}1}T_{\mathrm{s}}})$ for input u_1. b) Magnitude error versus the phase error between $G_{\mathrm{f}}(e^{\mathrm{j}\omega_{\mathrm{d}2}T_{\mathrm{s}}})$ and $G_{zu,\mathrm{d}}(e^{\mathrm{j}\omega_{\mathrm{d}2}T_{\mathrm{s}}})$ for input u_2.

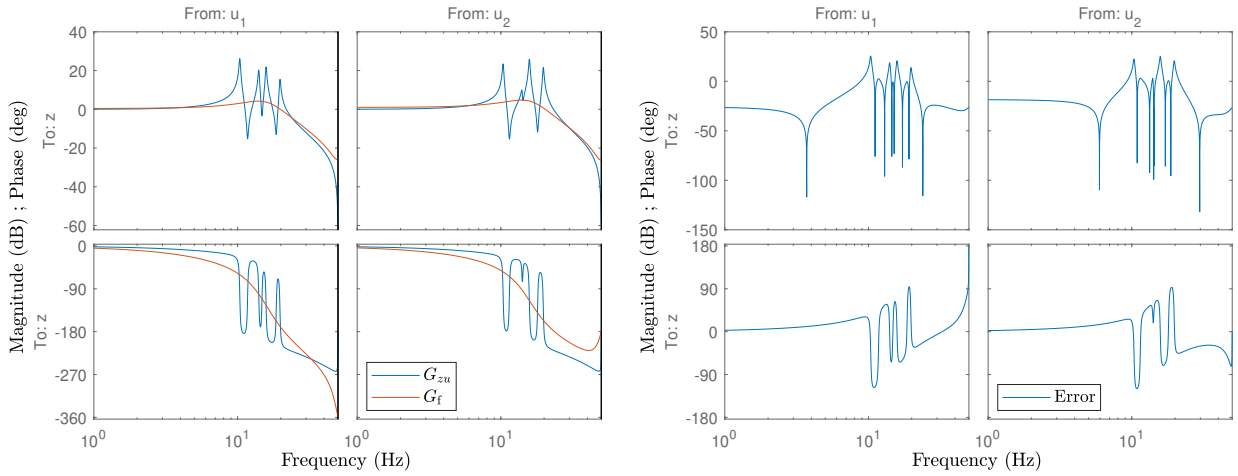

Figure 3.13: MISO example: complex windowed average dereverberated target model. a) Frequency response of the discretized G_{zu} with $\zeta = 0.01$ and the DTM G_{f} constructed from G_{zu} with $\zeta = 0.1$. The DTM was constructed by using complex windowed averaging with $\hat{n} = 2$, $\Delta = 8\pi$ rad s^{-1}, and $\beta = 0.8$. b) Error between the frequency response of the discretized G_{zu} and the DTM G_{f}.

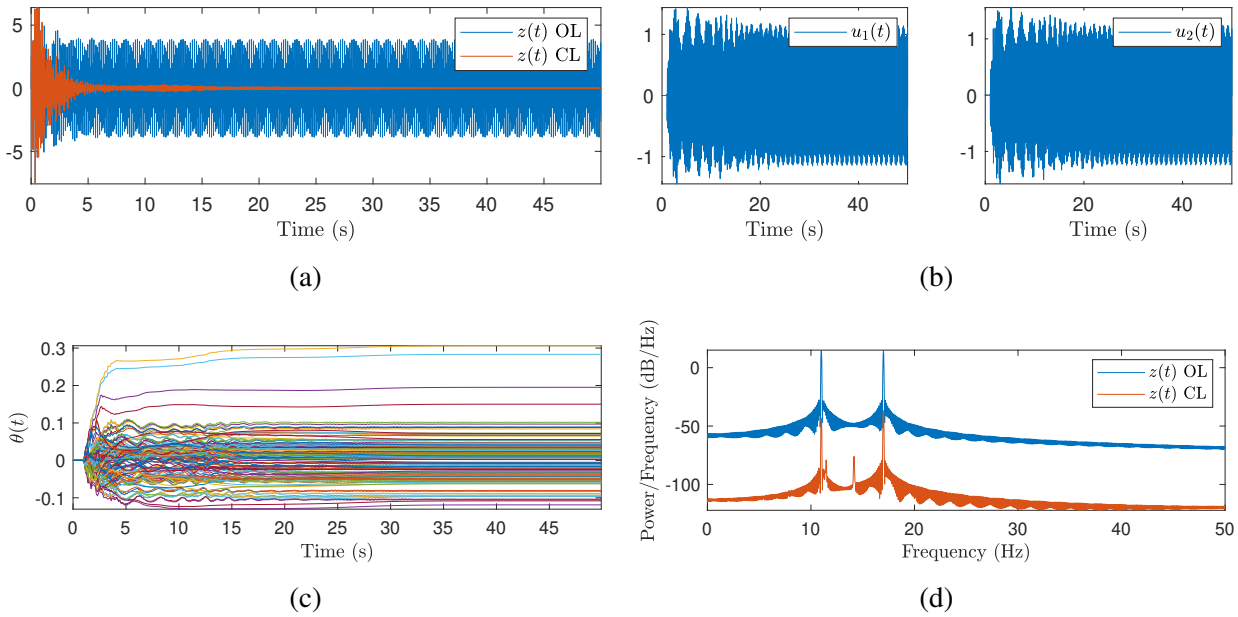

Figure 3.14: MISO adaptive disturbance rejection using complex windowed average dereverberated target model. a) Open-loop and closed-loop response of the structure subject to the harmonic disturbance, where RCAC starts at 1 s. b) Control inputs. c) Controller coefficients. d) Power spectral density of the open- and closed-loop responses. Notice that the 2 peaks in the open-loop response corresponding to the disturbance are suppressed by 58 dB and 52 dB.

3.3.2.2 Optimization

The optimization method is used with $\hat{n}_{\max} = 2$, and $\beta = 0.8$. RCAC is initialized with $n_c = 20$, $\theta_0 = 0_{l_\theta}$, $k_w = 5n_c$, $\alpha = 0.2$, and $R = 0$. Figure 3.15 shows the resulting magnitude of the asymptotic closed-loop response at the sample times along with the magnitude error versus the phase error between $G_f(e^{j\omega_d T_s})$ and $G_{zu,d}(e^{j\omega_d T_s})$ for 50 values of ζ from 0.01 to 0.5. For $\zeta = 0.01$, Figure 3.16 compares the structure and the dereverberated target model constructed from the $\zeta = 0.1$ model, with the resulting closed-loop response shown in Figure 3.17.

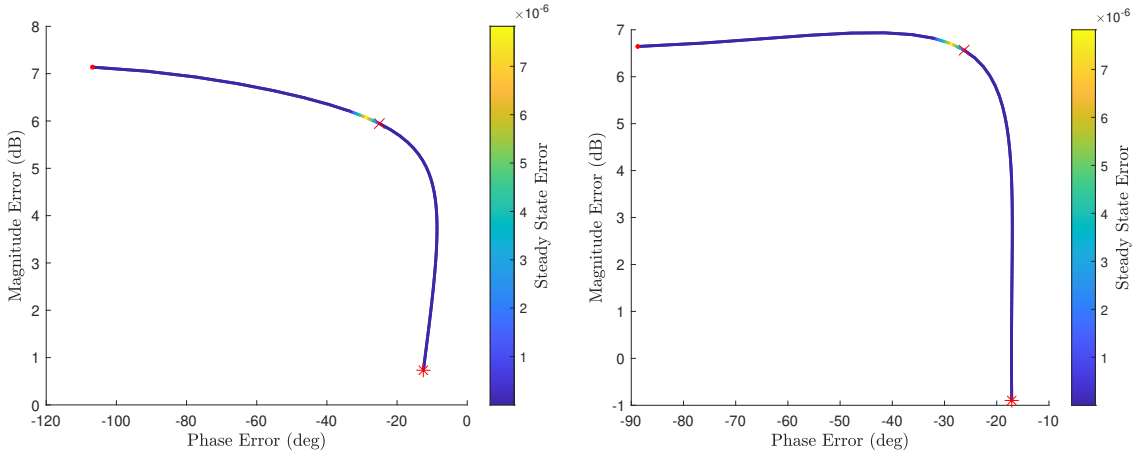

(a) (b)

Figure 3.15: MISO example: optimization based dereverberated target model. Magnitude of the asymptotic closed-loop response at the sample instances along with the magnitude error versus the phase error between $G_f(e^{j\omega_d T_s})$ and $G_{zu,d}(e^{j\omega_d T_s})$ at the disturbance frequency of the respective channel as ζ is swept between 0.01 to 0.5 when using G_f computed from the $\zeta = 0.1$ model. The labeling and symbols is the same as in Figure 3.12

3.4 Retrospective Cost Adaptive Control With Instantaneous Cost

Due to the high computational cost of RLS, it can sometimes be advantageous to implement a modified version of RCAC with a lower computational cost for experimental applications using a gradient based update. Specifically, the controller coefficients θ are now updated by minimizing the cost function

$$J_k(\theta) \triangleq \frac{1}{2}(\hat{z}_k(\theta)^T \hat{z}_k(\theta) + \theta^T R \theta), \tag{3.51}$$

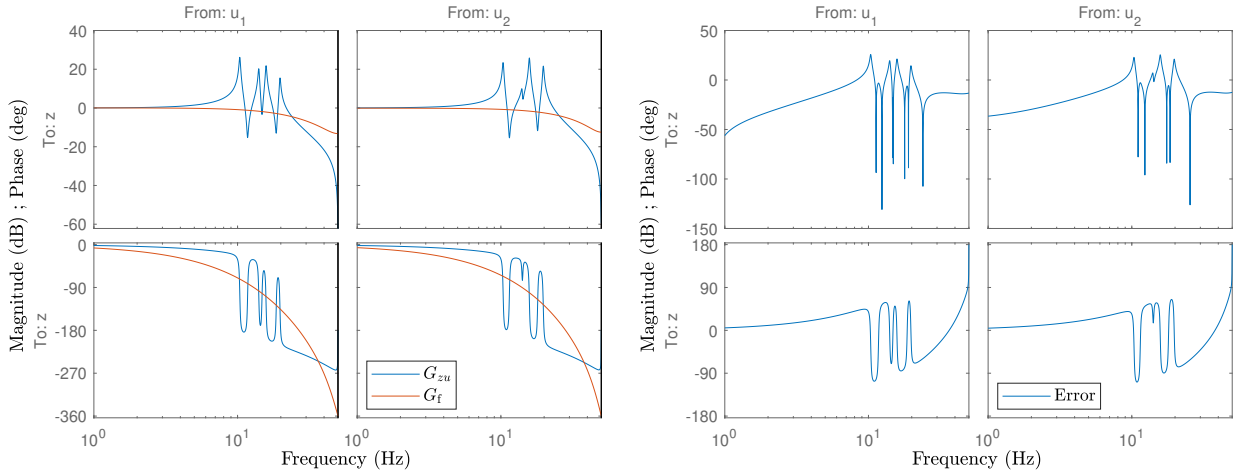

(a) (b)

Figure 3.16: MISO example: optimization based dereverberated target model. a) Frequency response of the discretized G_{zu} with $\zeta = 0.01$ and the DTM G_f constructed from G_{zu} with $\zeta = 0.1$. The DTM was constructed by using the optimization based method with $\hat{n}_{\max} = 2$, and $\beta = 0.8$. b) Error between the frequency response of the discretized G_{zu} and the DTM G_f.

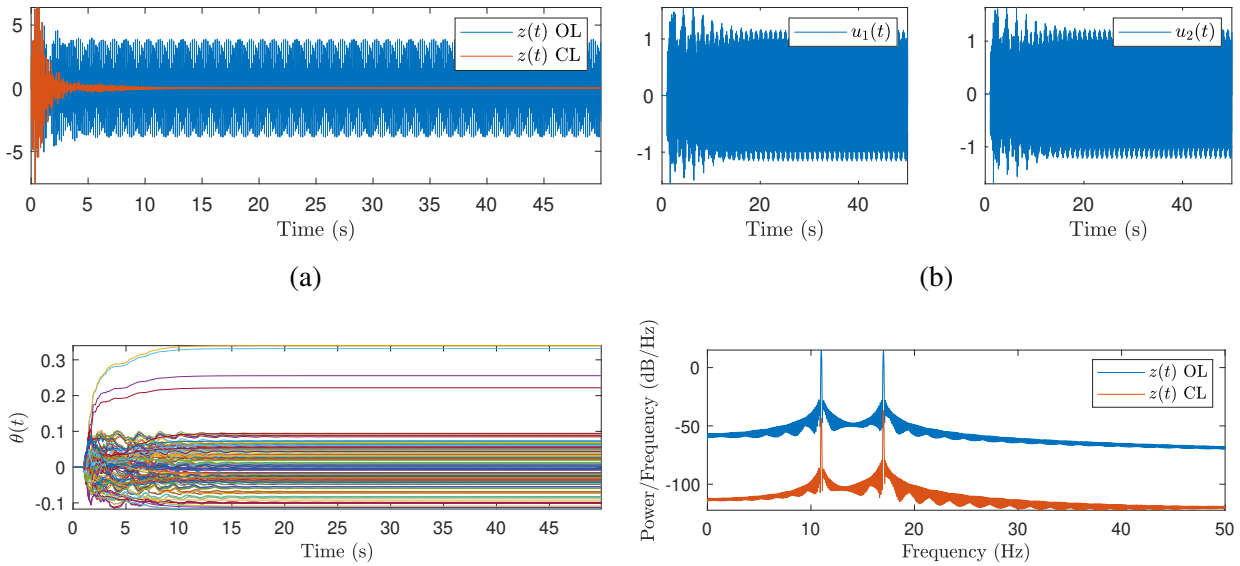

(a) (b) (c) (d)

Figure 3.17: MISO adaptive disturbance rejection using optimization based dereverberated target model. a) Open-loop and closed-loop response of the structure subject to the harmonic disturbance, where RCAC starts at 1 s. b) Control inputs. c) Controller coefficients. d) Power spectral density of the open- and closed-loop responses. Notice that the 2 peaks in the open-loop response corresponding to the disturbance are suppressed by 59 dB and 52 dB.

using gradient descent, where the positive-definite matrix $R \in \mathbb{R}^{l_\theta \times l_\theta}$ is a regularization term.

The gradient of (3.51) is given by

$$\nabla J_k(\theta) = \Phi_{\mathrm{f},k}^{\mathrm{T}} \hat{z}_k(\theta) + R\theta. \tag{3.52}$$

Let θ_k denote the current value of θ, and let $\mu_k > 0$ denote the step size used to update θ_k, that is,

$$\theta_{k+1} = \theta_k - \mu_k \nabla J_k(\theta_k), \tag{3.53}$$

$$= \theta_k - \mu_k (\Phi_{\mathrm{f},k}^{\mathrm{T}} \hat{z}_k(\theta_k) + R\theta_k). \tag{3.54}$$

Defining

$$\begin{aligned}
g(\mu_k) &\triangleq J_k(\theta_k - \mu_k(\Phi_{\mathrm{f},k}^{\mathrm{T}} \hat{z}_k(\theta_k) + R\theta_k)), \\
&= \tfrac{1}{2} \nabla J_k(\theta_k)^{\mathrm{T}} (\Phi_{\mathrm{f},k}^{\mathrm{T}} \Phi_{\mathrm{f},k} + R) \nabla J_k(\theta_k) \mu_k^2 \\
&\quad - [\nabla J_k(\theta_k)^{\mathrm{T}} (\Phi_{\mathrm{f},k}^{\mathrm{T}} \Phi_{\mathrm{f},k} + R)\theta_k + (z_k - u_{\mathrm{f}})^{\mathrm{T}} \Phi_{\mathrm{f},k} \nabla J_k(\theta_k))] \mu_k \\
&\quad + \tfrac{1}{2} \theta_k^{\mathrm{T}} \Phi_{\mathrm{f},k}^{\mathrm{T}} \Phi_{\mathrm{f},k} \theta_k + (z_k - u_{\mathrm{f}})^{\mathrm{T}} \Phi_{\mathrm{f},k} \theta_k \\
&\quad + \tfrac{1}{2} (z_k(\theta_k)^{\mathrm{T}} z_k(\theta_k) - 2 z_k(\theta_k)^{\mathrm{T}} u_{\mathrm{f},k} + u_{\mathrm{f},k}^{\mathrm{T}} u_{\mathrm{f},k}) + \tfrac{1}{2} \theta_k^{\mathrm{T}} R \theta_k, \\
&= \tfrac{1}{2} \nabla J_k(\theta_k)^{\mathrm{T}} (\Phi_{\mathrm{f},k}^{\mathrm{T}} \Phi_{\mathrm{f},k} + R) \nabla J_k(\theta_k) \mu_k^2 \\
&\quad - [\nabla J_k(\theta_k)^{\mathrm{T}} \Phi_{\mathrm{f},k}^{\mathrm{T}} \hat{z}_k(\theta_k) + \nabla J_k(\theta_k)^{\mathrm{T}} R \theta_k] \mu_k + J_k(\theta_k), \\
&= \tfrac{1}{2} [(\Phi_{\mathrm{f},k}^{\mathrm{T}} \hat{z}_k(\theta_k) + R\theta_k)^{\mathrm{T}} (\Phi_{\mathrm{f},k}^{\mathrm{T}} \Phi_{\mathrm{f},k} + R)(\Phi_{\mathrm{f},k}^{\mathrm{T}} \hat{z}_k(\theta_k) + R\theta_k)] \mu_k^2 \\
&\quad - [(\Phi_{\mathrm{f},k}^{\mathrm{T}} \hat{z}_k(\theta_k) + R\theta_k)^{\mathrm{T}} (\Phi_{\mathrm{f},k}^{\mathrm{T}} \hat{z}_k(\theta_k) + R\theta_k)] \mu_k + J_k(\theta_k),
\end{aligned} \tag{3.55}$$

it follows that

$$\begin{aligned}
g'(\mu_k) = [(\Phi_{\mathrm{f},k}^{\mathrm{T}} \hat{z}_k(\theta_k) + R\theta_k)^{\mathrm{T}} (\Phi_{\mathrm{f},k}^{\mathrm{T}} \Phi_{\mathrm{f},k} + R)(\Phi_{\mathrm{f},k}^{\mathrm{T}} \hat{z}_k(\theta_k) + R\theta_k)] \mu_k, \\
- [(\Phi_{\mathrm{f},k}^{\mathrm{T}} \hat{z}_k(\theta_k) + R\theta_k)^{\mathrm{T}} (\Phi_{\mathrm{f},k}^{\mathrm{T}} \hat{z}_k(\theta_k) + R\theta_k)].
\end{aligned} \tag{3.56}$$

An optimal adaptive steps size $\mu_{\mathrm{opt},k}$ is found by setting $g'(\mu_k) = 0$ and assuming that $(\Phi_{\mathrm{f},k}^{\mathrm{T}} \hat{z}_k(\theta_k) + R\theta_k) \neq 0$ yielding

$$\mu_{\mathrm{opt},k} \triangleq \frac{(\Phi_{\mathrm{f},k}^{\mathrm{T}} \hat{z}_k(\theta_k) + R\theta_k)^{\mathrm{T}} (\Phi_{\mathrm{f},k}^{\mathrm{T}} \hat{z}_k(\theta_k) + R\theta_k)}{(\Phi_{\mathrm{f},k}^{\mathrm{T}} \hat{z}_k(\theta_k) + R\theta_k)^{\mathrm{T}} (\Phi_{\mathrm{f},k}^{\mathrm{T}} \Phi_{\mathrm{f},k} + R)(\Phi_{\mathrm{f},k}^{\mathrm{T}} \hat{z}_k(\theta_k) + R\theta_k)}. \tag{3.57}$$

The corresponding update law for the controller coefficient vector using the optimal step size is

then given by

$$\theta_{k+1} = \theta_k - \mu_{\text{opt},k}(\Phi_{\text{f},k}^{\mathrm{T}}\hat{z}_k(\theta_k) + R\theta_k), \tag{3.58}$$

Additionally, we can derive a suboptimal step size using the inequality

$$\begin{aligned}(\Phi_{\text{f},k}^{\mathrm{T}}\hat{z}_k(\theta_k) + R\theta_k)^{\mathrm{T}}(\Phi_{\text{f},k}^{\mathrm{T}}\Phi_{\text{f},k} + R)(\Phi_{\text{f},k}^{\mathrm{T}}\hat{z}_k(\theta_k) + R\theta_k),& \\ \leq \sigma_{\max}(\Phi_{\text{f},k}^{\mathrm{T}}\Phi_{\text{f},k} + R)\|\Phi_{\text{f},k}^{\mathrm{T}}\hat{z}_k(\theta_k) + R\theta_k\|^2,&\end{aligned} \tag{3.59}$$

which leads to the suboptimal step size

$$\mu_{\sigma,k} \triangleq \frac{1}{\sigma_{\max}(\Phi_{\text{f},k}^{\mathrm{T}}\Phi_{\text{f},k} + R)} \leq \mu_{\text{opt},k}. \tag{3.60}$$

Additional computational savings are obtained by replacing the maximum singular value by the Frobenius norm, that is,

$$\mu_{\text{F},k} \triangleq \frac{1}{\|\Phi_{\text{f},k}^{\mathrm{T}}\Phi_{\text{f},k} + R\|_{\text{F}}} \leq \mu_{\sigma,k}. \tag{3.61}$$

Combining (3.60) and (3.61) yields

$$\mu_{\text{F},k} \leq \mu_{\sigma,k} \leq \mu_{\text{opt},k}. \tag{3.62}$$

The above step sizes may be too aggressive during the initial steps of RCAC when limited data is available, therefore we can multiply (3.57), (3.60), and (3.61) by a tunable parameter $\alpha \in (0, 1]$ to adjust the adaptation speed. Multiplying (3.61) by α and setting $R = 0_{l_\theta}$ results in the step size used in Section 3.5

$$\mu_{\text{Exp},k} = \frac{\alpha}{\|\Phi_{\text{f},k}\|_{\text{F}}^2}. \tag{3.63}$$

3.5 Lab Acoustic Experiment

RCAC with a dereverberated target model is now implemented in an acoustic experiment. The experiment consists of an omnidirectional microphone with three mid-bass speakers in a 6 ft × 3 ft × 3 ft enclosed space shown in Figure 3.18. One speaker w_1 is used to generate the harmonic disturbance, with the other two speakers u_1 and u_2 being available for control. The RCAC algorithm is implemented using a dSPACE SCALEXIO at a sample rate of 8 kHz. The SCALEXIO is also used to generate the harmonic disturbance consisting of seven tones at 0.8, 0.9, 1.06, 1.3, 1.6, 2.2, and 3 kHz. Note that the frequency, amplitude, and phase of the harmonic disturbance are assumed to be unknown.

The nature of the acoustic experiment leads to multi-sample delays. Once a frequency response of the system is identified, the delays are characterized and removed to facilitate the optimization procedure used to create the DTF. At 8 kHz, the delays from inputs u_1 and u_2 to the microphone corresponded to 9 and 16 samples respectively. The resulting frequency response without delays is used to generate the DTF. The 9 and 16 sample delays were then added to the appropriate inputs in the DTF to create the target model.

Due to computational constraints, a modified version of RCAC was implemented for the experiment. Specifically, the controller coefficients θ are now updated by minimizing the cost function (3.51) with $R = 0_{l_\theta}$ and using the update law (3.52) with $\mu_k = \mu_{\text{Exp},k}$.

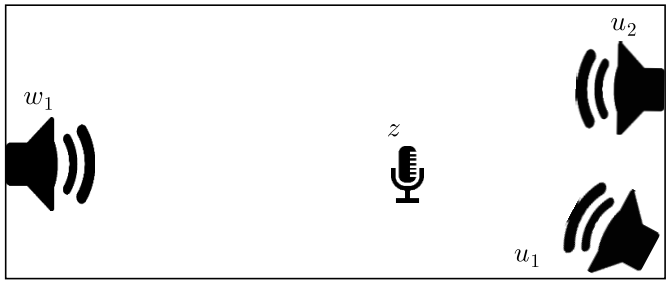

(a)

(b)

Figure 3.18: Experimental Setup. a) Simplified top-down drawing. b) Image of experimental setup.

3.5.1 Complex Windowed Averaging

The complex windowed average method is used with $\hat{n} = 6$, $\Delta = 1000\pi$ rad s^{-1}, and $\beta = \gamma = 1$. RCAC is initialized with $n_c = 50$, $\theta_0 = 0_{l_\theta}$, $k_w = 11n_c$, and $\alpha = 0.05$. Figure 3.19 compares

the acoustic experiment model and the dereverberated target model. Figure 3.20 shows that the disturbance is suppressed as the controller coefficients converge.

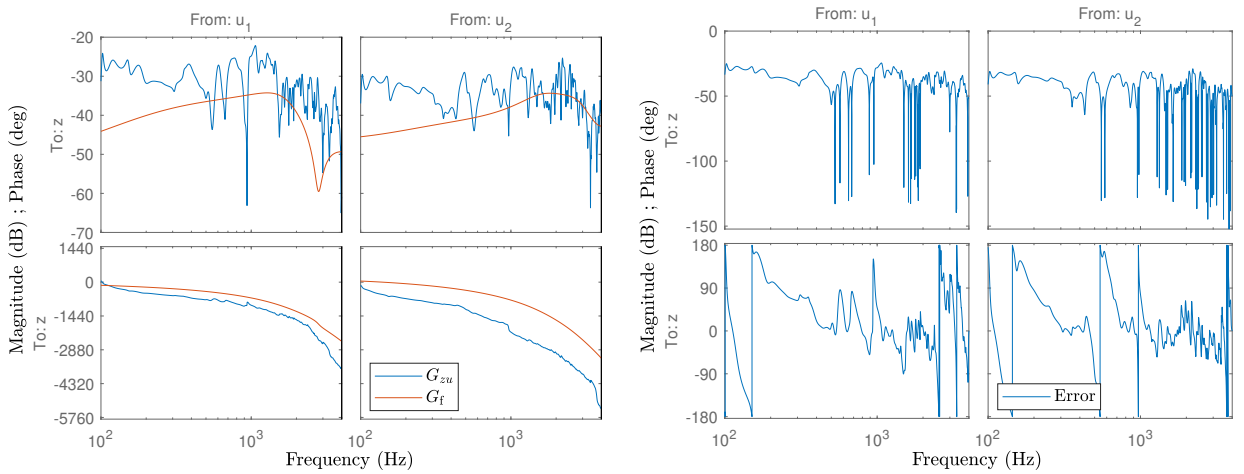

(a) (b)

Figure 3.19: Experiment: complex windowed average dereverberated target model. a) Frequency response of the discretized G_{zu} and the DTM G_{f}. The DTM was constructed by using the complex windowed average method with $\hat{n} = 6$, $\Delta = 1000\pi$ rad s^{-1}, and adding a 9 sample delay to input u_1 and 16 sample delay to input u_2. b) Error between the frequency response of the discretized G_{zu} and the DTM G_{f}.

3.5.2 Optimization

The optimization based method is used with $\hat{n}_{\max} = 6$, $\beta = 0.6$, and $\gamma = 1$. RCAC is initialized with $n_{\mathrm{c}} = 40$, $\theta_0 = 0_{l_\theta}$, $k_w = 14n_{\mathrm{c}}$, and $\alpha = 0.05$. Figure 3.21 compares the acoustic experiment model and the dereverberated target model. Figure 3.22 shows that the disturbance is suppressed as the controller coefficients converge. Large spikes in the control input occur until the controller coefficients converge at 3 seconds and convergence is slower than in complex windowed average method

3.6 Conclusions

In this chapter, two methods for identifying DTFs were formulated. For harmonic disturbance rejection in a sampled-data feedback loop, RCAC was applied numerically to adaptive disturbance rejection using a DTF as the target model. The frequency, amplitude, and phase of the harmonic disturbance were assumed to be unknown. Using the limited modeling information provided by the low-order dereverberated target model, RCAC was found to suppress the harmonic disturbance

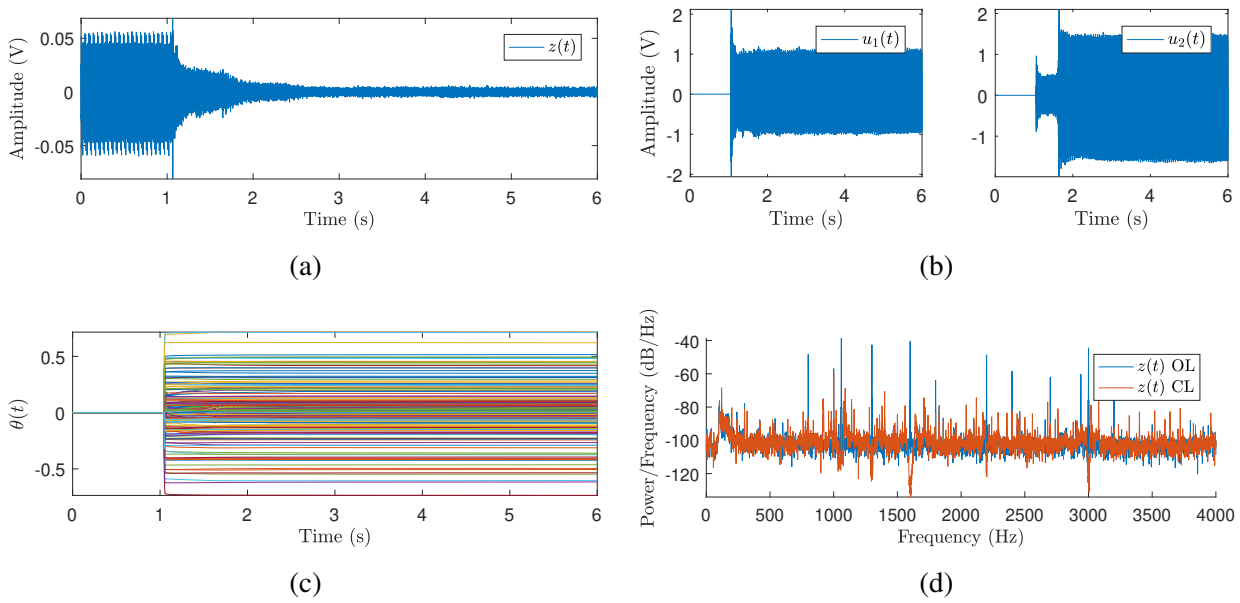

Figure 3.20: Experiment: adaptive disturbance rejection using complex windowed average dereverberated target model. a) Open-loop response and closed-loop response of the acoustic experiment subject to the harmonic disturbance, where RCAC starts at 1.05 s. b) Control inputs. c) Controller coefficients. d) Power spectral density of the open- and closed-loop responses. Notice that the 7 largest peaks in the open-loop response corresponding to the disturbance are suppressed in the closed-loop response to the noise floor. Tones from the laboratory environment are also present.

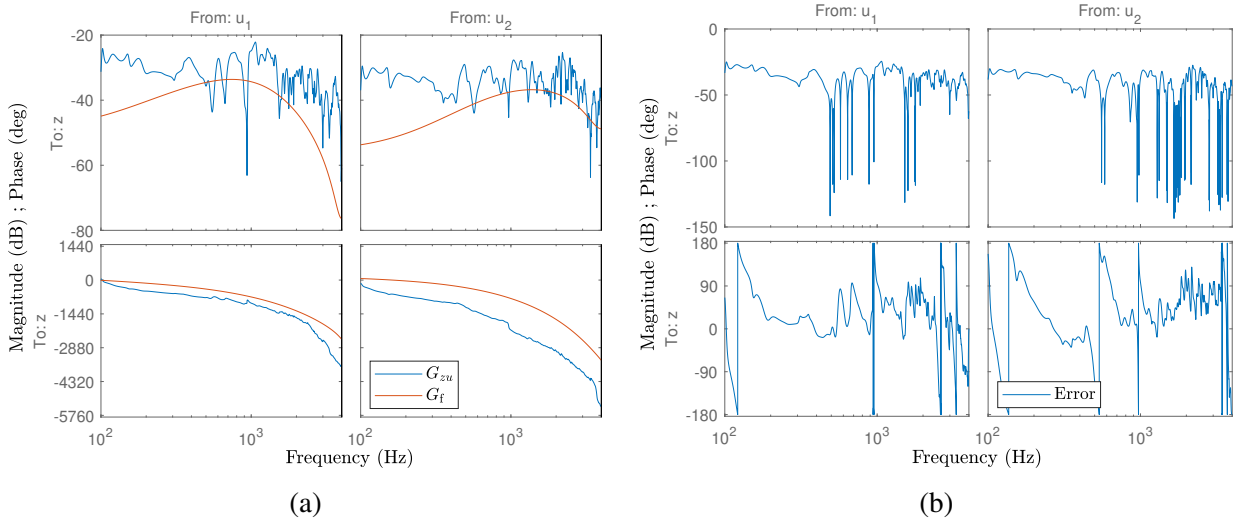

Figure 3.21: Experiment: optimization based dereverberated target model. a) Frequency response of the discretized G_{zu} and the DTM G_{f}. The DTM was constructed by using logarithmic-average error minimization with $\hat{n}_{\max} = 6$, $\beta = 0.6$, and adding a 9 sample delay to input u_1 and 16 sample delay to input u_2. b) Error between the frequency response of the discretized G_{zu} and the DTM G_{f}.

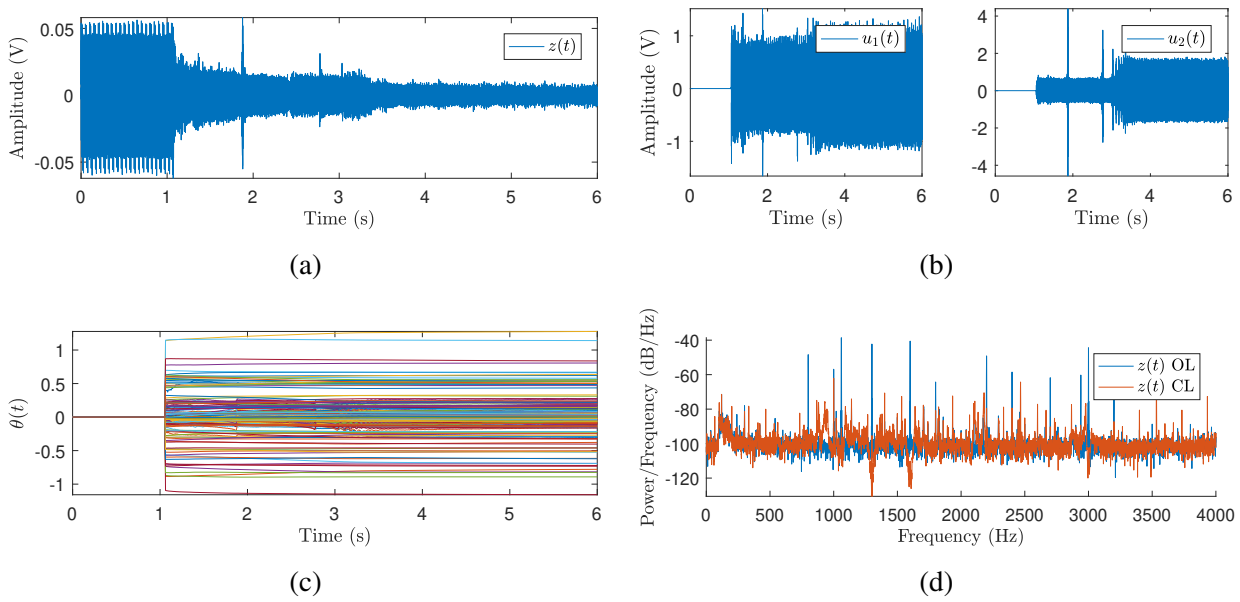

Figure 3.22: Experiment: adaptive disturbance rejection using optimization based dereverberated target model. a) Open-loop response and closed-loop response of the acoustic experiment subject to the harmonic disturbance, where RCAC starts at 1.05 s. b) Control inputs. c) Controller coefficients. d) Power spectral density of the open- and closed-loop responses. Notice that the 7 largest peaks in the open-loop response corresponding to the disturbance are suppressed in the closed-loop response to the noise floor. Tones from the laboratory environment are also present.

over a range of disturbance frequencies. In addition, for a 2-input, 1-output structure, RCAC was found to suppress the harmonic disturbance using a dereverberated target model constructed from a model with an erroneous damping ratio. RCAC was then applied to a 2-input, 1-output acoustic noise-suppression experiment. A gradient-based variation of RCAC was implemented with a dereverberated target model with 8-kHz sample rate, with seven harmonic disturbances. RCAC was found to suppress the disturbances as well as ambient disturbances present in the lab. The results show that a dereverberated target model that captures the phase and magnitude trend but not the detailed peaks and notches of the structure can be effective for disturbance rejection on lightly damped structures.

CHAPTER 4

Retrospective Cost Model Reference Adaptive Control

In this chapter we investigate the MRAC problem for systems containing NMP zeros. A relevant method for NMP systems is the APPC developed in [66, 67, 68], which can be applied to NMP systems with *unknown* NMP zeros. This is accomplished by overparameterizing the $2n$ parameter controller identification problem as a $4n$ parameter problem using a Bezout identity. The drawback of this approach is the need for sufficient persistency in order to achieve model-following, even for step commands. Although this requirement was alleviated in [69] through the use of DREM, the need for persistency is nontrivial.

This chapter develops a novel MRAC technique based on RCAC and compares it with APPC. For SISO discrete-time or sampled-data systems, RCAC requires knowledge of the sign of the leading numerator coefficient, relative degree, and NMP zeros. RCAC minimizes a retrospective performance measure based on the difference between filtered past control inputs and filtered, re-optimized past control inputs. To further reduce the dependence on prior modeling, an indirect adaptive control extension of RCAC was developed in [70].

An initial development of RC-MRAC was shown in [71] with stability analysis given in [72]. A related technique was developed in [73]. As in the case of RCAC, RC-MRAC is applicable to discrete-time and sampled-data systems with known NMP zeros; minimum-phase zeros need not be known. The goal and contribution of the present chapter is to develop RC-MRAC and assess its performance from the perspective of both command following and adaptive pole placement in comparison to APPC. Additionally, we show that, with minor modifications, RC-MRAC can perform disturbance rejection for harmonic disturbances with unknown spectra. Numerical examples show that, in contrast to [69], RC-MRAC does not require persistency. The price paid for alleviating the need for persistency is knowledge of the NMP zeros.

The structure of the chapter is as follows, Section 4.1 gives an overview of the MRAC problem, Section 4.2 gives a derivation of APPC, Section 4.3 gives a derivation of RC-MRAC, Section 4.4 shows the connection between APPC and RC-MRAC, and Sections 4.5-4.7 provide examples and

comparison of both algorithms for minimum- and NMP systems, as well as harmonic disturbance rejection.

4.1 Model Reference Adaptive Control

Consider the discrete-time SISO system

$$y_k = \frac{N(\mathbf{q}^{-1})}{D(\mathbf{q}^{-1})} u_k, \tag{4.1}$$

where

$$N(\mathbf{q}^{-1}) \triangleq \sum_{i=n_\mathrm{r}}^{n} N_i \mathbf{q}^{-i}, \tag{4.2}$$

$$D(\mathbf{q}^{-1}) \triangleq 1 + \sum_{i=1}^{n} D_i \mathbf{q}^{-i}, \tag{4.3}$$

are coprime, $N_{n_\mathrm{r}} \neq 0$, and n_r is the relative degree of $\frac{N(\mathbf{q}^{-1})}{D(\mathbf{q}^{-1})}$ as a rational function of $\mathbf{q}$. In the MRAC problem, the goal is to find a controller $G_\mathrm{c}(\mathbf{q}^{-1})$ such that the output y_k follows the desired reference response $y_{\mathrm{m},k}$ to a command r_k given by

$$y_{\mathrm{m},k} = \frac{N_\mathrm{m}(\mathbf{q}^{-1})}{D_\mathrm{m}(\mathbf{q}^{-1})} r_k, \tag{4.4}$$

where

$$N_\mathrm{m}(\mathbf{q}^{-1}) \triangleq \sum_{i=n_\mathrm{r}}^{n} N_{\mathrm{m},i} \mathbf{q}^{-i}, \tag{4.5}$$

$$D_\mathrm{m}(\mathbf{q}^{-1}) \triangleq 1 + \sum_{i=1}^{n} D_{\mathrm{m},i} \mathbf{q}^{-i}. \tag{4.6}$$

As shown in Figure 4.1, the error e_k between the actual plant response y_k and the reference model response $y_{\mathrm{m},k}$ is used to update the controller. The direct MRAC problem differs from the indirect case in that the plant is not identified, but knowledge of the NMP zeros of (4.1) is typically needed to prevent unstable pole-zero cancellation.

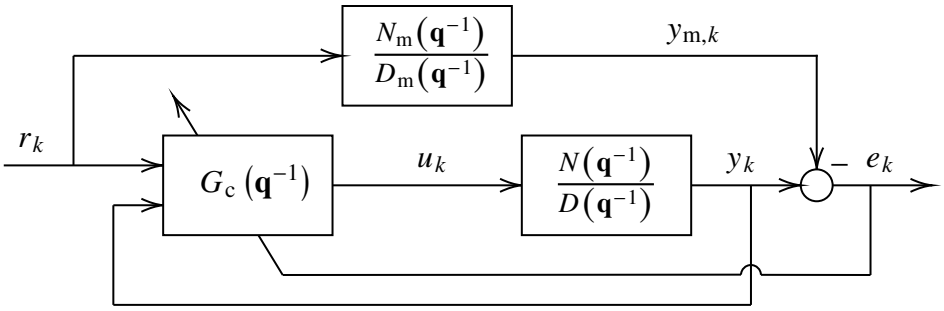

Figure 4.1: Block diagram of the direct model reference adaptive control problem.

4.2 Adaptive Pole Placement Control

The APPC developed in [66, 67] addresses the MRAC problem in the case where $N_{\mathrm{m}}(\mathbf{q}^{-1}) = N(\mathbf{q}^{-1})$. Through the use of a Bezout identity, no knowledge of the NMP zeros of the plant is needed and only the plant order n needs to be known. This comes at the cost of higher persistency of excitation requirements which has been previously demonstrated [69]. For reference, APPC is summarized below.

4.2.1 APPC Derivation

Defining

$$x_k \triangleq \frac{1}{D(\mathbf{q}^{-1})} u_k, \tag{4.7}$$

which satisfies

$$D(\mathbf{q}^{-1}) x_k = u_k, \tag{4.8}$$

it follows that (4.1) can be written as

$$y_k = N(\mathbf{q}^{-1}) x_k. \tag{4.9}$$

For the command r_k, consider the controller

$$u_k = N_{\mathrm{c}}(\mathbf{q}^{-1}) y_k + D_{\mathrm{c}}(\mathbf{q}^{-1}) u_k + H(\mathbf{q}^{-1}) r_k, \tag{4.10}$$

where

$$N_{\mathrm{c}}(\mathbf{q}^{-1}) \triangleq \sum_{i=1}^{n} N_{\mathrm{c},i}\mathbf{q}^{-i}, \tag{4.11}$$

$$D_{\mathrm{c}}(\mathbf{q}^{-1}) \triangleq \sum_{i=1}^{n} D_{\mathrm{c},i}\mathbf{q}^{-i}, \tag{4.12}$$

$$H(\mathbf{q}^{-1}) \triangleq 1 + \sum_{i=1}^{n} H_i\mathbf{q}^{-i}, \tag{4.13}$$

and $H(\mathbf{q}^{-1})$ is an asymptotically stable monic polynomial as a function of $\mathbf{q}$. Combining (4.8), (4.9), and (4.10) yields

$$D(\mathbf{q}^{-1})x_k = N_{\mathrm{c}}(\mathbf{q}^{-1})N(\mathbf{q}^{-1})x_k + D_{\mathrm{c}}(\mathbf{q}^{-1})D(\mathbf{q}^{-1})x_k + H(\mathbf{q}^{-1})r_k, \tag{4.14}$$

which implies

$$x_k = \frac{H(\mathbf{q}^{-1})}{\tilde{D}(\mathbf{q}^{-1})}r_k, \tag{4.15}$$

where

$$\tilde{D}(\mathbf{q}^{-1}) \triangleq D(\mathbf{q}^{-1}) - N_{\mathrm{c}}(\mathbf{q}^{-1})N(\mathbf{q}^{-1}) - D_{\mathrm{c}}(\mathbf{q}^{-1})D(\mathbf{q}^{-1}). \tag{4.16}$$

Proposition 4.2.1. *Let the desired closed-loop poles be the roots of*

$$D_{\mathrm{m}}(\mathbf{q}^{-1}) = 1 + \sum_{i=1}^{n} D_{\mathrm{m},i}\mathbf{q}^{-i}, \tag{4.17}$$

and assume there exist $N_{\mathrm{c}}^*(\mathbf{q}^{-1})$ and $D_{\mathrm{c}}^*(\mathbf{q}^{-1})$ such that

$$D_{\mathrm{m}}(\mathbf{q}^{-1})H(\mathbf{q}^{-1}) = \tilde{D}^*(\mathbf{q}^{-1}), \tag{4.18}$$

where

$$\tilde{D}^*(\mathbf{q}^{-1}) \triangleq D(\mathbf{q}^{-1}) - N_{\mathrm{c}}^*(\mathbf{q}^{-1})N(\mathbf{q}^{-1}) - D_{\mathrm{c}}^*(\mathbf{q}^{-1})D(\mathbf{q}^{-1}). \tag{4.19}$$

Then, the closed-loop dynamics are given by

$$y_k = \frac{N(\mathbf{q}^{-1})}{D_{\mathrm{m}}(\mathbf{q}^{-1})}r_k. \tag{4.20}$$

Proof. Using (4.9), (4.15) with $\tilde{D}(\mathbf{q}^{-1}) = \tilde{D}^*(\mathbf{q}^{-1})$, and (4.18),

$$y_k = N(\mathbf{q}^{-1})x_k = \frac{N(\mathbf{q}^{-1})H(\mathbf{q}^{-1})}{\tilde{D}^*(\mathbf{q}^{-1})}r_k = \frac{N(\mathbf{q}^{-1})H(\mathbf{q}^{-1})}{D_{\mathrm{m}}(\mathbf{q}^{-1})H(\mathbf{q}^{-1})}r_k = \frac{N(\mathbf{q}^{-1})}{D_{\mathrm{m}}(\mathbf{q}^{-1})}r_k. \tag{4.21}$$

Note that, although the numerator of the closed loop dynamics (4.21) is $N(\mathbf{q}^{-1})$, Proposition 4.2.1 does not require knowledge of $N(\mathbf{q}^{-1})$. □

Proposition 4.2.2. *Let $B^*(\mathbf{q}^{-1})$ and $C^*(\mathbf{q}^{-1})$ satisfy the Bezout identity*

$$1 = B^*(\mathbf{q}^{-1})N(\mathbf{q}^{-1}) + C^*(\mathbf{q}^{-1})D(\mathbf{q}^{-1}), \tag{4.22}$$

where

$$B^*(\mathbf{q}^{-1}) \triangleq \sum_{i=1}^{n} B_i^*\mathbf{q}^{-i}, \tag{4.23}$$

$$C^*(\mathbf{q}^{-1}) \triangleq 1 + \sum_{i=1}^{n} C_i^*\mathbf{q}^{-i}. \tag{4.24}$$

Then,

$$\begin{aligned} &D_{\mathrm{m}}(\mathbf{q}^{-1})H(\mathbf{q}^{-1})[\tilde{B}(\mathbf{q}^{-1})y_k + \tilde{C}(\mathbf{q}^{-1})u_k] + [\tilde{N}_{\mathrm{c}}(\mathbf{q}^{-1})y_k + \tilde{D}_{\mathrm{c}}(\mathbf{q}^{-1})u_k] \\ &\quad = D_{\mathrm{m}}(\mathbf{q}^{-1})H(\mathbf{q}^{-1})[\hat{B}(\mathbf{q}^{-1})y_k + \hat{C}(\mathbf{q}^{-1})u_k] - [u_k - \hat{N}_{\mathrm{c}}(\mathbf{q}^{-1})y_k - \hat{D}_{\mathrm{c}}(\mathbf{q}^{-1})u_k], \end{aligned} \tag{4.25}$$

where

$$\tilde{B}(\mathbf{q}^{-1}) \triangleq \hat{B}(\mathbf{q}^{-1}) - B^*(\mathbf{q}^{-1}), \tag{4.26}$$

$$\tilde{C}(\mathbf{q}^{-1}) \triangleq \hat{C}(\mathbf{q}^{-1}) - C^*(\mathbf{q}^{-1}), \tag{4.27}$$

$$\tilde{N}_{\mathrm{c}}(\mathbf{q}^{-1}) \triangleq \hat{N}_{\mathrm{c}}(\mathbf{q}^{-1}) - N_{\mathrm{c}}^*(\mathbf{q}^{-1}), \tag{4.28}$$

$$\tilde{D}_{\mathrm{c}}(\mathbf{q}^{-1}) \triangleq \hat{D}_{\mathrm{c}}(\mathbf{q}^{-1}) - D_{\mathrm{c}}^*(\mathbf{q}^{-1}). \tag{4.29}$$

Proof. Multiplying both sides of (4.19) by x_k, and using (4.8), (4.9), and (4.18) yields

$$D_{\mathrm{m}}(\mathbf{q}^{-1})H(\mathbf{q}^{-1})x_k = u_k - N_{\mathrm{c}}^*(\mathbf{q}^{-1})y_k - D_{\mathrm{c}}^*(\mathbf{q}^{-1})u_k. \tag{4.30}$$

Multiplying both sides of (4.22) by x_k and using (4.8) and (4.9) yields

$$x_k = B^*(\mathbf{q}^{-1})y_k + C^*(\mathbf{q}^{-1})u_k. \tag{4.31}$$

Substituting (4.31) into (4.30) yields

$$D_{\mathrm{m}}(\mathbf{q}^{-1})H(\mathbf{q}^{-1})[B^*(\mathbf{q}^{-1})y_k + C^*(\mathbf{q}^{-1})u_k] = u_k - N_{\mathrm{c}}^*(\mathbf{q}^{-1})y_k - D_{\mathrm{c}}^*(\mathbf{q}^{-1})u_k. \tag{4.32}$$

Finally, substituting (4.26)-(4.29) into (4.32) yields (4.25). □

Note that all the terms on the right-hand side of (4.25) are known, and thus the sum of terms on the left-hand side is known despite the fact that $\tilde{N}_{\mathrm{c}}(\mathbf{q}^{-1})$, $\tilde{D}_{\mathrm{c}}(\mathbf{q}^{-1})$, $\tilde{B}(\mathbf{q}^{-1})$ and $\tilde{C}(\mathbf{q}^{-1})$ are individually unknown. Furthermore, if (4.26)-(4.29) are all zero, then both sides of (4.25) are zero. We thus define the performance variable

$$\begin{aligned} z_k &\triangleq D_{\mathrm{m}}(\mathbf{q}^{-1})H(\mathbf{q}^{-1})[\hat{B}(\mathbf{q}^{-1})y_k + \hat{C}(\mathbf{q}^{-1})u_k] - [u_k - \hat{N}_{\mathrm{c}}(\mathbf{q}^{-1})y_k - \hat{D}_{\mathrm{c}}(\mathbf{q}^{-1})u_k] && (4.33)\\ &= D_{\mathrm{m}}(\mathbf{q}^{-1})H(\mathbf{q}^{-1})[\tilde{B}(\mathbf{q}^{-1})y_k + \tilde{C}(\mathbf{q}^{-1})u_k] + [\tilde{N}_{\mathrm{c}}(\mathbf{q}^{-1})y_k + \tilde{D}_{\mathrm{c}}(\mathbf{q}^{-1})u_k]. && (4.34)\end{aligned}$$

Note that, if $\tilde{N}_{\mathrm{c}}(\mathbf{q}^{-1})$, $\tilde{D}_{\mathrm{c}}(\mathbf{q}^{-1})$, $\tilde{B}(\mathbf{q}^{-1})$, and $\tilde{C}(\mathbf{q}^{-1})$ are all zero, then z_k is zero. We thus seek estimates $\hat{N}_{\mathrm{c}}(\mathbf{q}^{-1})$, $\hat{D}_{\mathrm{c}}(\mathbf{q}^{-1})$, $\hat{B}(\mathbf{q}^{-1})$ and $\hat{C}(\mathbf{q}^{-1})$ of $N_{\mathrm{c}}^*(\mathbf{q}^{-1})$, $D_{\mathrm{c}}^*(\mathbf{q}^{-1})$, $B^*(\mathbf{q}^{-1})$ and $C^*(\mathbf{q}^{-1})$, respectively, that minimize the magnitude of z_k.

4.2.2 APPC Algorithm

Proposition 4.2.3. *Define*

$$\theta_1 \triangleq \begin{bmatrix} N_{\mathrm{c},1}^* & \cdots & N_{\mathrm{c},n}^* & D_{\mathrm{c},1}^* & \cdots & D_{\mathrm{c},n}^* \end{bmatrix}^{\mathrm{T}}, \tag{4.35}$$

$$\theta_2 \triangleq \begin{bmatrix} B_{\mathrm{c},1}^* & \cdots & B_{\mathrm{c},n}^* & C_{\mathrm{c},1}^* & \cdots & C_{\mathrm{c},n}^* \end{bmatrix}^{\mathrm{T}}. \tag{4.36}$$

Then,

$$\begin{bmatrix} \Phi_k & \Phi_{\mathrm{f},k} \end{bmatrix} \begin{bmatrix} \theta_1 \\ \theta_2 \end{bmatrix} + u_{\mathrm{f},k} = 0, \tag{4.37}$$

where

$$\Phi_k \triangleq \begin{bmatrix} y_{k-1} & \cdots & y_{k-n} & u_{k-1} & \cdots & u_{k-n} \end{bmatrix}, \tag{4.38}$$

$$\Phi_{\mathrm{f},k} \triangleq D_{\mathrm{m}}(\mathbf{q}^{-1})H(\mathbf{q}^{-1})\Phi_k, \tag{4.39}$$

$$u_{\mathrm{f},k} \triangleq [D_{\mathrm{m}}(\mathbf{q}^{-1})H(\mathbf{q}^{-1}) - 1]u_k. \tag{4.40}$$

Since $N_{\mathrm{c}}^*(\mathbf{q}^{-1})$, $D_{\mathrm{c}}^*(\mathbf{q}^{-1})$, $B^*(\mathbf{q}^{-1})$ and $C^*(\mathbf{q}^{-1})$ are unknown, the goal is to solve the regression (4.37) at each step k to obtain estimates $\hat{\theta}_{1,k}$ and $\hat{\theta}_{2,k}$ of the polynomial coefficients θ_1 and θ_2,

respectively. The estimation error is thus given by

$$\hat{z}_k(\hat{\theta}_{1,k}, \hat{\theta}_{2,k}) \triangleq \begin{bmatrix} \Phi_k & \Phi_{\mathrm{f},k} \end{bmatrix} \begin{bmatrix} \hat{\theta}_{1,k} \\ \hat{\theta}_{2,k} \end{bmatrix} + u_{\mathrm{f},k}. \tag{4.41}$$

For regression at each step, RLS is used to minimize the cost function

$$J_k(\hat{\theta}_{1,k}, \hat{\theta}_{2,k}) \triangleq \sum_{i=1}^{k} \lambda^{k-i} [\hat{z}_i(\hat{\theta}_{1,i}, \hat{\theta}_{2,i})^{\mathrm{T}} \hat{z}_i(\hat{\theta}_{1,i}, \hat{\theta}_{2,i})] + \lambda^k (\begin{bmatrix} \hat{\theta}_{1,k} \\ \hat{\theta}_{2,k} \end{bmatrix} - \begin{bmatrix} \hat{\theta}_{1,0} \\ \hat{\theta}_{2,0} \end{bmatrix})^{\mathrm{T}} R_\theta (\begin{bmatrix} \hat{\theta}_{1,k} \\ \hat{\theta}_{2,k} \end{bmatrix} - \begin{bmatrix} \hat{\theta}_{1,0} \\ \hat{\theta}_{2,0} \end{bmatrix}), \tag{4.42}$$

where $\lambda \in (0, 1]$ is the forgetting factor. Using the computed RLS solution and (4.10), the control input at step $k + 1$ is given by

$$u_{k+1} = \Phi_{k+1} \hat{\theta}_{1,k+1} + H(\mathbf{q}^{-1}) r_{k+1}. \tag{4.43}$$

Note that the identified Bezout coefficients $\hat{B}(\mathbf{q}^{-1})$ and $\hat{C}(\mathbf{q}^{-1})$ are available from the RLS solution. However, these estimates are not used to determine the control input. In addition, $\hat{B}(\mathbf{q}^{-1})$ and $\hat{C}(\mathbf{q}^{-1})$ could be used to obtain estimates of $N(\mathbf{q}^{-1})$ and $D(\mathbf{q}^{-1})$. However, these estimates are not needed for APPC.

4.2.3 APPC Global Stability Results

The following section briefly restates the global stability results of APPC as given in [66]. Let the unknown system of order n be given by (4.1), where $N(\mathbf{q}^{-1})$ and $D(\mathbf{q}^{-1})$ are coprime. Let the command r_k be of the form

$$r_k = \sum_{i=1}^{2n} L_i e^{\jmath \omega_i k} + \overline{L}_i e^{-\jmath \omega_i k}, \tag{4.44}$$

where $L_i \neq 0 \ \forall i$, $\omega_i \neq \omega_j$ if $i \neq j$, and $\overline{L}$ is the complex conjugate of L. Let the control law be (4.43) and the identification scheme be the minimization of the cost function (4.42) using RLS at each step. Then, if L_i is chosen such that

$$\sum_{k=1}^{\infty} \begin{bmatrix} \Phi_k & \Phi_{\mathrm{f},k} \end{bmatrix}^{\mathrm{T}} \begin{bmatrix} \Phi_k & \Phi_{\mathrm{f},k} \end{bmatrix} \geq \varepsilon I_{4n}, \tag{4.45}$$

where ε is finite and positive, then u_k, y_k, and x_k are bounded, and the closed-loop system is globally stable converging to a system that satisfies (4.20).

4.3 Retrospective Cost Model Reference Adaptive Control

4.3.1 RC-MRAC Derivation

Let $N(\mathbf{q}^{-1})$ be factored as

$$N(\mathbf{q}^{-1}) = N_{n_\mathrm{r}} N_\mathrm{u}(\mathbf{q}^{-1}) N_\mathrm{s}(\mathbf{q}^{-1}) \mathbf{q}^{-n_\mathrm{r}}, \tag{4.46}$$

where $N_\mathrm{u}(\mathbf{q}^{-1})$ and $N_\mathrm{s}(\mathbf{q}^{-1})$ as a function of $\mathbf{q}$ are monic polynomials of order n_u and n_s whose roots have modulus at least 1 and less than 1, respectively. Next, consider the controller

$$u_k = N_\mathrm{c}(\mathbf{q}^{-1}) y_k + D_\mathrm{c}(\mathbf{q}^{-1}) u_k + R_\mathrm{c}(\mathbf{q}^{-1}) F(\mathbf{q}^{-1}) r_k, \tag{4.47}$$

where $N_\mathrm{c}(\mathbf{q}^{-1})$ and $D_\mathrm{c}(\mathbf{q}^{-1})$ are given by (4.11) and (4.12), and

$$R_\mathrm{c}(\mathbf{q}^{-1}) \triangleq R_{\mathrm{c},0} + \sum_{i=1}^{n_\mathrm{s}} R_{\mathrm{c},i} \mathbf{q}^{-i}, \tag{4.48}$$

$$F(\mathbf{q}^{-1}) \triangleq 1 + \sum_{i=1}^{n-n_\mathrm{s}} F_i \mathbf{q}^{-i}, \tag{4.49}$$

where $F(\mathbf{q}^{-1})$ is an arbitrary stable monic polynomial in $\mathbf{q}$. Combining (4.8), (4.9), and (4.47) yields

$$D(\mathbf{q}^{-1}) x_k = N_\mathrm{c}(\mathbf{q}^{-1}) N(\mathbf{q}^{-1}) x_k + D_\mathrm{c}(\mathbf{q}^{-1}) D(\mathbf{q}^{-1}) x_k + R_\mathrm{c}(\mathbf{q}^{-1}) F(\mathbf{q}^{-1}) r_k, \tag{4.50}$$

which implies

$$x_k = \frac{R_\mathrm{c}(\mathbf{q}^{-1}) F(\mathbf{q}^{-1})}{\tilde{D}(\mathbf{q}^{-1})} r_k, \tag{4.51}$$

where

$$\tilde{D}(\mathbf{q}^{-1}) \triangleq D(\mathbf{q}^{-1}) - N_\mathrm{c}(\mathbf{q}^{-1}) N(\mathbf{q}^{-1}) - D_\mathrm{c}(\mathbf{q}^{-1}) D(\mathbf{q}^{-1}). \tag{4.52}$$

Proposition 4.3.1. *Let the desired closed-loop poles be the roots of*

$$D_\mathrm{m}(\mathbf{q}^{-1}) = 1 + \sum_{i=1}^{n} D_{\mathrm{m},i} \mathbf{q}^{-i}, \tag{4.53}$$

and assume there exist $N_\mathrm{c}^*(\mathbf{q}^{-1})$ *and* $D_\mathrm{c}^*(\mathbf{q}^{-1})$ *such that*

$$D_\mathrm{m}(\mathbf{q}^{-1}) N_\mathrm{s}(\mathbf{q}^{-1}) F(\mathbf{q}^{-1}) = \tilde{D}^*(\mathbf{q}^{-1}), \tag{4.54}$$

where

$$\tilde{D}^*(\mathbf{q}^{-1}) \triangleq D(\mathbf{q}^{-1}) - N_{\mathrm{c}}^*(\mathbf{q}^{-1})N(\mathbf{q}^{-1}) - D_{\mathrm{c}}^*(\mathbf{q}^{-1})D(\mathbf{q}^{-1}). \tag{4.55}$$

Then, the closed-loop dynamics are given by

$$y_k = \frac{N_{n_{\mathrm{r}}}N_u(\mathbf{q}^{-1})R_{\mathrm{c}}(\mathbf{q}^{-1})\mathbf{q}^{-n_{\mathrm{r}}}}{D_{\mathrm{m}}(\mathbf{q}^{-1})}r_k. \tag{4.56}$$

Proof. Using (4.9), (4.51) with $\tilde{D}(\mathbf{q}^{-1}) = \tilde{D}^*(\mathbf{q}^{-1})$, and (4.54),

$$\begin{aligned} y_k = N(\mathbf{q}^{-1})x_k &= \frac{N(\mathbf{q}^{-1})R_{\mathrm{c}}(\mathbf{q}^{-1})F(\mathbf{q}^{-1})}{\tilde{D}^*(\mathbf{q}^{-1})}r_k = \frac{N(\mathbf{q}^{-1})R_{\mathrm{c}}(\mathbf{q}^{-1})F(\mathbf{q}^{-1})}{D_{\mathrm{m}}(\mathbf{q}^{-1})N_{\mathrm{s}}(\mathbf{q}^{-1})F(\mathbf{q}^{-1})}r_k \\ &= \frac{N_{n_{\mathrm{r}}}N_u(\mathbf{q}^{-1})R_{\mathrm{c}}(\mathbf{q}^{-1})\mathbf{q}^{-n_{\mathrm{r}}}}{D_{\mathrm{m}}(\mathbf{q}^{-1})}r_k. \end{aligned}$$

□

Proposition 4.3.2. *Assume there exists $R_{\mathrm{c}}^*(\mathbf{q}^{-1})$ such that*

$$N_{\mathrm{m}}(\mathbf{q}^{-1}) = N_{n_{\mathrm{r}}}N_u(\mathbf{q}^{-1})R_{\mathrm{c}}^*(\mathbf{q}^{-1})\mathbf{q}^{-n_{\mathrm{r}}}, \tag{4.57}$$

and let

$$\tilde{N}_{\mathrm{c}}(\mathbf{q}^{-1}) \triangleq \hat{N}_{\mathrm{c}}(\mathbf{q}^{-1}) - N_{\mathrm{c}}^*(\mathbf{q}^{-1}), \tag{4.58}$$

$$\tilde{D}_{\mathrm{c}}(\mathbf{q}^{-1}) \triangleq \hat{D}_{\mathrm{c}}(\mathbf{q}^{-1}) - D_{\mathrm{c}}^*(\mathbf{q}^{-1}), \tag{4.59}$$

$$\tilde{R}_{\mathrm{c}}(\mathbf{q}^{-1}) \triangleq \hat{R}_{\mathrm{c}}(\mathbf{q}^{-1}) - R_{\mathrm{c}}^*(\mathbf{q}^{-1}). \tag{4.60}$$

Then,

$$\begin{aligned} &N_{n_{\mathrm{r}}}N_u(\mathbf{q}^{-1})\mathbf{q}^{-n_{\mathrm{r}}}[\tilde{N}_{\mathrm{c}}(\mathbf{q}^{-1})y_k + \tilde{D}_{\mathrm{c}}(\mathbf{q}^{-1})u_k + \tilde{R}_{\mathrm{c}}(\mathbf{q}^{-1})r_k] \\ &\quad = D_{\mathrm{m}}(\mathbf{q}^{-1})F(\mathbf{q}^{-1})(y_k - y_{\mathrm{m},k}) - N_{n_{\mathrm{r}}}N_u(\mathbf{q}^{-1})\mathbf{q}^{-n_{\mathrm{r}}}[u_k - \hat{N}_{\mathrm{c}}(\mathbf{q}^{-1})y_k - \hat{D}_{\mathrm{c}}(\mathbf{q}^{-1})u_k - \hat{R}_{\mathrm{c}}(\mathbf{q}^{-1})r_k] \end{aligned} \tag{4.61}$$

Proof. Multiplying both sides of (4.55) by x_k, and using (4.8), (4.9), and (4.54) yields

$$D_{\mathrm{m}}(\mathbf{q}^{-1})N_{\mathrm{s}}(\mathbf{q}^{-1})F(\mathbf{q}^{-1})x_k = u_k - N_{\mathrm{c}}^*(\mathbf{q}^{-1})y_k - D_{\mathrm{c}}^*(\mathbf{q}^{-1})u_k. \tag{4.62}$$

Then, multiplying both sides of (4.62) by $N_{n_\mathrm{r}} N_u(\mathbf{q}^{-1})\mathbf{q}^{-n_\mathrm{r}}$ and using (4.9) yields

$$D_\mathrm{m}(\mathbf{q}^{-1})F(\mathbf{q}^{-1})y_k = N_{n_\mathrm{r}} N_u(\mathbf{q}^{-1})\mathbf{q}^{-n_\mathrm{r}}[u_k - N_\mathrm{c}^*(\mathbf{q}^{-1})y_k - D_\mathrm{c}^*(\mathbf{q}^{-1})u_k]. \tag{4.63}$$

Subtracting $F(\mathbf{q}^{-1})N_\mathrm{m}(\mathbf{q}^{-1})r_k$ from both sides of (4.63) and using (4.4) yields

$$D_\mathrm{m}(\mathbf{q}^{-1})F(\mathbf{q}^{-1})(y_k - y_{\mathrm{m},k}) = N_{n_\mathrm{r}} N_u(\mathbf{q}^{-1})\mathbf{q}^{-n_\mathrm{r}}[u_k - N_\mathrm{c}^*(\mathbf{q}^{-1})y_k - D_\mathrm{c}^*(\mathbf{q}^{-1})u_k] - F(\mathbf{q}^{-1})N_\mathrm{m}(\mathbf{q}^{-1})r_k. \tag{4.64}$$

Then, combining (4.57) with (4.64) yields

$$D_\mathrm{m}(\mathbf{q}^{-1})F(\mathbf{q}^{-1})(y_k - y_{\mathrm{m},k}) - N_{n_\mathrm{r}} N_u(\mathbf{q}^{-1})\mathbf{q}^{-n_\mathrm{r}}[u_k - N_\mathrm{c}^*(\mathbf{q}^{-1})y_k - D_\mathrm{c}^*(\mathbf{q}^{-1})u_k - R_\mathrm{c}^*(\mathbf{q}^{-1})F(\mathbf{q}^{-1})r_k] = 0. \tag{4.65}$$

Substituting (4.58)-(4.60) into (4.65) yields (4.61). □

Note that all the terms on the right-hand side of (4.61) are known, and thus the sum of terms on the left-hand side is known despite the fact that $\tilde{N}_\mathrm{c}(\mathbf{q}^{-1})$, $\tilde{D}_\mathrm{c}(\mathbf{q}^{-1})$, and $\tilde{R}_\mathrm{c}(\mathbf{q}^{-1})$ are individually unknown. Furthermore, if (4.58)-(4.60) are all zero, then both sides of (4.61) are zero. We thus define the performance variable

$$\begin{aligned} z_k \triangleq\ & D_\mathrm{m}(\mathbf{q}^{-1})F(\mathbf{q}^{-1})(y_k - y_{\mathrm{m},k}) - N_{n_\mathrm{r}} N_u(\mathbf{q}^{-1})\mathbf{q}^{-n_\mathrm{r}}[u_k - \hat{N}_\mathrm{c}(\mathbf{q}^{-1})y_k \\ & - \hat{D}_\mathrm{c}(\mathbf{q}^{-1})u_k - \hat{R}_\mathrm{c}(\mathbf{q}^{-1})F(\mathbf{q}^{-1})r_k] \qquad (4.66) \\ =\ & N_{n_\mathrm{r}} N_u(\mathbf{q}^{-1})\mathbf{q}^{-n_\mathrm{r}}[\tilde{N}_\mathrm{c}(\mathbf{q}^{-1})y_k + \tilde{D}_\mathrm{c}(\mathbf{q}^{-1})u_k + \tilde{R}_\mathrm{c}(\mathbf{q}^{-1})F(\mathbf{q}^{-1})r_k]. \qquad (4.67) \end{aligned}$$

Note that, if $\tilde{N}_\mathrm{c}(\mathbf{q}^{-1})$, $\tilde{D}_\mathrm{c}(\mathbf{q}^{-1})$, and $\tilde{R}_\mathrm{c}(\mathbf{q}^{-1})$ are all zero, then z_k is zero. We thus seek estimates $\hat{N}_\mathrm{c}(\mathbf{q}^{-1})$, $\hat{D}_\mathrm{c}(\mathbf{q}^{-1})$, and $\hat{R}_\mathrm{c}(\mathbf{q}^{-1})$ of $N_\mathrm{c}^*(\mathbf{q}^{-1})$, $D_\mathrm{c}^*(\mathbf{q}^{-1})$, and $R_\mathrm{c}^*(\mathbf{q}^{-1})$, respectively, that minimize the magnitude of z_k.

4.3.2 RC-MRAC Algorithm

Proposition 4.3.3. *Define*

$$\theta \triangleq \begin{bmatrix} N_{\mathrm{c},1}^* & \cdots & N_{\mathrm{c},n}^* & D_{\mathrm{c},1}^* & \cdots & D_{\mathrm{c},n}^* & R_{\mathrm{c},0}^* & \cdots & R_{\mathrm{c},n_\mathrm{s}}^* \end{bmatrix}^\mathrm{T}, \tag{4.68}$$

Then,

$$z_{\mathrm{f},k} - u_{\mathrm{f},k} + \Phi_{\mathrm{f},k}\theta = 0, \tag{4.69}$$

where

$$r_{\mathrm{f},k} \triangleq F(\mathbf{q}^{-1})r_k \tag{4.70}$$

$$\Phi_k \triangleq \begin{bmatrix} y_{k-1} & \cdots & y_{k-n} & u_{k-1} & \cdots & u_{k-n} & r_{\mathrm{f},k} & \cdots & r_{\mathrm{f},k-n_{\mathrm{s}}} \end{bmatrix}, \tag{4.71}$$

$$\Phi_{\mathrm{f},k} \triangleq N_{n_{\mathrm{r}}} N_u(\mathbf{q}^{-1})\mathbf{q}^{-n_{\mathrm{r}}}\Phi_k, \tag{4.72}$$

$$u_{\mathrm{f},k} \triangleq N_{n_{\mathrm{r}}} N_u(\mathbf{q}^{-1})\mathbf{q}^{-n_{\mathrm{r}}}u_k. \tag{4.73}$$

$$z_{\mathrm{f},k} \triangleq D_{\mathrm{m}}(\mathbf{q}^{-1})F(\mathbf{q}^{-1})(y_k - y_{\mathrm{m},k}). \tag{4.74}$$

Since $N_{\mathrm{c}}^*(\mathbf{q}^{-1})$, $D_{\mathrm{c}}^*(\mathbf{q}^{-1})$, and $R_{\mathrm{c}}^*(\mathbf{q}^{-1})$ are unknown, the goal is to solve the regression (4.69) at each step k to obtain the estimate $\hat{\theta}_k$. The estimation error is thus given by

$$\hat{z}_k(\hat{\theta}_k) \triangleq z_{\mathrm{f},k} - u_{\mathrm{f},k} + \Phi_{\mathrm{f},k}\hat{\theta}_k. \tag{4.75}$$

For regression at each step, RLS is used to minimize the cost function

$$J_k(\hat{\theta}_k) \triangleq \sum_{i=1}^{k} \lambda^{k-i}[\hat{z}_i(\hat{\theta}_i)^{\mathrm{T}}\hat{z}_i(\hat{\theta}_i)] + \lambda^k(\hat{\theta}_k - \hat{\theta}_0)^{\mathrm{T}}R_\theta(\hat{\theta}_k - \hat{\theta}_0), \tag{4.76}$$

where $\lambda \in (0, 1]$ is the forgetting factor. Using the computed RLS solution and (4.47), the control input at step $k + 1$ is given by

$$u_{k+1} = \Phi_{k+1}\hat{\theta}_{k+1}. \tag{4.77}$$

Note that $N_{n_{\mathrm{r}}}$, $N_u(\mathbf{q}^{-1})$, n_{r}, and n are assumed to be known a priori.

4.4 Connection Between RC-MRAC and APPC

In the following section we show that in the special case where $N_{\mathrm{m}}(\mathbf{q}^{-1}) = N(\mathbf{q}^{-1})$, and $H(\mathbf{q}^{-1}) = N_{\mathrm{s}}(\mathbf{q}^{-1})F(\mathbf{q}^{-1})$, APPC and RC-MRAC are equivalent.

Proposition 4.4.1. *Let* $H(\mathbf{q}^{-1}) = N_{\mathrm{s}}(\mathbf{q}^{-1})F(\mathbf{q}^{-1})$*, and* $N_{\mathrm{m}}(\mathbf{q}^{-1}) = N(\mathbf{q}^{-1})$ *such that* $R_{\mathrm{c}}^*(\mathbf{q}^{-1}) = N_{\mathrm{s}}(\mathbf{q}^{-1})$*. Then,* (4.65) *is equivalent to* (4.32)*.*

Proof. Substituting $R_{\mathrm{c}}^*(\mathbf{q}^{-1}) = N_{\mathrm{s}}(\mathbf{q}^{-1})$ into (4.65) yields

$$D_{\mathrm{m}}(\mathbf{q}^{-1})F(\mathbf{q}^{-1})(y_k - y_{\mathrm{m},k}) - N_{n_{\mathrm{r}}}N_u(\mathbf{q}^{-1})\mathbf{q}^{-n_{\mathrm{r}}}[u_k - N_{\mathrm{c}}^*(\mathbf{q}^{-1})y_k - D_{\mathrm{c}}^*(\mathbf{q}^{-1})u_k - N_{\mathrm{s}}(\mathbf{q}^{-1})F(\mathbf{q}^{-1})r_k] = 0. \tag{4.78}$$

Using (4.4) and (4.57) in (4.78),

$$\begin{aligned}
&D_{\mathrm{m}}(\mathbf{q}^{-1})F(\mathbf{q}^{-1})y_k - F(\mathbf{q}^{-1})N_{\mathrm{m}}(\mathbf{q}^{-1})r_k \\
&\quad - N_{n_{\mathrm{r}}}N_u(\mathbf{q}^{-1})\mathbf{q}^{-n_{\mathrm{r}}}[u_k - N_{\mathrm{c}}^*(\mathbf{q}^{-1})y_k - D_{\mathrm{c}}^*(\mathbf{q}^{-1})u_k - N_{\mathrm{s}}(\mathbf{q}^{-1})F(\mathbf{q}^{-1})r_k] \\
&= F(\mathbf{q}^{-1})D_{\mathrm{m}}(\mathbf{q}^{-1})y_k - F(\mathbf{q}^{-1})N_{\mathrm{m}}(\mathbf{q}^{-1})r_k - N_{n_{\mathrm{r}}}N_u(\mathbf{q}^{-1})\mathbf{q}^{-n_{\mathrm{r}}}[u_k - N_{\mathrm{c}}^*(\mathbf{q}^{-1})y_k - D_{\mathrm{c}}^*(\mathbf{q}^{-1})u_k] \\
&\quad + N_{n_{\mathrm{r}}}N_u(\mathbf{q}^{-1})N_{\mathrm{s}}(\mathbf{q}^{-1})\mathbf{q}^{-n_{\mathrm{r}}}F(\mathbf{q}^{-1})r_k = 0. \qquad (4.79)
\end{aligned}$$

Using (4.57) in (4.79),

$$D_{\mathrm{m}}(\mathbf{q}^{-1})F(\mathbf{q}^{-1})y_k - N_{n_{\mathrm{r}}}N_u(\mathbf{q}^{-1})\mathbf{q}^{-n_{\mathrm{r}}}[u_k - N_{\mathrm{c}}^*(\mathbf{q}^{-1})y_k - D_{\mathrm{c}}^*(\mathbf{q}^{-1})u_k] = 0. \qquad (4.80)$$

Then, substituting (4.9) into (4.80) and dividing by $N_{n_{\mathrm{r}}}N_u(\mathbf{q}^{-1})\mathbf{q}^{-n_{\mathrm{r}}}$ yields

$$\begin{aligned}
&D_{\mathrm{m}}(\mathbf{q}^{-1})F(\mathbf{q}^{-1})N(\mathbf{q}^{-1})x_k - N_{n_{\mathrm{r}}}N_u(\mathbf{q}^{-1})\mathbf{q}^{-n_{\mathrm{r}}}[u_k - N_{\mathrm{c}}^*(\mathbf{q}^{-1})y_k - D_{\mathrm{c}}^*(\mathbf{q}^{-1})u_k] \\
&\quad = D_{\mathrm{m}}(\mathbf{q}^{-1})F(\mathbf{q}^{-1})N_{\mathrm{s}}(\mathbf{q}^{-1})x_k - [u_k - N_{\mathrm{c}}^*(\mathbf{q}^{-1})y_k - D_{\mathrm{c}}^*(\mathbf{q}^{-1})u_k] = 0. \qquad (4.81)
\end{aligned}$$

Substituting $N_{\mathrm{s}}(\mathbf{q}^{-1})F(\mathbf{q}^{-1}) = H(\mathbf{q}^{-1})$, and using the Bezout identity (4.31) yields the result

$$D_{\mathrm{m}}(\mathbf{q}^{-1})H(\mathbf{q}^{-1})[B^*(\mathbf{q}^{-1})y_k + C^*(\mathbf{q}^{-1})u_k] = u_k - N_{\mathrm{c}}^*(\mathbf{q}^{-1})y_k - D_{\mathrm{c}}^*(\mathbf{q}^{-1})u_k. \qquad (4.82)$$

□

4.5 Example 1: Minimum-Phase Plant

Consider the plant

$$\frac{N(\mathbf{q}^{-1})}{D(\mathbf{q}^{-1})} = \frac{\mathbf{q}^{-1} - 0.5\mathbf{q}^{-2}}{(1 - \rho e^{J\nu}\mathbf{q}^{-1})(1 - \rho e^{-J\nu}\mathbf{q}^{-1})}, \qquad (4.83)$$

and the desired model

$$\frac{N_{\mathrm{m}}(\mathbf{q}^{-1})}{D_{\mathrm{m}}(\mathbf{q}^{-1})} = \frac{\mathbf{q}^{-1} - 0.5\mathbf{q}^{-2}}{(1 - 0.5e^{J\frac{\pi}{2}}\mathbf{q}^{-1})(1 - 0.5e^{-J\frac{\pi}{2}}\mathbf{q}^{-1})}. \qquad (4.84)$$

The following subsections demonstrate the model-following performance of APPC and RC-MRAC for various values of ρ and ν for step and harmonic commands. It is assumed that $N(\mathbf{q}^{-1})$ is known in order to compare the two algorithms. Each simulation is run for 200 steps, where the

performance metric

$$\|e\| \triangleq \sqrt{\sum_{i=101}^{200} e_i^2} \tag{4.85}$$

is used to compare the algorithms.

4.5.1 Example 1a: APPC for Reference Model Following

For the APPC algorithm we choose

$$H(\mathbf{q}^{-1}) = N_s(\mathbf{q}^{-1})F(\mathbf{q}^{-1}) = (1 - 0.5\mathbf{q}^{-1})(1 + 0.5\mathbf{q}^{-1}) = 1 - 0.25\mathbf{q}^{-2}, \tag{4.86}$$

and initialize $\hat{\theta}_{1,0} = 0_{4\times1}$ and $\hat{\theta}_{2,0} = 0_{4\times1}$ with $R_\theta = 10^{-5}I_8$ and $\lambda = 1$.

Given a unit step command for r_k, the model-following error versus the pole locations of the plant is shown in Figure 4.2a for various values of ρ and ν. Note that the model-following performance degrades as the plant poles move closer to the plant zero due to the system nearing a decrease in order. The response of the system for $\rho = 0.5$ and $\nu = \frac{\pi}{4}$ is given in Figure 4.2b.

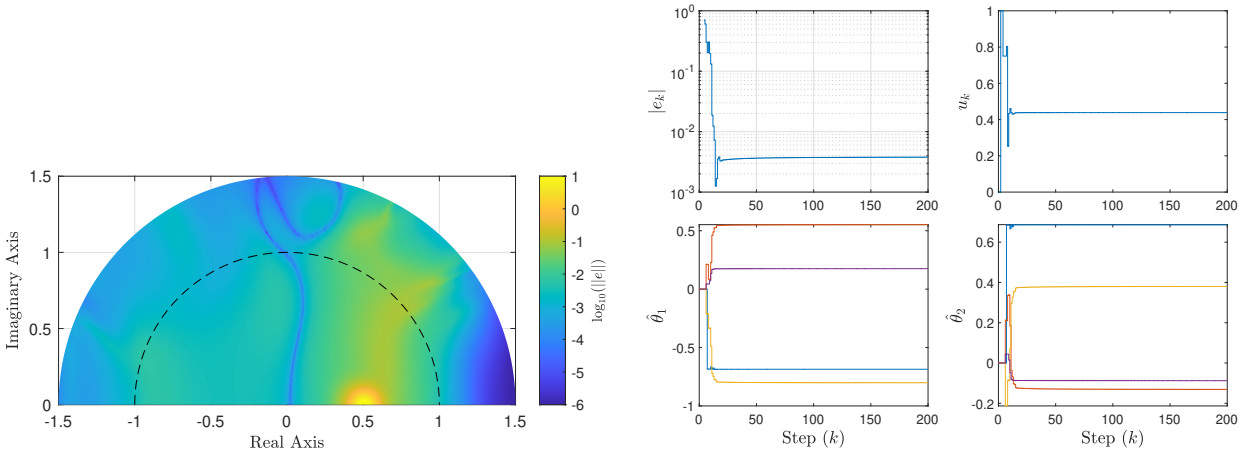

(a) (b)

Figure 4.2: APPC for the minimum-phase plant (4.83) with a step command. a) Log of the model-following error versus the pole locations of the plant. b) Response of the system for $\rho = 0.5$ and $\nu = \frac{\pi}{4}$. Viewing clockwise from the top left: model-following error e_k, control input u_k, Bezout coefficient estimates $\hat{\theta}_2$, and controller coefficient estimates $\hat{\theta}_1$.

Given the two-harmonic command $r_k = \cos(k) + \cos(\frac{1}{8}k)$, the model-following error versus the pole locations of the plant is shown in Figure 4.3a for various values of ρ and ν. Note that the model-following performance degrades as the plant poles move closer to the plant zero. The overall

model-following error is improved compared to the step command. The response of the system for $\rho = 0.5$ and $\nu = \frac{\pi}{4}$ is given in Figure 4.3b.

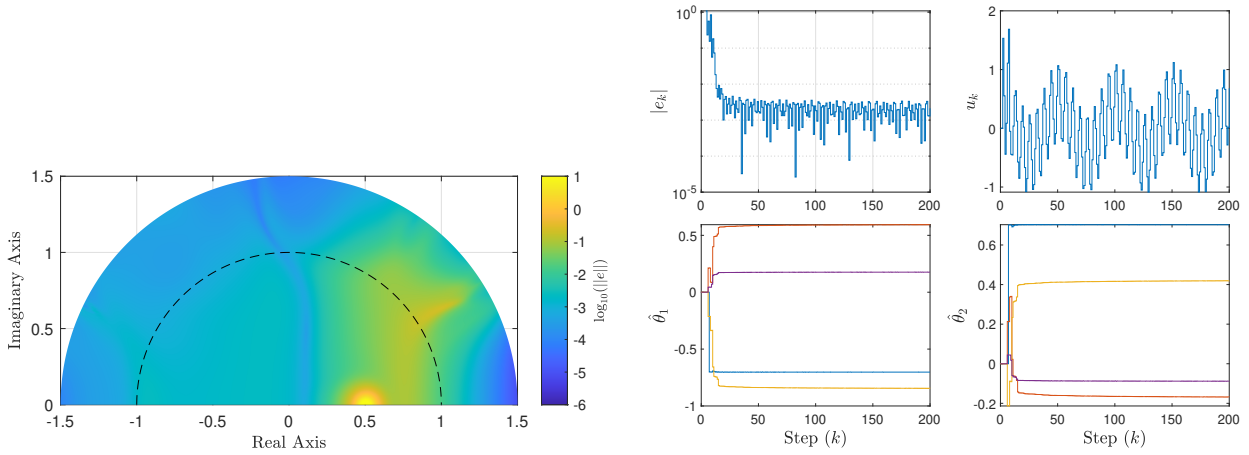

(a) (b)

Figure 4.3: APPC for the minimum-phase plant (4.83) with a two-harmonic command. a) Log of the model-following error versus the pole locations of the plant. b) Response of the system for $\rho = 0.5$ and $\nu = \frac{\pi}{4}$. Viewing clockwise from the top left: model-following error e_k, control input u_k, Bezout coefficient estimates $\hat{\theta}_2$, and controller coefficient estimates $\hat{\theta}_1$.

Given the four-harmonic command $r_k = \cos(k) + \cos(\frac{1}{2}k) + \cos(\frac{1}{4}k) + \cos(\frac{1}{8}k)$, the model-following error versus the pole locations of the plant is shown in Figure 4.4a for various values of ρ and ν. Note that the model-following performance degrades as the plant poles move closer to the plant zero. Due to the increased persistency of the command, the model-following error is improved over both the step command and the two-harmonic command. The response of the system for $\rho = 0.5$ and $\nu = \frac{\pi}{4}$ is given in Figure 4.4b.

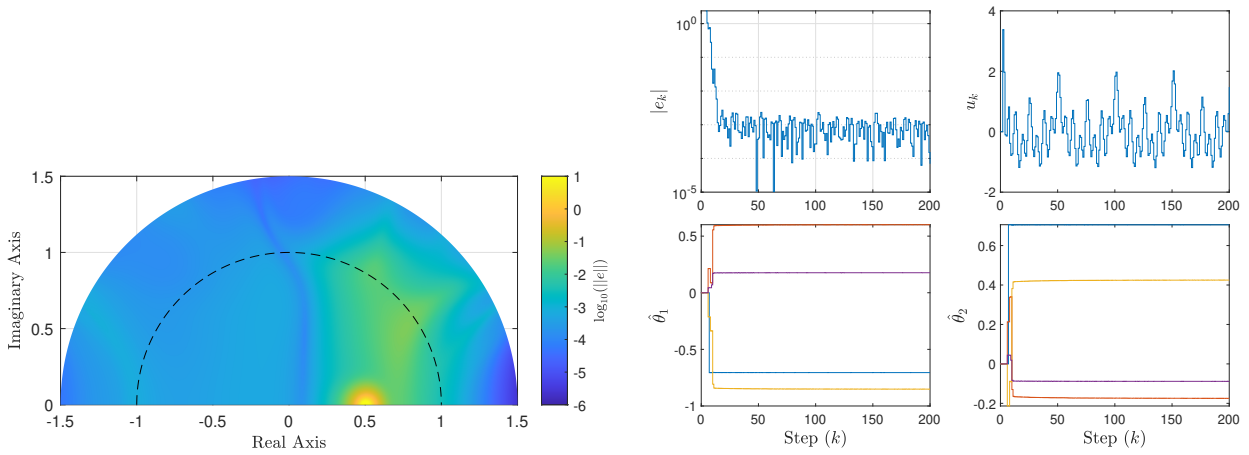

(a) (b)

Figure 4.4: APPC for the minimum-phase plant (4.83) with a four-harmonic command. a) Log of the model-following error versus the pole locations of the plant. b) Response of the system for $\rho = 0.5$ and $\nu = \frac{\pi}{4}$. Viewing clockwise from the top left: model-following error e_k, control input u_k, Bezout coefficient estimates $\hat{\theta}_2$, and controller coefficient estimates $\hat{\theta}_1$.

4.5.2 Example 1b: RC-MRAC for Reference Model Following

For RC-MRAC, we choose

$$F(\mathbf{q}^{-1}) = (1 + 0.5\mathbf{q}^{-1}), \tag{4.87}$$

and initialize $\hat{\theta}_0 = 0_{6\times 1}$, with $R_\theta = 10^{-5} I_6$ and $\lambda = 1$.

Given a unit step command for r_k, the model-following error versus the pole locations of the plant is shown in Figure 4.5a for various values of ρ and ν. Note that the model-following performance degrades as the plant poles move closer to the plant zero. The response of the system for $\rho = 0.5$ and $\nu = \frac{\pi}{4}$ is given in Figure 4.5b.

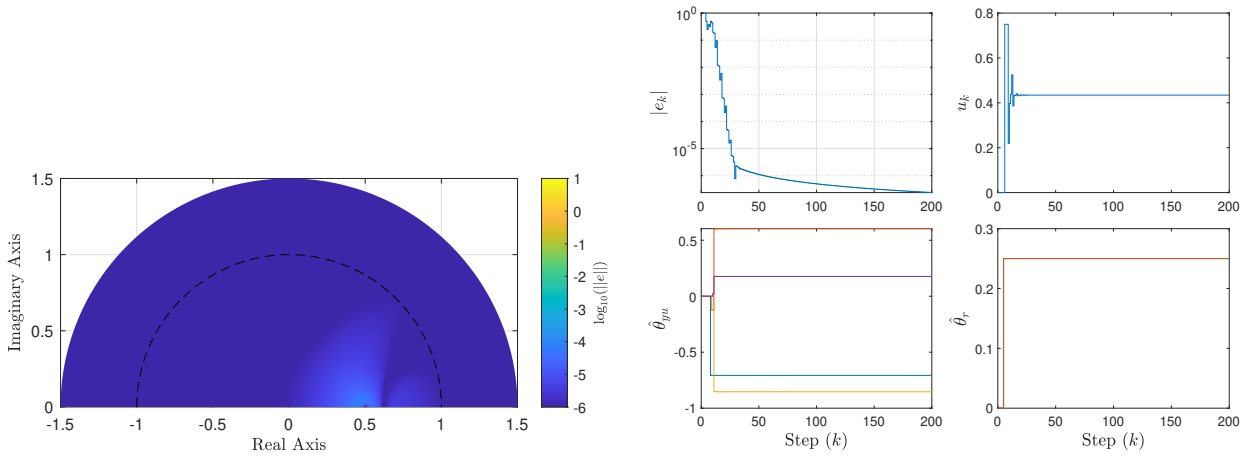

(a) (b)

Figure 4.5: RC-MRAC for the minimum-phase plant (4.83) with a step command. a) Log of the model-following error versus the pole locations of the plant. b) Response of the system for $\rho = 0.5$ and $\nu = \frac{\pi}{4}$. Viewing clockwise from the top left: model-following error e_k, control input u_k, controller coefficients $\hat{\theta}$ associated with r_k, and controller coefficients $\hat{\theta}$ associated with y_k and u_k.

Given the two-harmonic command $r_k = \cos(k) + \cos(\frac{1}{8}k)$, the model-following error versus the pole locations of the plant is shown in Figure 4.6a for various values of ρ and ν. Note that the model-following performance degrades as the plant poles move closer to the plant zero. The overall model-following error is similar to the step command. The response of the system for $\rho = 0.5$ and $\nu = \frac{\pi}{4}$ is given in Figure 4.6b.

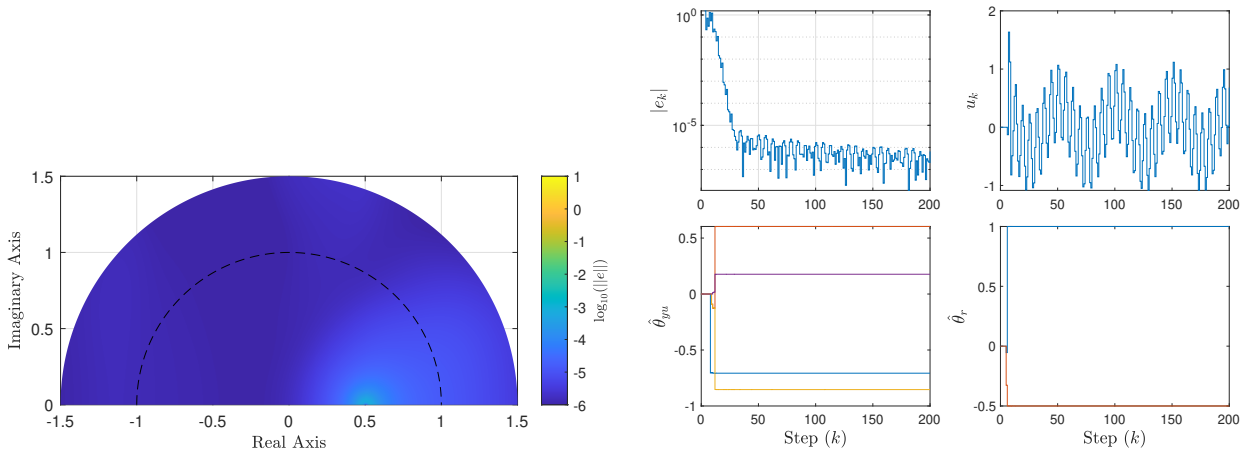

(a) (b)

Figure 4.6: RC-MRAC for the minimum-phase plant (4.83) with a two-harmonic command. a) Log of the model-following error versus the pole locations of the plant. b) Response of the system for $\rho = 0.5$ and $\nu = \frac{\pi}{4}$. Viewing clockwise from the top left: model-following error e_k, control input u_k, controller coefficients $\hat{\theta}$ associated with r_k, and controller coefficients $\hat{\theta}$ associated with y_k and u_k.

Given the four-harmonic command $r_k = \cos(k) + \cos(\frac{1}{2}k) + \cos(\frac{1}{4}k) + \cos(\frac{1}{8}k)$, the model-following error versus the pole locations of the plant is shown in Figure 4.7a for various values of ρ and ν. Note that the model-following performance degrades as the plant poles move closer to the plant zero. The response of the system for $\rho = 0.5$ and $\nu = \frac{\pi}{4}$ is given in Figure 4.7b.

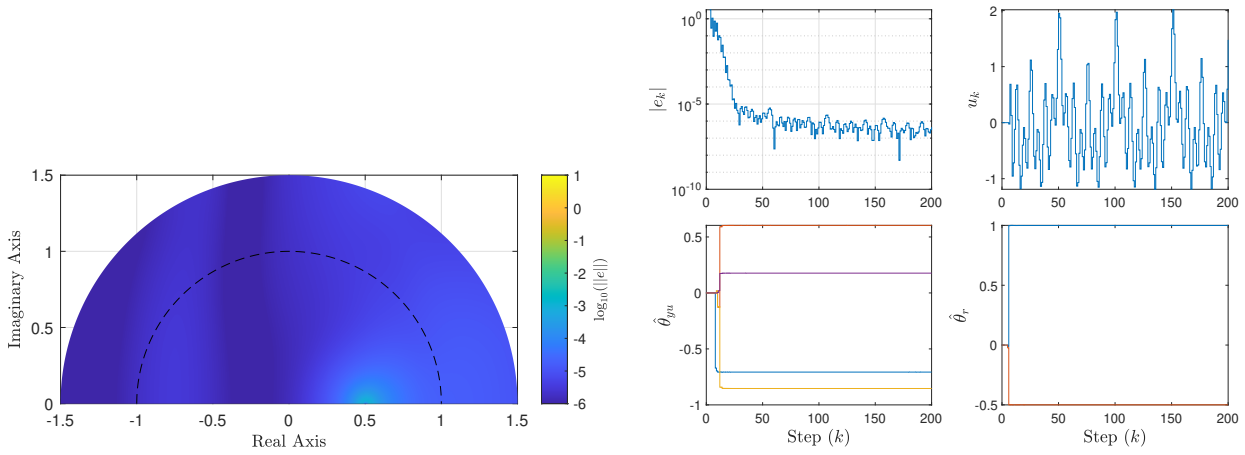

(a) (b)

Figure 4.7: RC-MRAC for the minimum-phase plant (4.83) with a four-harmonic command. a) Log of the model-following error versus the pole locations of the plant. b) Response of the system for $\rho = 0.5$ and $\nu = \frac{\pi}{4}$. Viewing clockwise from the top left: model-following error e_k, control input u_k, controller coefficients $\hat{\theta}$ associated with r_k, and controller coefficients $\hat{\theta}$ associated with y_k and u_k.

4.6 Example 2: Nonminimum-Phase Plant

Consider the plant

$$\frac{N(\mathbf{q}^{-1})}{D(\mathbf{q}^{-1})} = \frac{\mathbf{q}^{-1} - 1.5\mathbf{q}^{-2}}{(1 - \rho e^{J\nu}\mathbf{q}^{-1})(1 - \rho e^{-J\nu}\mathbf{q}^{-1})}, \tag{4.88}$$

and the desired model

$$\frac{N_{\mathrm{m}}(\mathbf{q}^{-1})}{D_{\mathrm{m}}(\mathbf{q}^{-1})} = \frac{\mathbf{q}^{-1} - 1.5\mathbf{q}^{-2}}{(1 - 0.5e^{J\frac{\pi}{2}}\mathbf{q}^{-1})(1 - 0.5e^{-J\frac{\pi}{2}}\mathbf{q}^{-1})}. \tag{4.89}$$

The following subsections demonstrate the model-following performance of RC-MRAC and APPC for various values of ρ and ν for step and harmonic commands. It is assumed that $N(\mathbf{q}^{-1})$ is known in order to compare the two algorithms. The same performance metric (4.85) as in Example 1 is used.

4.6.1 Example 2a: APPC for Reference Model Following

For the APPC algorithm we choose

$$H(\mathbf{q}^{-1}) = 1 - 0.25\mathbf{q}^{-2}, \tag{4.90}$$

and initialize $\hat{\theta}_{1,0} = 0_{4\times1}$ and $\hat{\theta}_{2,0} = 0_{4\times1}$ with $R_\theta = 10^{-5} I_8$ and $\lambda = 1$.

Given a unit step command for r_k, the model-following error versus the pole locations of the plant is shown in Figure 4.8a for various values of ρ and ν. Note that the model-following performance degrades as the plant poles move closer to the plant zero. The response of the system for $\rho = 0.5$ and $\nu = \frac{\pi}{4}$ is given in Figure 4.8b.

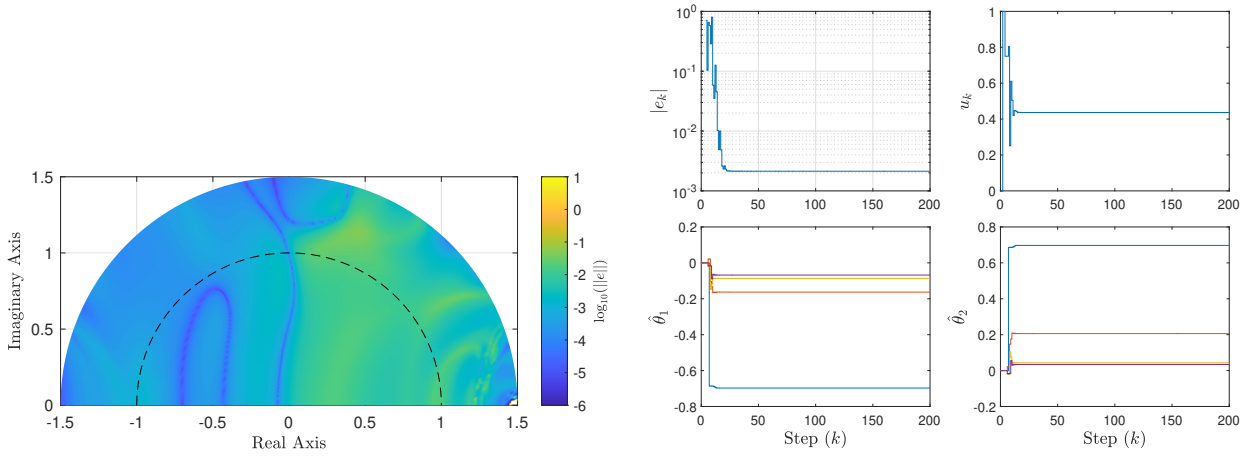

(a) (b)

Figure 4.8: APPC for the NMP plant (4.88) with a step command. a) Log of the model-following error versus the pole locations of the plant. Empty squares represent regions where the system became unstable. b) Response of the system for $\rho = 0.5$ and $\nu = \frac{\pi}{4}$. Viewing clockwise from the top left: model-following error e_k, control input u_k, Bezout coefficient estimates $\hat{\theta}_2$, and controller coefficient estimates $\hat{\theta}_1$.

Given the two-harmonic command $r_k = \cos(k) + \cos(\frac{1}{8}k)$, the model-following error versus the pole locations of the plant is shown in Figure 4.9a for various values of ρ and ν. Note that the model-following performance degrades as the plant poles move closer to the plant zero. The overall model-following error is improved compared to the step command. The response of the system for $\rho = 0.5$ and $\nu = \frac{\pi}{4}$ is given in Figure 4.9b.

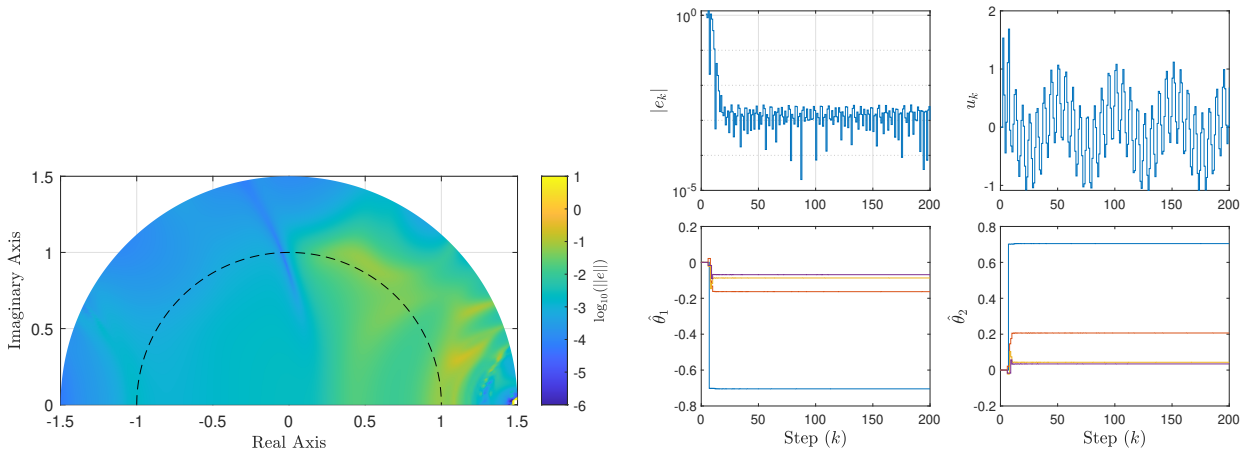

(a) (b)

Figure 4.9: APPC for the NMP plant (4.88) with a two-harmonic command. a) Log of the model-following error versus the pole locations of the plant. Empty squares represent regions where the system became unstable. b) Response of the system for $\rho = 0.5$ and $\nu = \frac{\pi}{4}$. Viewing clockwise from the top left: model-following error e_k, control input u_k, Bezout coefficient estimates $\hat{\theta}_2$, and controller coefficient estimates $\hat{\theta}_1$.

Given the four-harmonic command $r_k = \cos(k) + \cos(\frac{1}{2}k) + \cos(\frac{1}{4}k) + \cos(\frac{1}{8}k)$, the model-following error versus the pole locations of the plant is shown in Figure 4.10a for various values of ρ and ν. Note that the model-following performance degrades as the plant poles move closer to the plant zero. Due to the increased persistency of the command, the model-following error is improved over both the step command and the two-harmonic command. The response of the system for $\rho = 0.5$ and $\nu = \frac{\pi}{4}$ is given in Figure 4.10b.

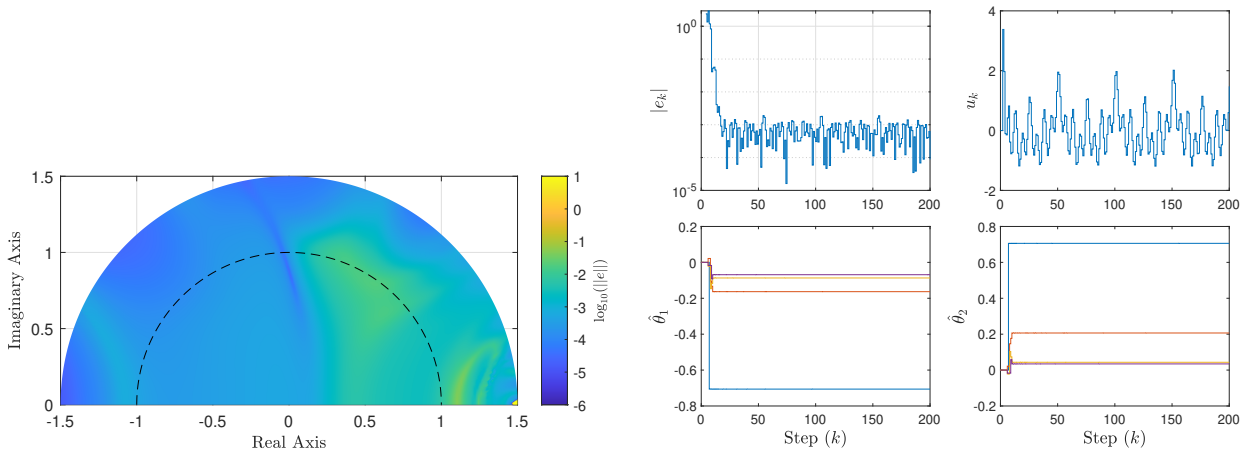

(a) (b)

Figure 4.10: APPC for the NMP plant (4.88) with a four-harmonic command. a) Log of the model-following error versus the pole locations of the plant. Empty squares represent regions where the system became unstable. b) Response of the system for $\rho = 0.5$ and $\nu = \frac{\pi}{4}$. Viewing clockwise from the top left: model-following error e_k, control input u_k, Bezout coefficient estimates $\hat{\theta}_2$, and controller coefficient estimates $\hat{\theta}_1$.

4.6.2 Example 2b: RC-MRAC for Reference Model Following

For RC-MRAC, we choose

$$F(\mathbf{q}^{-1}) = 1 - 0.25\mathbf{q}^{-2}, \tag{4.91}$$

and initialize $\hat{\theta}_0 = 0_{5\times 1}$, with $R_\theta = 10^{-5} I_5$ and $\lambda = 1$. Given a unit step command for r_k, the model-following error versus the pole locations of the plant is shown in Figure 4.11a for various values of ρ and ν. Note that the model-following performance degrades as the plant poles move closer to the plant zero and that the convergence is much slower than in the minimum-phase case. The response of the system for $\rho = 0.5$ and $\nu = \frac{\pi}{4}$ is given in Figure 4.11b.

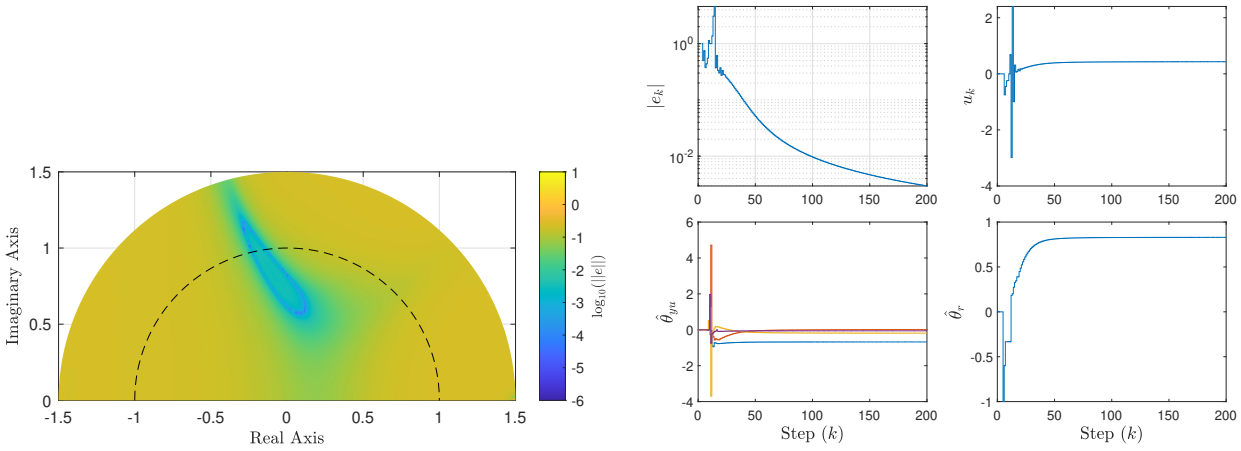

(a) (b)

Figure 4.11: RC-MRAC for the NMP plant (4.88) with step command. a) Log of the model-following error versus the pole locations of the plant. b) Response of the system for $\rho = 0.5$ and $\nu = \frac{\pi}{4}$. Viewing clockwise from the top left: model-following error e_k, control input u_k, controller coefficients $\hat{\theta}$ associated with r_k, and controller coefficients $\hat{\theta}$ associated with y_k and u_k.

Given the two-harmonic command $r_k = \cos(k) + \cos(\frac{1}{8}k)$, the model-following error versus the pole locations of the plant is shown in Figure 4.12a for various values of ρ and ν. Note that the model-following performance degrades as the plant poles move closer to the plant zero. The overall model-following error is improved compared to the step command, but the controller convergence is still slower than the minimum-phase case. The response of the system for $\rho = 0.5$ and $\nu = \frac{\pi}{4}$ is given in Figure 4.12b.

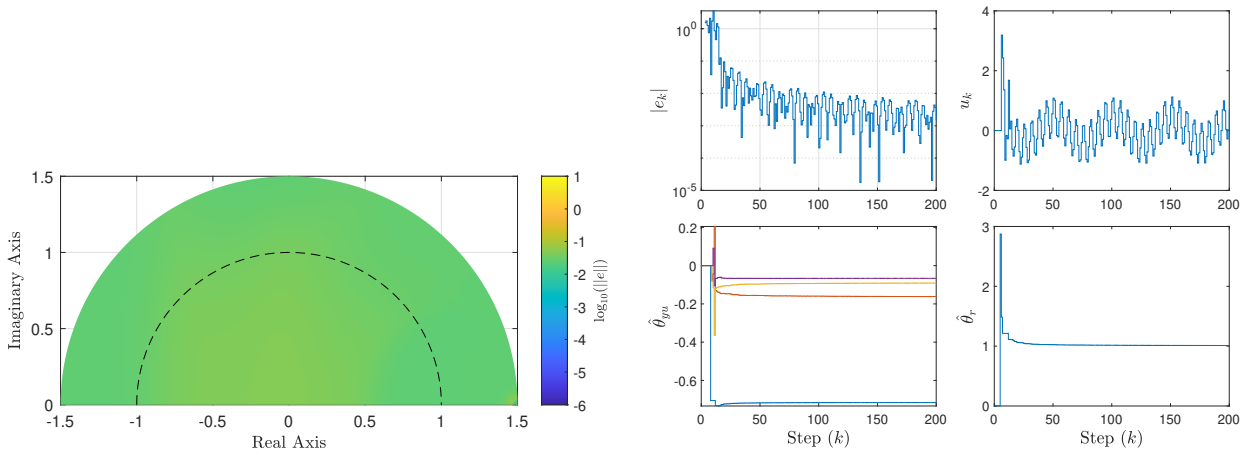

(a) (b)

Figure 4.12: RC-MRAC for the NMP plant (4.88) with a two-harmonic command. a) Log of the model-following error versus the pole locations of the plant. b) Response of the system for $\rho = 0.5$ and $\nu = \frac{\pi}{4}$. Viewing clockwise from the top left: model-following error e_k, control input u_k, controller coefficients $\hat{\theta}$ associated with r_k, and controller coefficients $\hat{\theta}$ associated with y_k and u_k.

Given the four-harmonic command $r_k = \cos(k) + \cos(\frac{1}{2}k) + \cos(\frac{1}{4}k) + \cos(\frac{1}{8}k)$, the model-following error versus the pole locations of the plant is shown in Figure 4.13a for various values of ρ and ν. Note that the model-following performance degrades as the plant poles move closer to the plant zero. Due to the increased persistency of the command, the model-following error is improved over both the step command and the two-harmonic command. The convergence of the controller is much slower than in the minimum-phase case. The response of the system for $\rho = 0.5$ and $\nu = \frac{\pi}{4}$ is given in Figure 4.13b.

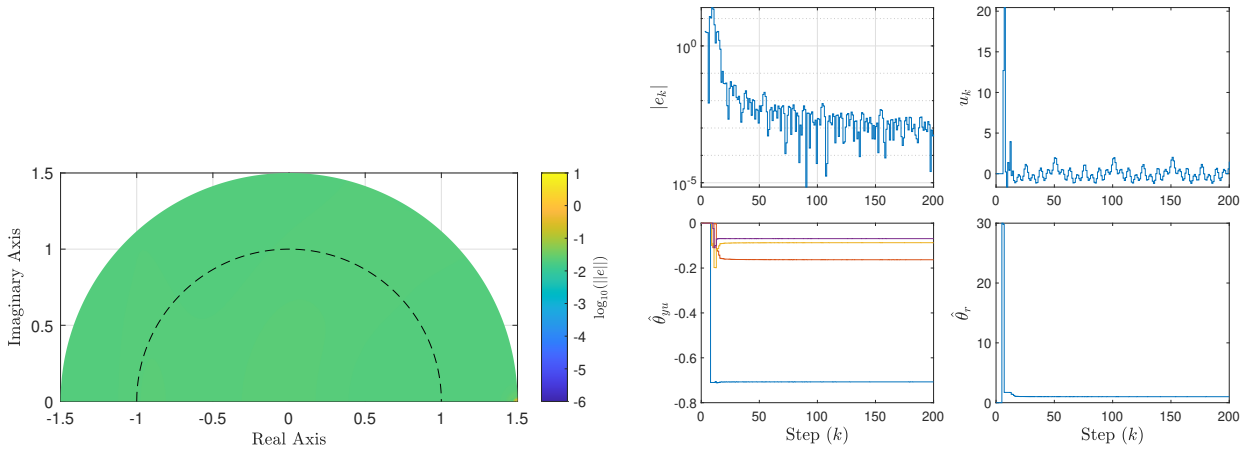

(a) (b)

Figure 4.13: RC-MRAC for the NMP plant (4.88) with a four-harmonic command. a) Log of the model-following error versus the pole locations of the plant. b) Response of the system for $\rho = 0.5$ and $\nu = \frac{\pi}{4}$. Viewing clockwise from the top left: model-following error e_k, control input u_k, controller coefficients $\hat{\theta}$ associated with r_k, and controller coefficients $\hat{\theta}$ associated with y_k and u_k.

4.7 Example 3: Unknown Harmonic Disturbance Rejection Using RC-MRAC

Consider the same system (4.83), and reference model (4.84), as in Example 1. We now place an unknown single harmonic disturbance at the frequency 0.35 radians per step at the input of the system. In this section we show that, unlike APPC, RC-MRAC can be used for disturbance rejection of unknown harmonic disturbances with a small modification. The disturbance rejection capability is tested for various values of ρ and ν for a step command on the reference model. It is assumed that $N(\mathbf{q}^{-1})$ is known. The same performance metric (4.85) as in Example 1 is used.

To accomplish harmonic disturbance rejection and model-following, we increase the order of the controller to $n = 4$, and set $n_s = 3$ to match the desired closed-loop model relative degree. The order must be incremented by 2 for each expected harmonic disturbance. The order can be larger than required at the cost of perfect model tracking. RLS is initialized with $\hat{\theta}_0 = 0_{12\times1}$, $R_\theta = 10^{-5}I_{12}$ and $\lambda = 1$. $F(\mathbf{q}^{-1})$ is chosen to be (4.87), the same as in Example 1b.

Given a unit step command for r_k, the model-following error versus the pole locations of the plant is shown in Figure 4.14a for various values of ρ and ν. Note that the model-following performance degrades as the plant poles move closer to the plant zero, but the algorithm is able to perform the model-following task while rejecting the disturbance for all tested poles. The response of the system for $\rho = 0.5$ and $\nu = \frac{\pi}{4}$ is given in Figure 4.14b.

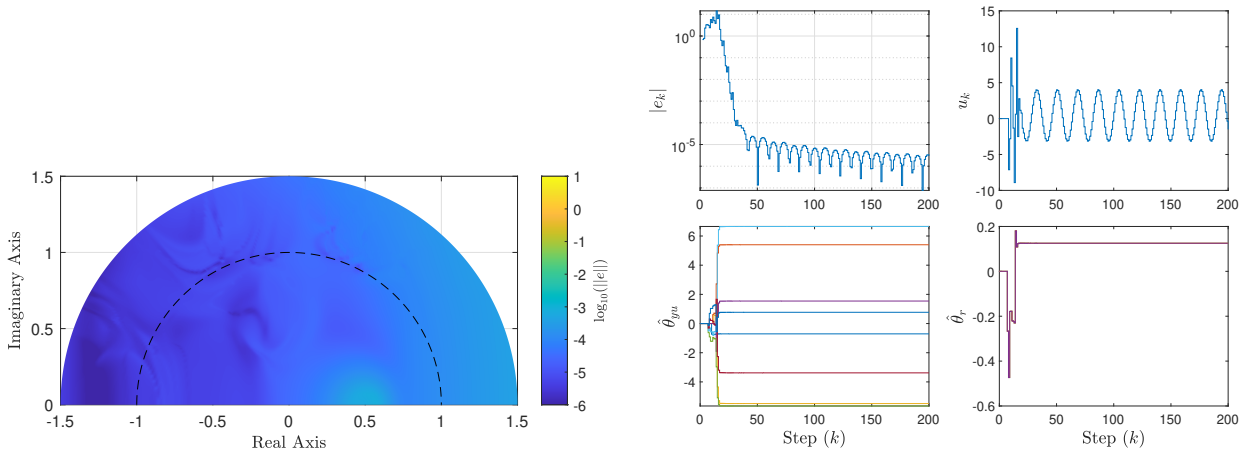

(a) (b)

Figure 4.14: RC-MRAC for harmonic disturbance rejection on the plant (4.83) with a step command. a) Log of the model-following error versus the pole locations of the plant. b) Response of the system for $\rho = 0.5$ and $\nu = \frac{\pi}{4}$. Viewing clockwise from the top left: model-following error e_k, control input u_k, controller coefficients $\hat{\theta}$ associated with r_k, and controller coefficients $\hat{\theta}$ associated with y_k and u_k.

4.8 Conclusions

In this chapter, RC-MRAC was developed and compared to Elliot's APPC. This controller places the closed-loop poles of the system to match the desired closed-loop poles given by a reference model provided that the leading numerator coefficient, relative degree, system order, and NMP zeros are known. RC-MRAC was shown numerically to be stable over a wide range of systems. Unlike APPC, the performance of RC-MRAC is not as sensitive to the persistency of the desired command. Additionally, it was shown that, with a slight modification, RC-MRAC can reject harmonic disturbances. For minimum-phase systems, RC-MRAC outperforms APPC without the need for persistency. For NMP systems, RC-MRAC performs better than APPC at lower persistency levels at the price of knowledge of the NMP zeros and slower convergence times.

CHAPTER 5

Variable-Rate Forgetting Using the *F*-Test

In this chapter we consider the RLS-VRF equations (2.12)-(2.14). The variable-rate forgetting factor λ_k is used to enable RLS to track time-varying parameters by discounting past data. This factor can take many forms and still maintain the consistency properties of RLS as long as they follow the conditions given in [45]. For example, the formulation in [50] uses a ratio of RMS performance errors to the noise standard deviation.

Inspired by the statistical analysis of the ratio of sample variances, we develop a new variable-rate forgetting factor using the F-test. The F-test is typically used to compare whether two sample variances are statistically equal in analysis of variance tests [74, 75]. The ratio of sample variances taken from normally distributed random variables follows an F-distribution, and if the ratio exceeds or is below what is expected for a given significance level, then the two variances are determined to not be equal. The main idea is to use the F-test to determine the level of forgetting to use in RLS based on the ratio of the variance of two sliding windows of prediction errors of differing length. When the variance of recent predictions increases relative to earlier predictions, we expect that the parameters have changed, and forgetting is warranted relative to the increase in variance. The goal is to prevent forgetting when sufficiently exciting data is not available while also enabling forgetting during parameter changes to allow RLS to quickly learn new parameters. The approach is applied to a parameter identification task and is compared to a constant-rate forgetting factor and the RMS performance error and noise standard-deviation-based forgetting factor given in [50].

5.1 Variable Rate Forgetting Using the *F*-Test

When using RLS, we would like to use forgetting to place a higher weight on more recent data while also suspending forgetting when new data is not available. To accomplish this, let β_k be given by

$$\beta_k \triangleq 1 + \eta g(e_0(\theta_0), \ldots, e_k(\theta_k))\mathbf{1}[g(e_0(\theta_0), \ldots, e_k(\theta_k))] \tag{5.1}$$

where $\mathbf{1}\colon \mathbb{R} \rightarrow \{0, 1\}$ is the unit step function, $\eta > 0$, and $g(e_0(\theta_0), \ldots, e_k(\theta_k))$ is a function of past RLS prediction errors. From (5.1) it follows that, if $g(e_0(\theta_0), \ldots, e_k(\theta_k)) \leq 0$, then forgetting is suspended, otherwise the level of forgetting is proportional to the magnitude of $g(e_0(\theta_0), \ldots, e_k(\theta_k))$ scaled by η. The objective is to determine an appropriate $g(e_0(\theta_0), \ldots, e_k(\theta_k))$. We expect that, if the true θ has changed relative to the current estimate of θ, then the variance of the prediction errors will increase [76]. When this occurs, we wish to forget older data in order to adjust the parameter estimate quickly. Therefore, we wish to compare the variance of a long and short window of past RLS prediction errors to determine whether the variance has increased, and, if so, enable forgetting. For $p = 1$, the F-test will facilitate this comparison.

Given two sample variances $\sigma^2_{\tau_\mathrm{n}}$ from $\tau_\mathrm{n} + 1$ samples and $\sigma^2_{\tau_\mathrm{d}}$ from $\tau_\mathrm{d} + 1$ samples, where $\tau_\mathrm{d} > \tau_\mathrm{n} \geq p$, and $\sigma^2_{\tau_\mathrm{n}} \geq \sigma^2_{\tau_\mathrm{d}}$, the variance $\sigma^2_{\tau_\mathrm{n}}$ is greater than $\sigma^2_{\tau_\mathrm{d}}$ with significance level α if

$$F^{-1}_{\tau_\mathrm{n},\tau_\mathrm{d}}(1 - \alpha) < \frac{\sigma^2_{\tau_\mathrm{n}}}{\sigma^2_{\tau_\mathrm{d}}}, \tag{5.2}$$

where $F^{-1}_{\tau_\mathrm{n},\tau_\mathrm{d}}(x)$ is the inverse cumulative distribution function of the F-distribution with degrees of freedom τ_n and τ_d [75]. The larger the variance ratio is from $F^{-1}_{\tau_\mathrm{n},\tau_\mathrm{d}}(1-\alpha)$, the stronger the evidence that $\sigma^2_{\tau_\mathrm{n}}$ is greater than $\sigma^2_{\tau_\mathrm{d}}$. The F-test can also be written as

$$\sqrt{F^{-1}_{\tau_\mathrm{n},\tau_\mathrm{d}}(1 - \alpha)} < \sqrt{\frac{\sigma^2_{\tau_\mathrm{n}}}{\sigma^2_{\tau_\mathrm{d}}}}. \tag{5.3}$$

This leads to a $g(e_0(\theta_0), \ldots, e_k(\theta_k))$ for the case $p = 1$. Given sample variances of the past RLS prediction errors $\sigma^2_{\tau_\mathrm{n}}(e_{k-\tau_n}(\theta_{k-\tau_n}), \ldots, e_k(\theta_k))$ and $\sigma^2_{\tau_\mathrm{d}}(e_{k-\tau_d}(\theta_{k-\tau_d}), \ldots, e_k(\theta_k))$, for $p = 1$, the function $g(e_0(\theta_0), \ldots, e_k(\theta_k))$ is defined as

$$g \triangleq \sqrt{\frac{\sigma^2_{\tau_\mathrm{n}}}{\sigma^2_{\tau_\mathrm{d}}}} - \sqrt{F^{-1}_{\tau_\mathrm{n},\tau_\mathrm{d}}(1 - \alpha)}, \tag{5.4}$$

where the error terms $e_k(\theta_k)$ are dropped for notational convenience. Using (5.4), forgetting is enabled when $\sigma^2_{\tau_\mathrm{n}}$ is statistically larger than $\sigma^2_{\tau_\mathrm{d}}$. The magnitude of the forgetting factor λ_k is inversely proportional to the difference between the square roots of the variance ratio and $F^{-1}_{\tau_\mathrm{n},\tau_\mathrm{d}}(1 - \alpha)$, thereby increasing the level of forgetting when there is more evidence that $\sigma^2_{\tau_\mathrm{n}}$ is larger $\sigma^2_{\tau_\mathrm{d}}$. A large value of α will cause the level of forgetting to be more sensitive to changes in the ratio of $\sigma^2_{\tau_\mathrm{n}}$ to $\sigma^2_{\tau_\mathrm{d}}$ compared to a smaller one.

For the case $p \geq 1$, the variances σ_{τ_n} and σ_{τ_d} are now covariance matrices Σ_{τ_n} and Σ_{τ_d}, and the ratio of the two covariance matrices is given by $\Sigma_{\tau_\mathrm{n}}\Sigma^{-1}_{\tau_\mathrm{d}}$. In this case, the ratio must be converted

into a scalar test statistic. Four commonly used test statistics are

- Wilks's Lambda: $|I + \frac{\tau_n}{\tau_d}\Sigma_{\tau_n}\Sigma_{\tau_d}^{-1}|^{-1} = \frac{|\tau_d\Sigma_{\tau_d}|}{|\tau_n\Sigma_{\tau_n}+\tau_d\Sigma_{\tau_d}|} = \prod_{i=1}^{n}\frac{1}{1+\mu_i}$,
- Lawley-Hotelling Trace: $\frac{\tau_n}{\tau_d}\mathrm{tr}(\Sigma_{\tau_n}\Sigma_{\tau_d}^{-1}) = \sum_{i=1}^{n}\mu_i$,
- Pillai's Trace: $\mathrm{tr}\left(\frac{\tau_n}{\tau_d}\Sigma_{\tau_n}\Sigma_{\tau_d}^{-1}(I + \frac{\tau_n}{\tau_d}\Sigma_{\tau_n}\Sigma_{\tau_d}^{-1})^{-1}\right) = \sum_{i=1}^{n}\frac{\mu_i}{1+\mu_i}$,
- Roy's Greatest Root: $\max_i(\mu_i)$,

where $\mu_i,\ i = 1,\ldots,n$ are the eigenvalues of $\frac{\tau_n}{\tau_d}\Sigma_{\tau_n}\Sigma_{\tau_d}^{-1}$ [75]. The Lawley-Hotelling trace is chosen due to its ease of use, similarity to the variance ratio in the F-Test, and availability of simple approximations. Using the Lawley-Hotelling trace with the approximation given by [55], Σ_{τ_n} is greater than Σ_{τ_d} with significance level α if

$$F_{p\tau_n,b}^{-1}(1-\alpha) < \frac{\tau_n}{\tau_d}\frac{\mathrm{tr}(\Sigma_{\tau_n}\Sigma_{\tau_d}^{-1})}{c}, \tag{5.5}$$

where

$$\begin{aligned} a &\triangleq \frac{(\tau_n+\tau_d-p-1)(\tau_d-1)}{(\tau_d-p-3)(\tau_d-p)}, \\ b &\triangleq 4+\frac{(p\tau_n+2)}{(a-1)},\quad c \triangleq \frac{p\tau_n(b-2)}{b(\tau_d-p-1)}. \end{aligned} \tag{5.6}$$

For $p = 1$, (5.5) is equivalent to the F-test. Given sample covariances of the past RLS prediction errors Σ_{τ_n} and Σ_{τ_d}, g is defined as

$$g \triangleq \sqrt{\frac{\tau_n}{\tau_d}\frac{\mathrm{tr}\left(\Sigma_{\tau_n}\Sigma_{\tau_d}^{-1}\right)}{c}} - \sqrt{F_{p\tau_n,b}^{-1}(1-\alpha)}. \tag{5.7}$$

The resulting RLS update using the F-test variable-rate forgetting factor (RLS/FTVRF) is given in Algorithm 1.

Some recommendations for the parameters τ_n, τ_d, η, and α are given as follows. A small τ_n will cause forgetting to occur sooner and is recommended for fast changing systems while a larger $\tau_n < 100$ will delay forgetting and is recommended for slowly changing systems. τ_d should be 5-10 times larger than τ_n. The parameter η adjusts the amount of forgetting and is recommended to set $0 < \eta \leq 1$, with lower values of η if lack of input persistency is expected. The variable α adjusts the sensitivity of the forgetting factor and should be less than 0.1 with smaller values reducing the sensitivity. Smaller values are recommended if the system has noisy measurements.

Algorithm 1 RLS-VRF using the F-test

Initialize: $\theta_0 \in \mathbb{R}^{n\times 1}$, $P_0 \in \mathbb{R}^{n\times n}$ positive-definite, $\tau_\mathrm{d} > \tau_\mathrm{n} \geq p$, $\eta > 0$, $\alpha > 0$, $k = 0$, and a buffer of $\tau_\mathrm{d} + 1$ previous errors

while $k \geq 0$ **do**

Measure $y_k \in \mathbb{R}^{p\times 1}$

$e_k \leftarrow y_k - \phi_k \theta_k$

Add e_k to error buffer and remove oldest entry

Compute sample covariance matrices $\Sigma_{\tau_\mathrm{n}} \in \mathbb{R}^{p\times p}$, $\Sigma_{\tau_\mathrm{d}} \in \mathbb{R}^{p\times p}$ from previous $\tau_\mathrm{n}+1$ and $\tau_\mathrm{d}+1$ errors from buffer

if $k \geq \tau_\mathrm{d} + 1$ **then**

Compute a, b, and c using (5.6)

$g \leftarrow$ (5.7)

else

$g \leftarrow 0$

end if

$\beta_k \leftarrow 1 + \eta g \mathbf{1}[g]$

$L_k \leftarrow \beta_k P_k$

$\theta_{k+1} \leftarrow \theta_k + P_{k+1}\phi_k^\mathrm{T}(y_k - \phi_k\theta_k)$

$P_{k+1} \leftarrow L_k - L_k\phi_k^\mathrm{T}(I_p + \phi_k L_k \phi_k^\mathrm{T})^{-1}\phi_k L_k$

$\phi_{k+1} \leftarrow$ Update regressor ϕ_k with current measurement and input

$k \leftarrow k + 1$

end while

5.2 Equivalence to the RLS/RMSVRF Function

In this section, we show that RLS/RMSVRF used in [50, 32] is a special case of RLS/FTVRF.

Proposition 5.2.1. *Assume* $\mathbb{E}[e(\theta)] = 0$. *For* $p = 1$ *and* $\alpha = 1 - F_{\tau_\mathrm{n},\tau_\mathrm{d}}(1)$, *the variable-rate forgetting function given in [50, 32] is a special case of* (5.7).

Proof. From (5.7), it follows that

$$
\begin{aligned}
g &\triangleq \sqrt{\frac{\tau_\mathrm{n}}{\tau_\mathrm{d}} \frac{\operatorname{tr}\left(\Sigma_{\tau_\mathrm{n}} \Sigma_{\tau_\mathrm{d}}^{-1}\right)}{c}} - \sqrt{F^{-1}_{p\tau_\mathrm{n},b}(1-\alpha)}, \\
&= \sqrt{\frac{\sigma^2_{\tau_\mathrm{n}}}{\sigma^2_{\tau_\mathrm{d}}}} - \sqrt{F^{-1}_{\tau_\mathrm{n},\tau_\mathrm{d}}(1-\alpha)}, \\
&= \sqrt{\frac{\frac{1}{\tau_\mathrm{n}} \sum_{i=k-\tau_n}^{k} e_i^2(\theta_i)}{\frac{1}{\tau_\mathrm{d}} \sum_{i=k-\tau_d}^{k} e_i^2(\theta_i)}} - \sqrt{F^{-1}_{\tau_\mathrm{n},\tau_\mathrm{d}}(1-\alpha)}, \\
&= \sqrt{\frac{\frac{1}{\tau_\mathrm{n}} \sum_{i=k-\tau_n}^{k} e_i^2(\theta_i)}{\frac{1}{\tau_\mathrm{d}} \sum_{i=k-\tau_d}^{k} e_i^2(\theta_i)}} - 1.
\end{aligned}
$$

□

For the suggested values of τ_n and τ_d given in [32], the forgetting function is equivalent to using a significance level of $\alpha \approx 0.5$, and is equal to 0.5 in the limit of the window sizes $\lim_{\tau_\mathrm{n},\tau_\mathrm{d}\to\infty} F_{\tau_\mathrm{n},\tau_\mathrm{d}}(1) = 0.5$. A significance level of $\alpha = 0.5$ means that 50% of the time, we conclude that $\sigma^2_{\tau_\mathrm{n}} > \sigma^2_{\tau_\mathrm{d}}$ when it is not true, causing forgetting to occur when it is not needed. This may lead to instability of the RLS/RMSVRF algorithm if the forgetting were to occur under nonpersistent excitation.

5.3 Examples

To demonstrate RLS/FTVRF, we use a similar example to the one used in [45]. Consider a mass-spring-damper system with $M = 5\,\mathrm{kg}$, $K = 1\,\frac{\mathrm{N}}{\mathrm{m}}$, and $C = 1\,\frac{\mathrm{N\,s}}{\mathrm{m}}$. After 100 steps, the system parameters change to $K = 10\,\frac{\mathrm{N}}{\mathrm{m}}$, and $C = 0.01\,\frac{\mathrm{N\,s}}{\mathrm{m}}$. The discrete-time transfer function is given by

$$
G_k(\mathbf{q}) = \begin{cases} \frac{0.4606\mathbf{q}+0.4307}{\mathbf{q}^2-1.64\mathbf{q}+0.8187}, & k < 100 \\ \frac{0.4218\mathbf{q}+0.4215}{\mathbf{q}^2-0.3116\mathbf{q}+0.998}, & k \geq 100, \end{cases} \tag{5.8}
$$

where $\mathbf{q}$ is the forward shift operator. We compare RLS/FTVRF to RLS with a constant-rate forgetting factor (RLS/CRF) of $\lambda = 0.99$ under noiseless measurements, noisy measurements, and nonpersistent inputs. We also compare to RLS/RMSVRF under noisy measurements. For all cases, $\theta_0 = 0_{5\times1}$, $P_0 = 100I_5$, $\tau_\text{n} = 10$, $\tau_\text{d} = 80$, $\eta = 1$, and $\alpha = 0.001$. The regressor is implemented as $\phi_k = \begin{bmatrix} y_{k-1} & y_{k-2} & u_k & u_{k-1} & u_{k-2} \end{bmatrix}$ so that the coefficients of the transfer function (5.8) are identified in the parameter vector θ_k.

5.3.1 Noiseless Measurements

Let the input into (5.8) be $u_k \sim \mathcal{N}(0, 1)$. First, comparing to RLS/CRF, from Figure 5.1 the parameters for RLS/FTVRF converge in less than 20 steps after the parameter change at $k = 100$. For RLS/CRF, the parameters are still not converged after 200 steps. Notice for RLS/FTVRF that once the prediction error increases, forgetting is enabled and $\text{tr}(P_k)$ increases as past data is given lower weight. Figure 5.2 shows the median, and 5th and 95th percentiles of 1000 Monte Carlo simulations of RLS/FTVRF. Notice that all simulations converge to the true parameters in less than 20 steps.

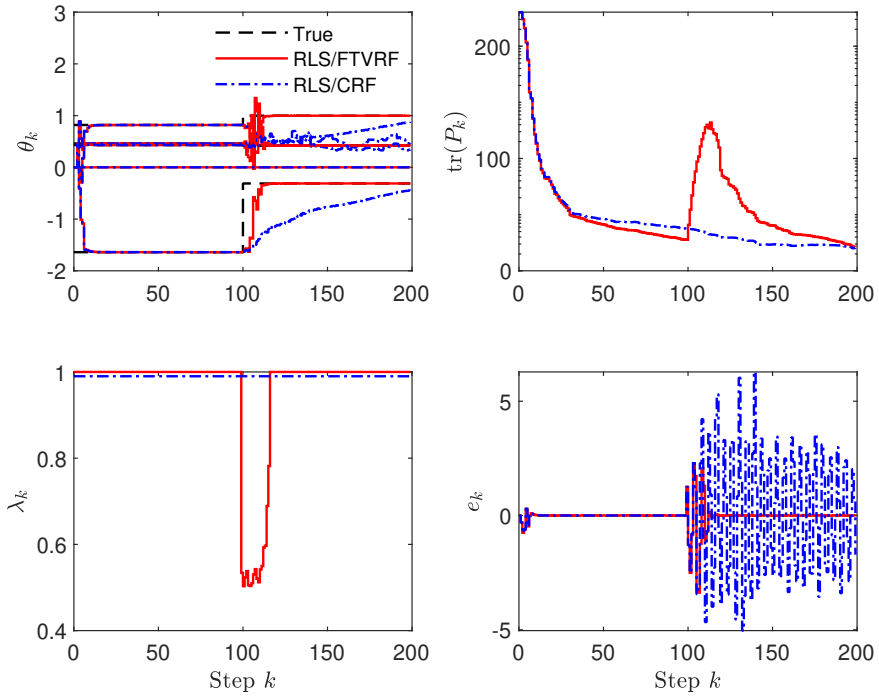

Figure 5.1: Noiseless measurements. Estimated parameters θ_k, trace of RLS covariance $\text{tr}(P_k)$, forgetting factor λ_k, and prediction error e_k for RLS/FTVRF and RLS/CRF.

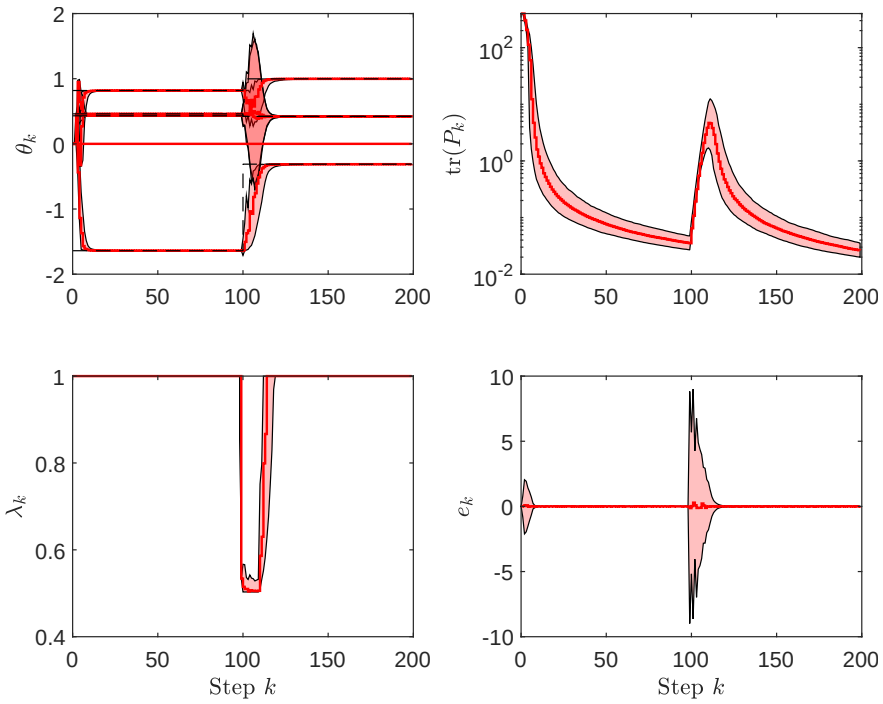

Figure 5.2: Noiseless measurements. Estimated parameters θ_k, trace of RLS covariance $\mathrm{tr}(P_k)$, forgetting factor λ_k, and prediction error e_k for RLS/FTVRF for 1000 simulations. The red line is the median and the upper and lower bounds are the 95th and 5th percentiles, respectively.

5.3.2 Noisy Measurements

Let the input into (5.8) be $u_k \sim \mathcal{N}(0, 1)$. Now the measurements are corrupted by noise $v_k \sim \mathcal{N}(0, 0.05)$. From Figure 5.3 the parameters for RLS/FTVRF converge in less than 20 steps after the parameters change at $k = 100$ despite the noisy measurements. For RLS/CRF, the parameters are still not converged after 200 steps. Notice for RLS/FTVRF that once the prediction error increases, forgetting is enabled and $\mathrm{tr}(P_k)$ increases as past data is given lower weight. The forgetting factor takes longer to reach its minimum value than in Figure 5.1, suggesting that the F-test limits the level of forgetting due to the uncertainty in whether the variance of errors has increased due to a parameter change or just temporarily due to noise. Figure 5.4 shows the median, and 5th and 95th percentiles of 1000 Monte Carlo simulations of RLS/FTVRF. Note that most of the simulation runs converge to the true parameters in less than 50 steps.

Figure 5.5 compares RLS/FTVRF to RLS/RMSVRF. Notice that RLS/RMSVRF enables forgetting at step 88 which is before any of the model parameters change and that forgetting also occurs at near the end of the simulation due to noise. RLS/FTVRF takes 8 more steps for its error to converge than RLS/RMSVRF, but convergence speed can be improved by increasing the significance level to $\alpha = 0.01$ without substantially risking forgetting before the parameter change or due to noise.

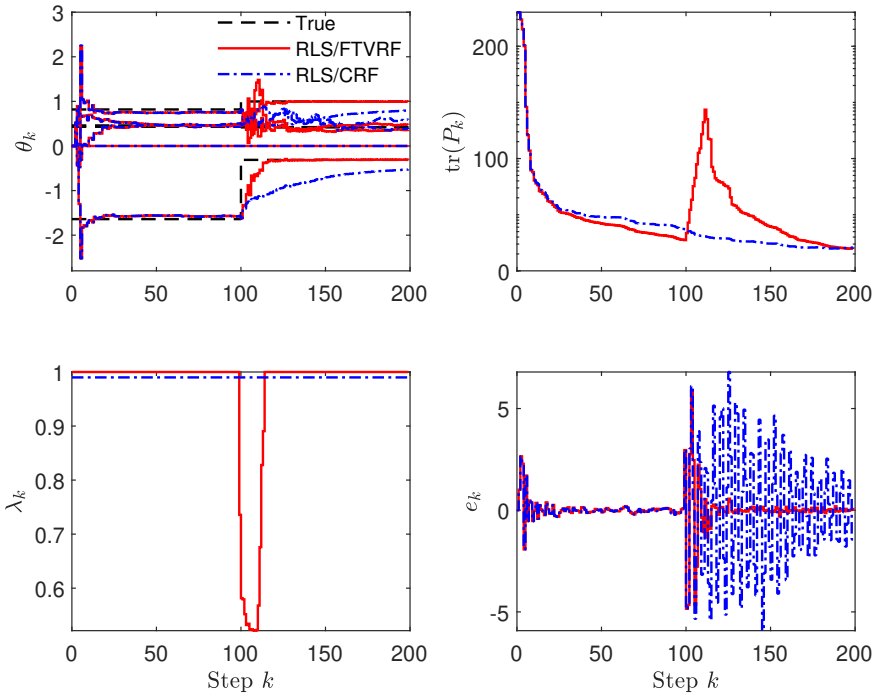

Figure 5.3: Noisy measurements. Estimated parameters θ_k, trace of RLS covariance $\mathrm{tr}(P_k)$, forgetting factor λ_k, and prediction error e_k for RLS/FTVRF and RLS/CRF.

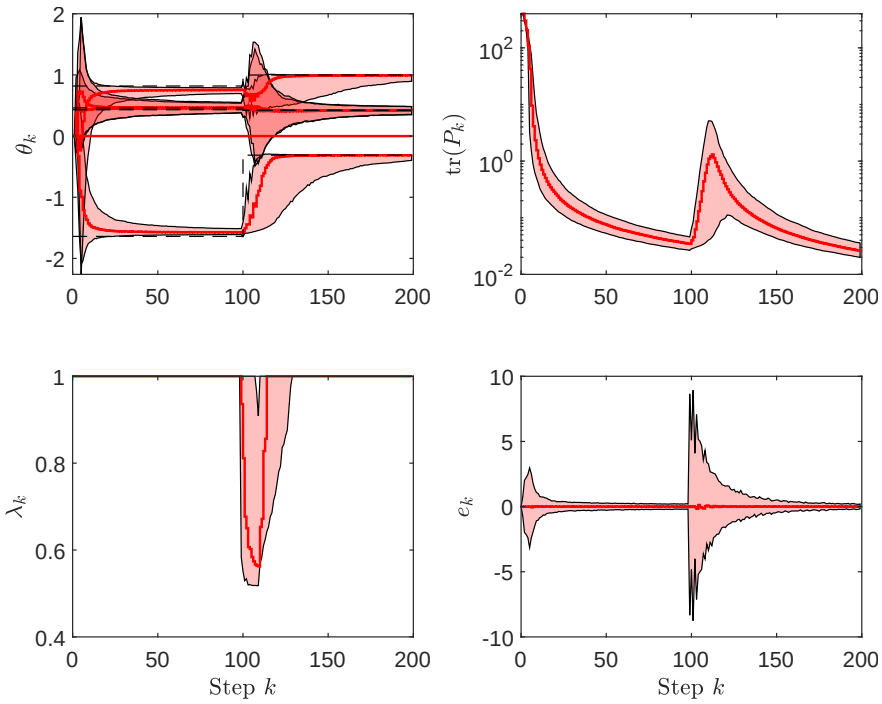

Figure 5.4: Noisy measurements. Estimated parameters θ_k, trace of RLS covariance $\mathrm{tr}(P_k)$, forgetting factor λ_k, and prediction error e_k for RLS/FTVRF for 1000 simulations. The red line is the median, and the upper and lower bounds are the 95th and 5th percentiles, respectively.

Figure 5.6 shows the median, and 5th and 95th percentiles of 1000 Monte Carlo simulations of the RLS/RMSVRF method. At step 80, 26% of simulations forget when it is not needed. Many simulations also forget long after the parameter change suggesting sensitivity to noise.

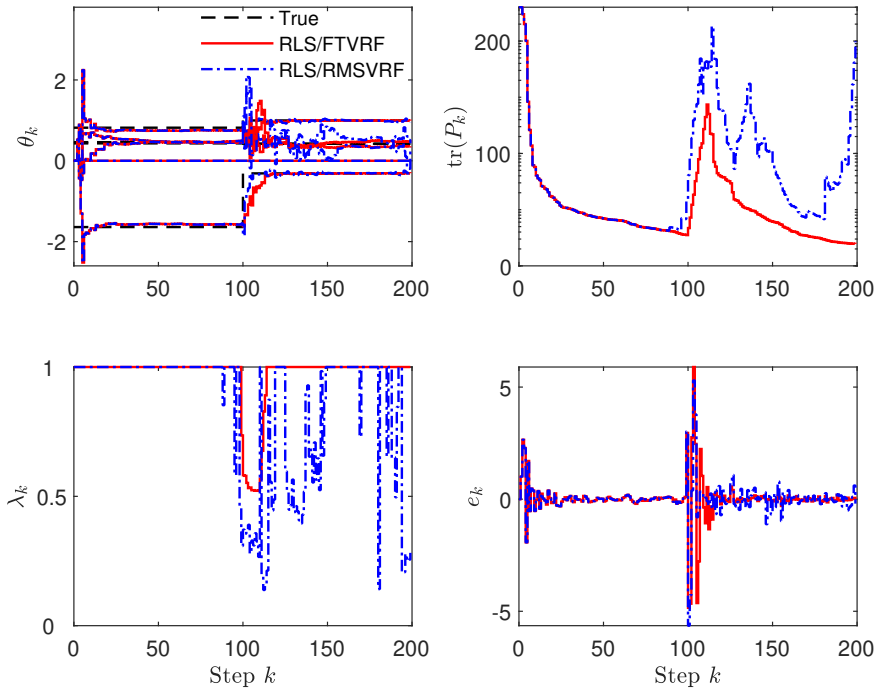

Figure 5.5: Noisy measurements. Estimated parameters θ_k, trace of RLS covariance $\mathrm{tr}(P_k)$, forgetting factor λ_k, and prediction error e_k for RLS/FTVRF and RLS/RMSVRF.

5.3.3 Nonpersistently Exciting Input

Let the input into (5.8) be

$$u_k = \begin{cases} \mathcal{N}(0,1), & \text{if } k < 100 \\ 0, & \text{if } k \geq 100, \end{cases} \tag{5.9}$$

with measurements corrupted by noise $v_k \sim \mathcal{N}(0, 0.05)$. The input is no longer persistently exciting once the parameters change, although the system may still be oscillating. In Figure 5.7 notice that over many steps for RLS/CRF, $\mathrm{tr}(P_k)$ continuously increases and will eventually cause RLS to 'blow-up' while for RLS/FTVRF, $\mathrm{tr}(P_k)$ stays bounded. Figure 5.8 shows the median, 5th and 95th percentiles of 1000 Monte Carlo simulations of RLS/FTVRF. Notice that all simulations keep $\mathrm{tr}(P_k)$ bounded.

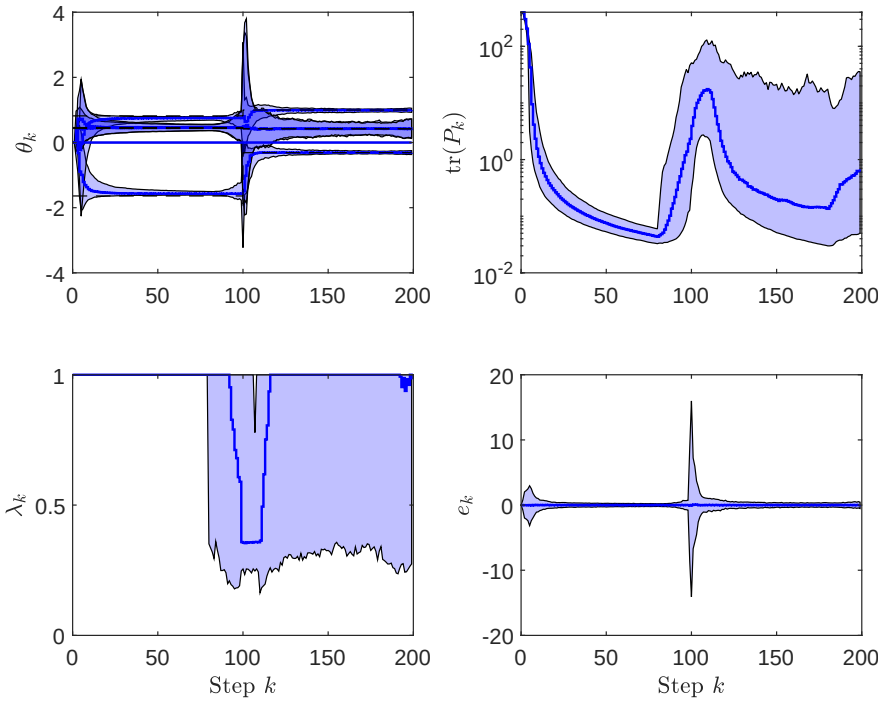

Figure 5.6: Noisy measurements. Estimated parameters θ_k, trace of RLS covariance $\mathrm{tr}(P_k)$, forgetting factor λ_k, and prediction error e_k for RLS/RMSVRF for 1000 simulations. The blue line is the median and the upper and lower bounds are the 95th and 5th percentiles, respectively. Notice how forgetting sometimes occurs even before the parameter change at 100 steps. Forgetting also sometimes occurs long after the parameter change due to noise.

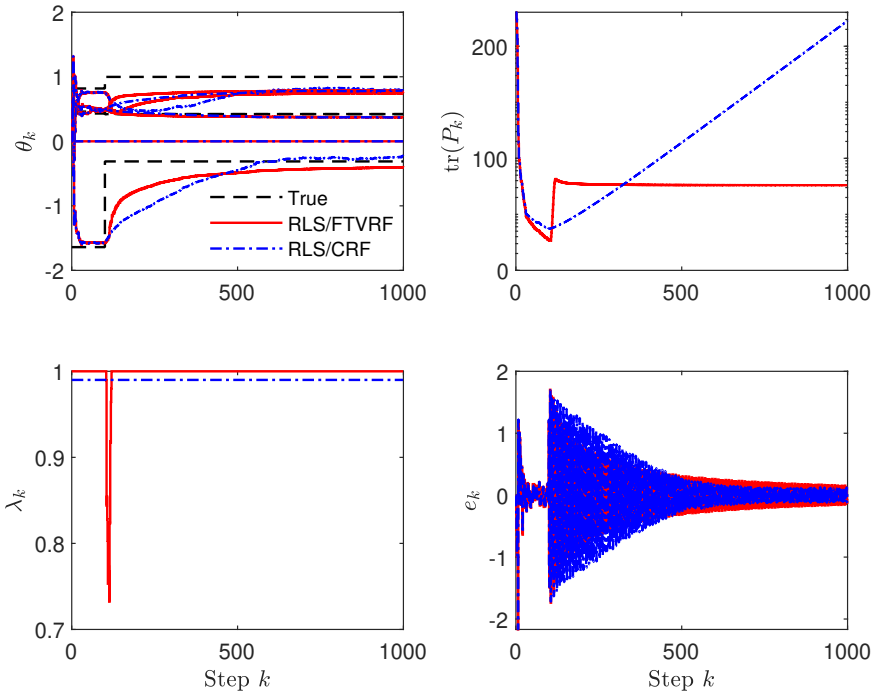

Figure 5.7: Nonpersistently exciting input. Estimated parameters θ_k, trace of RLS covariance $\mathrm{tr}(P_k)$, forgetting factor λ_k, and prediction error e_k for RLS/FTVRF and RLS/CRF.

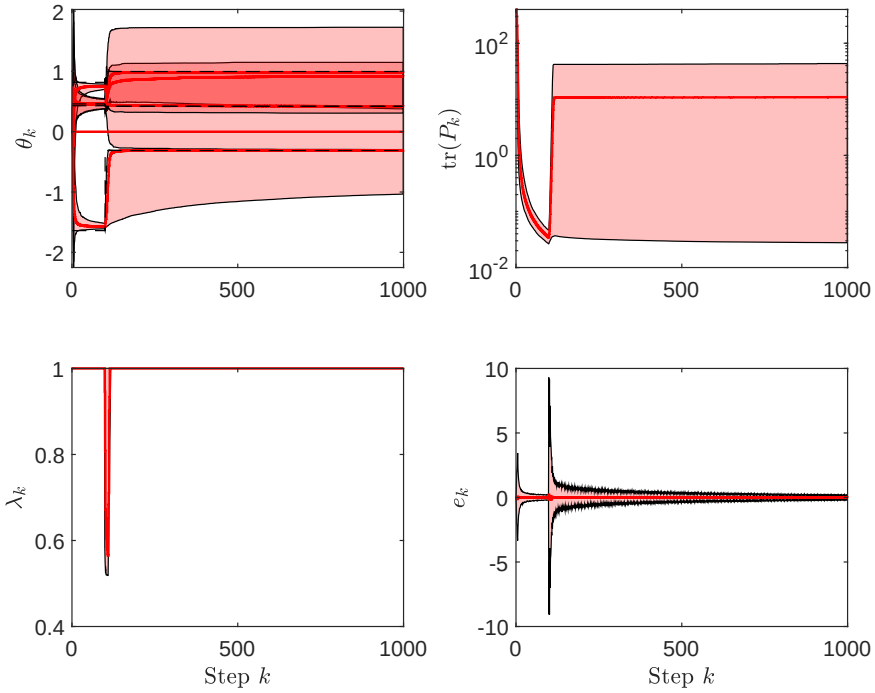

Figure 5.8: Nonpersistently exciting measurements. Estimated parameters θ_k, trace of RLS covariance $\mathrm{tr}(P_k)$, forgetting factor λ_k, and prediction error e_k for RLS/FTVRF for 1000 simulations. The red line is the median and the upper and lower bounds are the 95th and 5th percentiles, respectively.

5.4 Conclusions

In this chapter, we developed and investigated the performance of recursive least squares with F-test variable-rate forgetting (RLS/FTVRF), which uses a variable-rate forgetting factor for recursive least squares based on the F-test. The variable-rate forgetting method uses a ratio of covariances of errors from a short and long moving horizon to determine whether the underlying parameters have changed. A multivariate approximation of the F-test was used to extend the method to the multi-output case. The method was compared to a constant-rate forgetting factor in noiseless, noisy, and nonpersistently exciting input situations and also compared to the recursive least squares with root-mean-square variable-rate forgetting (RLS/RMSVRF) method used in [50, 32]. It was shown that RLS/FTVRF enabled forgetting when parameter changes occurred and prevented forgetting from occurring due to noise. In the nonpersistent input case, the method kept RLS from forgetting and kept the eigenvalues of the RLS covariance matrix bounded.

CHAPTER 6

Predictive Cost Adaptive Control of Flexible Structures with Harmonic and Broadband Disturbances

This chapter is focused on vibration suppression for large flexible structures such as space telescopes where closed-loop identification is unavoidable. Certain missions require on-orbit system identification to develop accurate operational models for vibration suppression, but due to the nature of the operational environment, these models are corrupted by unavoidable disturbances. These disturbances may arise from onboard equipment that cannot be shut down (for example, cryocoolers or control-moment gyros), and they may be due to environmental sources, such as solar pressure, magnetic torquing, and thermal gradients. Closed-loop system identification is also challenging due to the lack of consistency arising from correlated control inputs and plant outputs [77, 78, 79]. Specialized techniques, such as prediction error methods [80] can overcome this problem to some extent, but are not generally amenable to online implementation.

To address this problem, this chapter considers PCAC which was developed in Section 2.3. Since the online identification in PCAC is performed in the presence of disturbances, it can be expected that the disturbances will degrade the accuracy of the identified model. Interestingly, however, in the case of harmonic disturbances, the identified model incorporates a model of the harmonic disturbances, which enables the identified model to predict the future forced response of the structure. As shown in [33], these predictions facilitate the receding horizon optimization that MPC uses to determine the future control inputs. The contents of the chapter are as follows. Section 6.1 describes the class of flexible structure models of interest. Section 6.2 contains an investigation of PCAC for disturbance rejection of a flexible structure model for harmonic and broadband disturbances.

6.1 Problem Formulation

Consider a flexible structure modeled by

$$M\ddot{q}(t) + C\dot{q}(t) + Kq(t) = Bu(t) + B_w w(t), \tag{6.1}$$

where M, C, and $K \in \mathbb{R}^{n\times n}$ are, respectively, the positive-definite mass, positive-semidefinite damping, and positive-definite stiffness matrices of the structure, $q(t) \in \mathbb{R}^{n\times 1}$ is a state vector describing the generalized displacements, $B \in \mathbb{R}^{n\times m}$ is the control input distribution matrix, $B_w \in \mathbb{R}^{n\times m_w}$ is the exogenous disturbance input matrix, $u(t) \in \mathbb{R}^{m\times 1}$ is the control input, and $w(t) \in \mathbb{R}^{m_w\times 1}$ is the exogenous disturbance. The objective is to reject the effect of the disturbance $w(t)$ on $q(t)$ using control inputs $u(t)$ under the following assumptions.

Assumption 1. *The control input $u(t)$ is determined by a discrete-time controller with sample time T_s whose computed digital control request is converted to an analog signal by means of a ZOH circuit and is implemented by electromechanical actuators. Because of the ZOH, $u(t)$ is constant over each time period $[kT_s, (k+1)T_s)$, where k is the time step.*

Assumption 2. *M, C, and K are unknown except for an upper bound on the number of degrees of freedom (DOF) within the control bandwidth. However, additional modes may lie above the Nyquist rate of the sampled-data controller.*

Note that the modes whose frequencies are above the Nyquist rate of the sampled-data controller are subjected to aliasing and thus constitute spillover.

6.2 Numerical Examples

Consider the 4-bay truss structure shown in Figure 6.1a. The structure is assumed to be made of pinned truss elements, where each element has local mass and stiffness matrices of the form

$$\bar{M} = \frac{\rho AL}{6}\begin{bmatrix} 2 & 0 & 1 & 0 \\ 0 & 2 & 0 & 1 \\ 1 & 0 & 2 & 0 \\ 0 & 1 & 0 & 2 \end{bmatrix}, \quad \bar{K} = \frac{EA}{L}\begin{bmatrix} 1 & 0 & -1 & 0 \\ 0 & 0 & 0 & 0 \\ -1 & 0 & 1 & 0 \\ 0 & 0 & 0 & 0 \end{bmatrix}. \tag{6.2}$$

The local state $\bar{q}(t) = \begin{bmatrix} \delta_{\bar{x},1} & \delta_{\bar{y},1} & \delta_{\bar{x},2} & \delta_{\bar{y},2} \end{bmatrix}^{\mathrm{T}}$ corresponds to the local x and y displacements of each end of the element, where $\bar{M}$ is the local consistent mass matrix, $\bar{K}$ the local stiffness matrix, E is the elastic modulus, A is the cross-sectional area of the truss member, L is the length of

the truss member, and ρ is the density of the truss member material. The individual local mass and stiffness matrices are then assembled into the global mass and stiffness matrices M and K using appropriate coordinate transformations, and states corresponding to boundary constraints are removed. The global damping matrix C is constructed by assuming each normal mode has the same damping ratio $\zeta = 0.005$. The material is chosen to be a graphite-epoxy composite with properties $E = 1 \times 10^{11}$ Pa, $A = 5 \times 10^{-4}\,\mathrm{m}^2$, and $\rho = 1700\,\frac{\mathrm{kg}}{\mathrm{m}^3}$ [81, 82]. There are two 2-kg force actuators located at nodes 3 and 4, with control authority in the x-direction, and x-direction displacement sensors at nodes 5, 6, 7, and 8. The entire state of the structure is not measured. There are also 1-kg masses on nodes 1, 2, 5, 6, 7 and 8. The actuator force is limited to 10 N.

The objective is to investigate the ability of PCAC to suppress the effect of harmonic and broadband disturbances entering from node 1 on node 8 of the truss structure. For a large structure such as a space telescope, the displacement of node 8 is representative of the line-of-sight performance, and the disturbances entering at node 1 represent disturbances from control-moment gyros or other internal components. Measurements are corrupted with white noise such that a sensor measuring a 0.1-Hz disturbance at node 8 has a signal-to-noise ratio (SNR) of 40-dB. The measurements also have a gain of 10x.

The transfer function matrix representing the portion of the structure under consideration is given by

$$G(s) = \begin{bmatrix} G_{5,1}(s) & G_{5,3}(s) & G_{5,4}(s) \\ G_{6,1}(s) & G_{6,3}(s) & G_{6,4}(s) \\ G_{7,1}(s) & G_{7,3}(s) & G_{7,4}(s) \\ G_{8,1}(s) & G_{8,3}(s) & G_{8,4}(s) \end{bmatrix}, \tag{6.3}$$

where $G_{i,j}(s)$ is the transfer function from an x-direction input at node j to a x-direction displacement in node i. The maximum singular values of $G(\jmath\omega)$ are shown in Figure 6.1b. Notice that the structure is lightly damped with a cluster of modes near 10-Hz.

PCAC is initialized with the cold-start model $\theta_0 = 10^{-10} 1_{600\times 1}$, $\hat{n} = 25$, $P_0 = 1 I_{600}$, $\eta = 0.1$, $\tau_\mathrm{n} = 40$, $\tau_\mathrm{d} = 200$, $\alpha = 0.001$, $\ell = 40$, $Q = 10^6 I_{160}$, $R = I_{160}$, $C_\mathrm{t} = \begin{bmatrix} 0_{1\times 3} & 1 \end{bmatrix}$, $C_\mathrm{c} = 0_4$, $C = 0_{4\times 4}$, and $\mathcal{D} = 0_{4\times 1}$. C_t was chosen such that PCAC attempts to minimize the response of node 8, the fourth measurement. In the below figures, the open-loop response is denoted by OL and the closed-loop response is denoted by CL.

6.2.1 Harmonic Disturbance

The structure is excited by a harmonic disturbance consisting of sinusoidal tones at 0.354, 1, and 1.55-Hz entering in the x-direction of node 1 with PCAC running at a 50-Hz. Figures 6.2 and 6.3

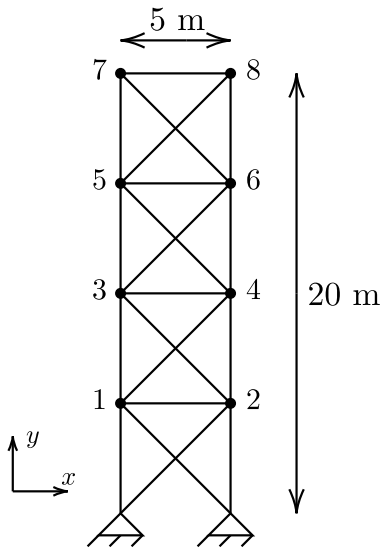

(a) Schematic of the truss structure with the nodes labeled.

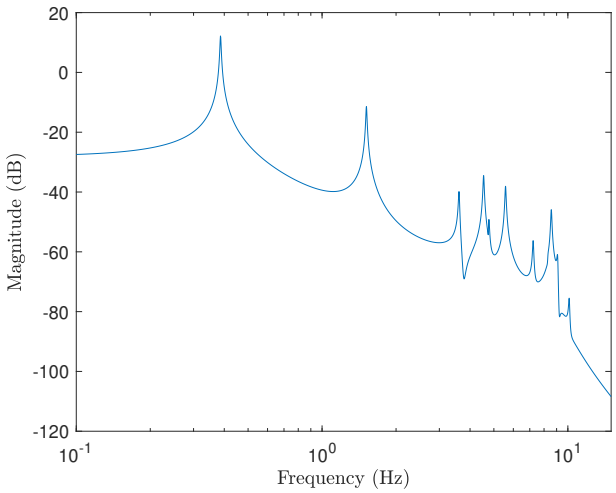

(b) Magnitude plot of the largest singular values of $G(\jmath\omega)$.

show that the disturbance is suppressed in all measurements, with the most suppression occurring on nodes 7 and 8. Figure 6.4 shows the norm of the identification coefficients $\|\theta_k\|$ and the trace of the identification covariance P_k. Notice that the disturbance is suppressed before either $\|\theta_k\|$ or $\mathrm{tr}(P_k)$ converge with $\|\theta_k\|$ converging soon after.

6.2.2 Band-Limited Broadband Disturbance

The structure is excited by a 25-Hz band-limited broadband disturbance entering in the x-direction of node 1 with PCAC running at a 50-Hz. Figures 6.5 and 6.6 show that the disturbance is suppressed in all measurements, with the most suppression occurring on nodes 7 and 8. Figure 6.7 shows the norm of the estimated model coefficients $\|\theta_k\|$ and the trace of the estimated model-coefficient covariance P_k. Notice that the disturbance is suppressed before $\|\theta_k\|$ or $\mathrm{tr}(P_k)$ converges.

6.2.3 Band-Limited Broadband Disturbance with Aliasing

In practice, a large structure has many modes outside the control bandwidth that can be excited by external disturbances and are spilled over due to sampling. The response of these excited modes aliases onto the control bandwidth and can cause instability if not accounted for in the original control design. Additionally, the ZOH control input can also excite these undersampled modes. To demonstrate robustness of PCAC to aliasing and spillover, the sample rate is reduced to 10 Hz so that there exist structural modes and disturbances outside the control bandwidth. The structure is

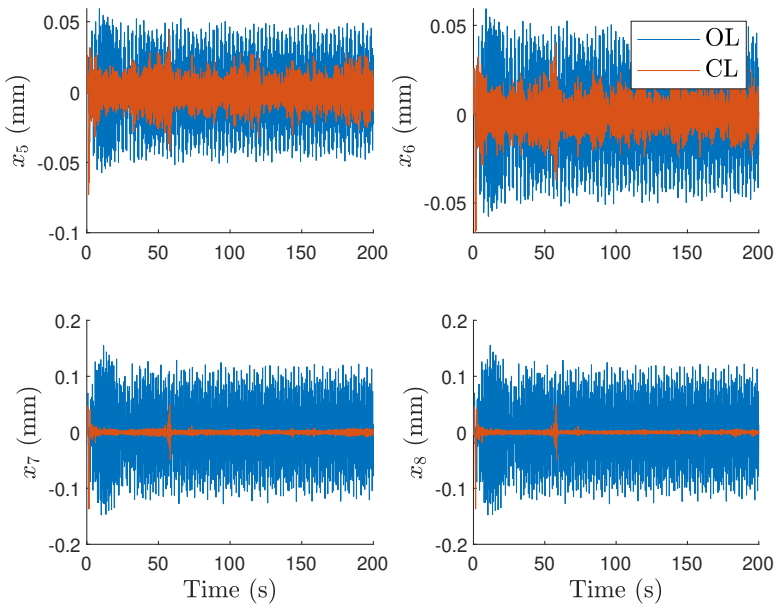

Figure 6.2: Harmonic disturbance: Open- and closed-loop response subject to the band-limited broadband disturbance. Starting from the top left moving clockwise, the measurements are the x-direction displacements of nodes 5, 6, 7, and 8, respectively. The closed-loop response converges within 10 s.

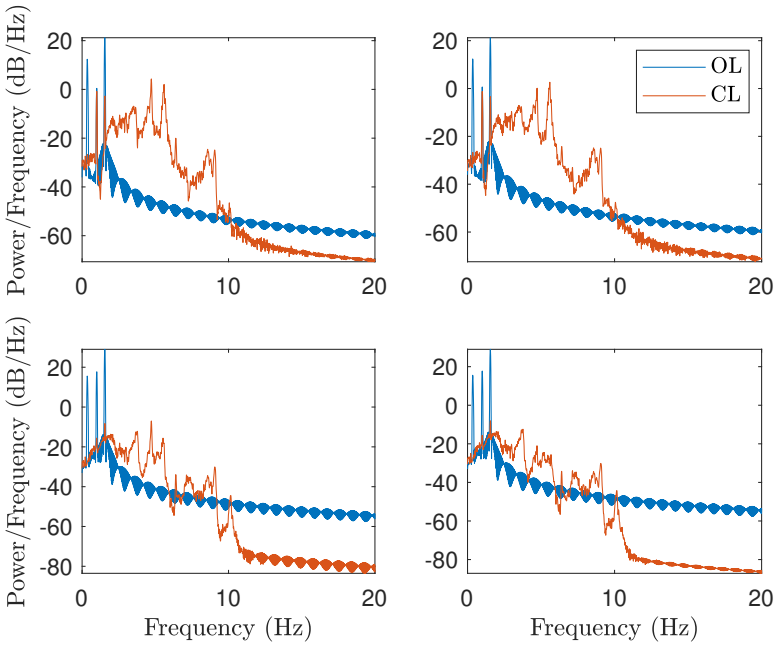

Figure 6.3: Harmonic disturbance: Power spectral densities of the open- and closed-loop systems. Starting from the top left moving clockwise, the measurements are the x-direction displacements of nodes 5, 6, 7, and 8, respectively. Notice that the 3 peaks corresponding to the 3 sinusoidal disturbances are suppressed in closed-loop for nodes 7 and 8.

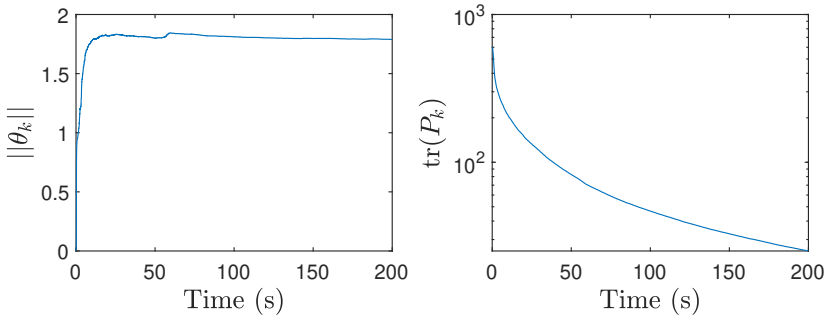

Figure 6.4: Harmonic disturbance: Norm of the estimated model coefficients θ_k and the trace of the matrix P_k.

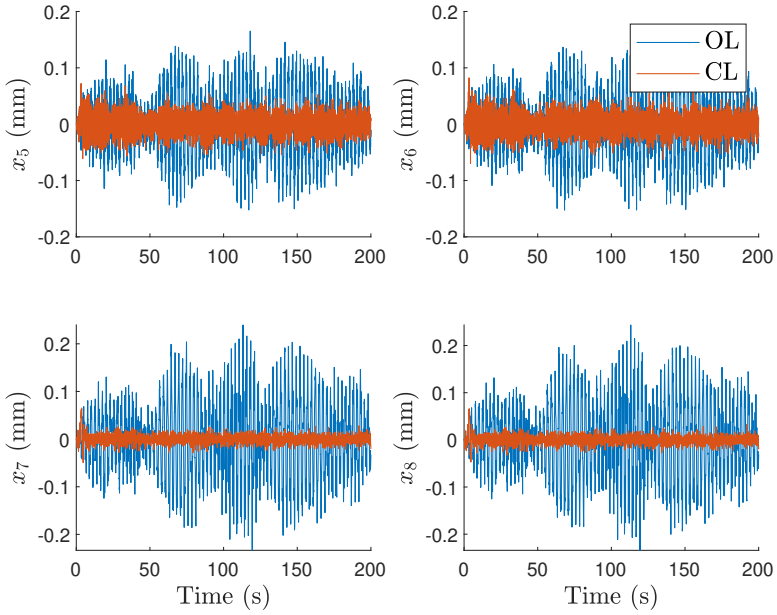

Figure 6.5: Band-limited broadband disturbance: Open- and closed-loop response subject to the band-limited broadband disturbance. Starting from the top left moving clockwise, the measurements are the x-direction displacements of nodes 5, 6, 7, and 8, respectively. Notice that the broadband disturbance is suppressed within 10 s for nodes 5 and 6, and within 5 s for nodes 7 and 8.

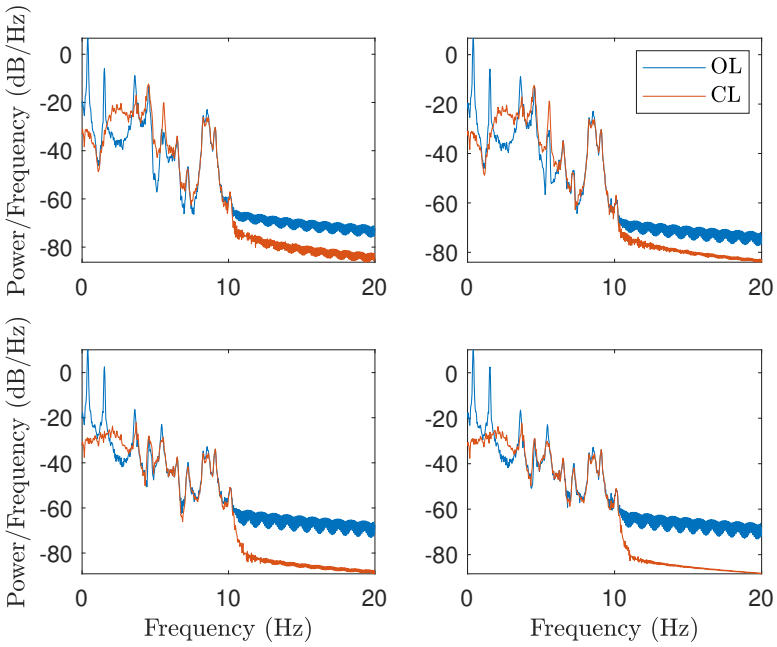

Figure 6.6: Band-limited broadband disturbance: Power spectral densities of the open- and closed-loop systems. Starting from the top left moving clockwise, the measurements are the x-direction displacements of nodes 5, 6, 7, and 8, respectively. Notice that most of the peaks in the open-loop response of nodes 7 and 8 are suppressed in closed-loop.

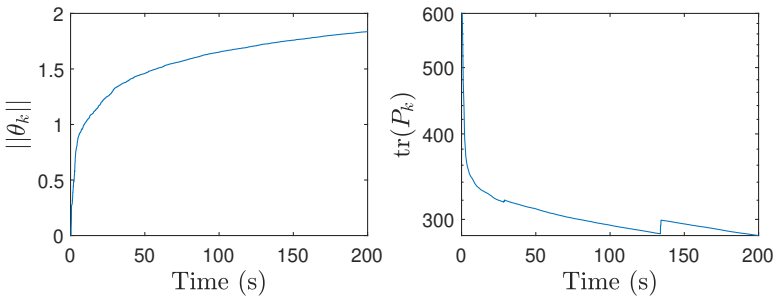

Figure 6.7: Band-limited broadband disturbance: Norm of the identification coefficients θ_k and the trace of the matrix P_k.

excited by a 50 Hz band-limited noise disturbance entering in the x-direction of node 1. Figures 6.8 and 6.9 show that the broadband disturbance is suppressed in all measurements despite aliased disturbances and spillover. Note also that the initial transient is larger than in the nonaliased case. Figure 6.10 shows that the identification coefficients do not need to be converged for the disturbance to be suppressed.

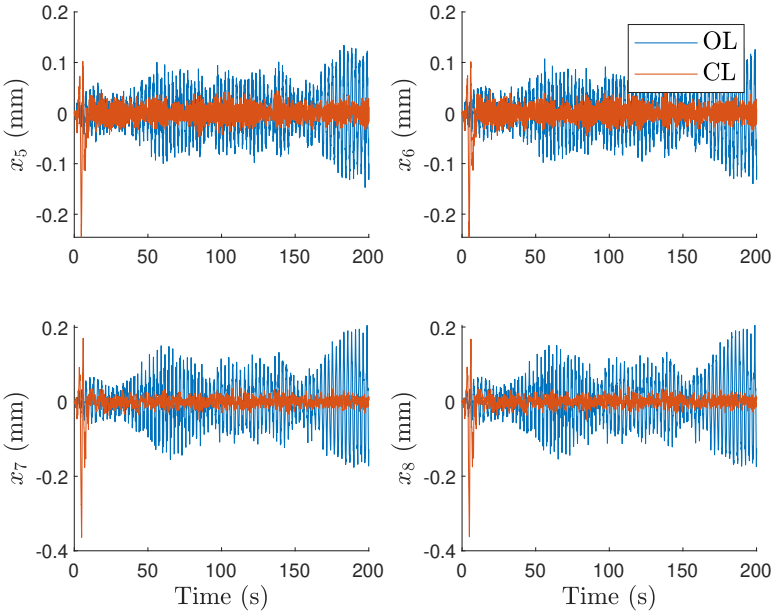

Figure 6.8: Band-limited broadband disturbance with aliasing: Open- and closed-loop response subject to the band-limited broadband disturbance. Starting from the top left moving clockwise, the measurements are the x-direction displacements of nodes 5, 6, 7, and 8, respectively. Notice that the broadband disturbance is suppressed within 15 s for nodes 5 and 6, and within 10 s for nodes 7 and 8.

6.3 Conclusions

This chapter investigated the performance of PCAC for disturbance rejection of flexible structures. A model of a large truss structure was developed and used to investigate MIMO disturbance rejection for unknown harmonic and broadband disturbances as well as broadband disturbances with aliasing. PCAC was shown to suppress the disturbances in all cases without a priori knowledge of the dynamics or disturbance spectra.

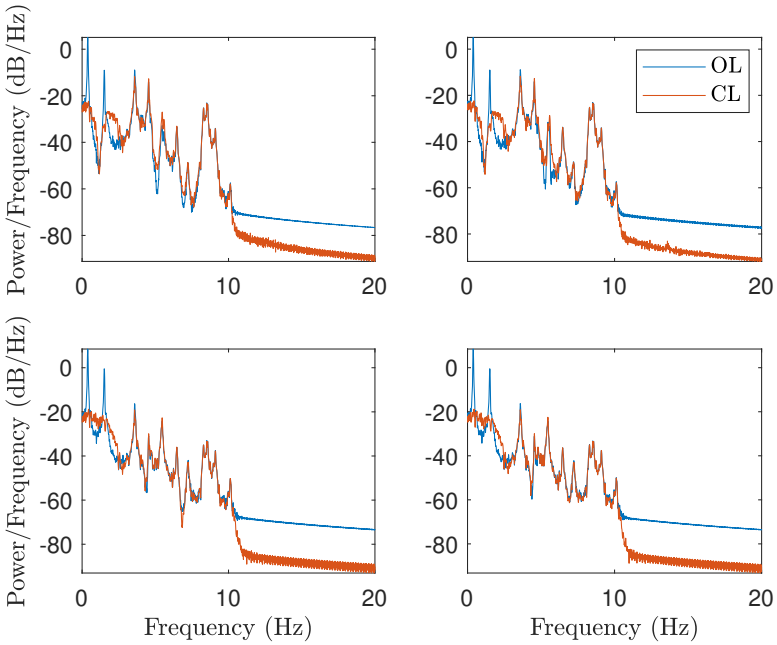

Figure 6.9: Band-limited broadband disturbance with aliasing: Power spectral densities of the open- and closed-loop systems. Starting from the top left moving clockwise, the measurements are the x-direction displacements of nodes 5, 6, 7, and 8, respectively. Notice that the modes inside the control bandwidth are suppressed.

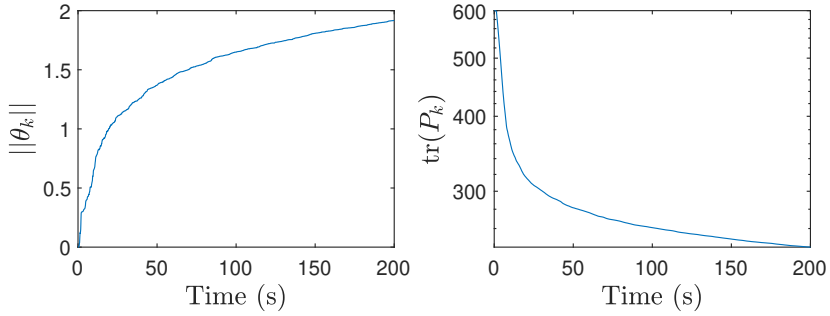

Figure 6.10: Band-limited broadband disturbance with aliasing: Norm of the identification coefficients θ_k and the trace of the matrix P_k.

CHAPTER 7

Adaptive Force-Control Augmentation for Small Celestial Body Sampling

In this chapter we investigate the spacecraft surface sampling problem. The objective of a sampling mission is to bring a spacecraft with a sampler in contact with the surface of a celestial body and maintain a desired contact force in order to capture a sample from the surface [11, 12]. The resulting samples are used to further scientific knowledge about the origins of the solar system and universe. Before contact with the surface, surface properties such as the compliance are uncertain. Additional challenges arise due to unknown nonlinear contact dynamics such as hysteretic effects, and the inability to use the spacecraft thrusters to augment the contact force. Therefore, the controller must be designed to be robust to a wide variety of surface properties. If the true surface properties are outside expectations, mission performance will be adversely affected possibly leading to mission failure.

The challenges associated with surface sampling missions motivates an alternative adaptive approach to the surface sampling control problem. The control algorithm proposed consists of a feedback linearization controller with a nominal robust controller that is augmented using PCAC to adaptively regulate the contact force of the sampler when subject to a surface with unknown properties. The robust controller is developed using a set of linear matrix inequalities (LMIs) to guarantee stability for a wide range of surface properties. The robust controller on its own is unable to meet the performance requirements of the mission and therefore PCAC is used to augment the commanded sampling arm torques. The present chapter extends the robust control algorithm given in [83] to the case of an adaptive controller.

7.1 Spacecraft Dynamics and Modeling

An overview of the spacecraft equations of motion and contact dynamics are given in this section. For simplicity, we assume a two-dimensional model, where all masses are rigid. Consider

the spacecraft with a 2-link sampling arm as shown in Figure 7.1. The relative joint angles are given by θ_1 and θ_2, the control torques by τ_1 and τ_2, the spacecraft bus mass by m_{sc}, the link masses and inertias by m_1, m_2, $\bar{I}_1$, and $\bar{I}_2$ respectively, the link lengths and distance to the link center of mass by L_1, L_2, R_1, and R_2, the sampler position relative to the surface by x and y, and the sampler mass by m_s. The contact and friction forces due to the surface are given by F_c and F_f. Due to the small gravitational forces in this environment, gravitational forces are assumed to be negligible relative to the contact forces and are ignored during the contact phase. The resulting equations of motion have the form

$$M(q)\ddot{q} + D(q,\dot{q})\dot{q} = Q \tag{7.1}$$

$$q \triangleq \begin{bmatrix} \theta_1 \\ \theta_2 \\ x \\ y \end{bmatrix}, \quad \dot{q} \triangleq \begin{bmatrix} \dot{\theta}_1 \\ \dot{\theta}_2 \\ \dot{x} \\ \dot{y} \end{bmatrix}, \tag{7.2}$$

where $M(q)$, $D(q,\dot{q})$, and Q are the mass, damping and generalized force matrices. Details of the derivation and structure of these matrices without the sampler mass are given in [83]. The equations of motion are derived below for reference.

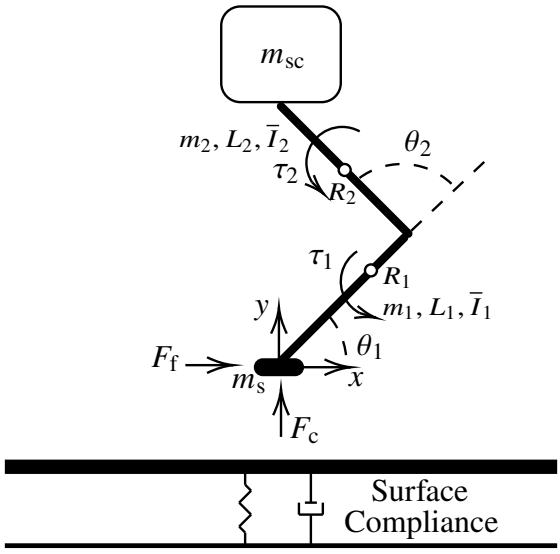

Figure 7.1: Spacecraft model for celestial body sampling.

The position the center of mass of each component of the spacecraft relative to the surface is

given by

$$p_{\mathrm{s}} = \begin{bmatrix} x \\ y \end{bmatrix}, \quad p_1 = \begin{bmatrix} x + R_1 \cos(\theta_1) \\ y + R_1 \sin(\theta_1) \end{bmatrix}, \tag{7.3}$$

$$p_2 = \begin{bmatrix} x + L_1 \cos(\theta_1) + R_2 \cos(\theta_1 + \theta_2) \\ y + L_1 \sin(\theta_1) + R_2 \sin(\theta_1 + \theta_2) \end{bmatrix}, \tag{7.4}$$

$$p_{\mathrm{sc}} = \begin{bmatrix} x + L_1 \cos(\theta_1) + L_2 \cos(\theta_1 + \theta_2) \\ y + L_1 \sin(\theta_1) + L_2 \sin(\theta_1 + \theta_2) \end{bmatrix}, \tag{7.5}$$

and velocities by

$$v_{\mathrm{s}} = \begin{bmatrix} \dot{x} \\ \dot{y} \end{bmatrix}, \quad v_1 = \begin{bmatrix} \dot{x} - R_1 \dot{\theta}_1 \sin(\theta_1) \\ \dot{y} + R_1 \dot{\theta}_1 \cos(\theta_1) \end{bmatrix}, \tag{7.6}$$

$$v_2 = \begin{bmatrix} \dot{x} - L_1 \dot{\theta}_1 \sin(\theta_1) - R_2(\dot{\theta}_1 + \dot{\theta}_2) \sin(\theta_1 + \theta_2) \\ \dot{y} + L_1 \dot{\theta}_1 \cos(\theta_1) + R_2(\dot{\theta}_1 + \dot{\theta}_2) \cos(\theta_1 + \theta_2) \end{bmatrix}, \tag{7.7}$$

$$v_{\mathrm{sc}} = \begin{bmatrix} \dot{x} - L_1 \dot{\theta}_1 \sin(\theta_1) - L_2(\dot{\theta}_1 + \dot{\theta}_2) \sin(\theta_1 + \theta_2) \\ \dot{y} + L_1 \dot{\theta}_1 \cos(\theta_1) + L_2(\dot{\theta}_1 + \dot{\theta}_2) \cos(\theta_1 + \theta_2) \end{bmatrix}. \tag{7.8}$$

The velocities and angular velocities of each center of mass can then be written as

$$v_{\mathrm{s}} = A(q)\dot{q} \triangleq \begin{bmatrix} 0 & 0 & 1 & 0 \\ 0 & 0 & 0 & 1 \end{bmatrix} \dot{q} \tag{7.9}$$

$$v_1 = B(q)\dot{q} \triangleq \begin{bmatrix} -R_1 \sin(\theta_1) & 0 & 1 & 0 \\ R_1 \cos(\theta_1) & 0 & 0 & 1 \end{bmatrix} \dot{q} \tag{7.10}$$

$$v_2 = C(q)\dot{q} \triangleq \begin{bmatrix} -L_1 \sin(\theta_1) - R_2 \sin(\theta_1 + \theta_2) & -R_2 \sin(\theta_1 + \theta_2) & 1 & 0 \\ L_1 \cos(\theta_1) + R_2 \cos(\theta_1 + \theta_2) & R_2 \cos(\theta_1 + \theta_2) & 0 & 1 \end{bmatrix} \dot{q} \tag{7.11}$$

$$v_{\mathrm{sc}} = D(q)\dot{q} \triangleq \begin{bmatrix} -L_1 \sin(\theta_1) - L_2 \sin(\theta_1 + \theta_2) & -L_2 \sin(\theta_1 + \theta_2) & 1 & 0 \\ L_1 \cos(\theta_1) + L_2 \cos(\theta_1 + \theta_2) & L_2 \cos(\theta_1 + \theta_2) & 0 & 1 \end{bmatrix} \dot{q} \tag{7.12}$$

$$\dot{\theta}_1 = E(q)\dot{q} \triangleq \begin{bmatrix} 1 & 0 & 0 & 0 \end{bmatrix} \dot{q} \tag{7.13}$$

$$\dot{\theta}_1 + \dot{\theta}_2 = F(q)\dot{q} \triangleq \begin{bmatrix} 1 & 1 & 0 & 0 \end{bmatrix} \dot{q} \tag{7.14}$$

The kinetic energy T of the spacecraft can then be written as

$$T = \frac{1}{2} \dot{q}^{\mathrm{T}} M(q) \dot{q}, \tag{7.15}$$

where,

$$M(q) \triangleq m_s A^{\mathrm{T}}(q)A(q) + m_1 B^{\mathrm{T}}(q)B(q) + m_2 C^{\mathrm{T}}(q)C(q) + m_{sc} D^{\mathrm{T}}(q)D(q) + I_1 E^{\mathrm{T}}(q)E(q) + I_2 F^{\mathrm{T}}(q)F(q). \tag{7.16}$$

The following property is given for two matrix functions $A(q)$ and $B(q)$ [84],

$$\frac{\partial}{\partial q}[A(q)B(q)] \triangleq [I \otimes A(q)]\frac{\partial B(q)}{\partial q} + \frac{\partial A(q)}{\partial q}B(q), \tag{7.17}$$

where

$$\frac{\partial A(q)}{\partial q} = \begin{bmatrix} \frac{\partial A(q)}{\partial q_1} \\ \vdots \\ \frac{\partial A(q)}{\partial q_n} \end{bmatrix}. \tag{7.18}$$

The equations of motion are then given by Lagrange's equations

$$\frac{d}{dt}\frac{\partial T}{\partial \dot{q}} - \frac{\partial T}{\partial q} = Q, \tag{7.19}$$

$$M(q)\ddot{q} + \dot{M}(q)\dot{q} - \frac{\partial T}{\partial q} = Q. \tag{7.20}$$

where

$$\dot{M}(q) = \left(\frac{\partial M(q)}{\partial q}\right)^{\mathrm{T}} (\dot{q} \otimes I_4), \tag{7.21}$$

and using (7.17)

$$\frac{\partial T}{\partial q} = \frac{\partial}{\partial q}[\frac{1}{2}\dot{q}^{\mathrm{T}}M(q)\dot{q}] = \frac{1}{2}[I_4 \otimes \dot{q}^{\mathrm{T}}]\frac{\partial M(q)}{\partial q}\dot{q}, \tag{7.22}$$

which leads to

$$M(q)\ddot{q} + \left[\left(\frac{\partial M(q)}{\partial q}\right)^{\mathrm{T}} (\dot{q} \otimes I_4) - \frac{1}{2}[I_4 \otimes \dot{q}^{\mathrm{T}}]\frac{\partial M(q)}{\partial q}\right]\dot{q} = Q, \tag{7.23}$$

where

$$\left(\frac{\partial M(q)}{\partial q}\right)^{\mathrm{T}} (\dot{q} \otimes I_4) - \frac{1}{2}[I_4 \otimes \dot{q}^{\mathrm{T}}]\frac{\partial M(q)}{\partial q} \triangleq D(q, \dot{q}). \tag{7.24}$$

During contact, the generalized force is given by

$$Q_i = \tau_1 \frac{\partial \dot{\theta}_1}{\partial \dot{q}_i} + \tau_2 \frac{\partial (\dot{\theta}_1 + \dot{\theta}_2)}{\partial \dot{q}_i} + F_{\mathrm{f}} \frac{\partial \dot{x}}{\partial \dot{q}_i} + F_{\mathrm{c}} \frac{\partial \dot{y}}{\partial \dot{q}_i} \quad \text{for} \quad i = 1, 2, 3, 4 \tag{7.25}$$

$$Q = \begin{bmatrix} 1 & 1 & 0 & 0 \\ 0 & 1 & 0 & 0 \\ 0 & 0 & 1 & 0 \\ 0 & 0 & 0 & 1 \end{bmatrix} \begin{bmatrix} \tau_1 \\ \tau_2 \\ F_{\mathrm{f}} \\ F_{\mathrm{c}} \end{bmatrix}. \tag{7.26}$$

For the contact force, two models commonly used for small celestial body sampling are used. The first is the linear Kelvin-Voigt model [85] given by

$$F_{\mathrm{c}} = -k_{\mathrm{s}} y - c_{\mathrm{s}} \dot{y}, \tag{7.27}$$

where k_{s} and c_{s} are the stiffness and damping of the surface material, The second is a nonlinear Hunt-Crossley model [85, 86, 87] given by

$$F_{\mathrm{c}} = k_{\mathrm{s}} (-y)^{\frac{3}{2}} \left(1 + \frac{3(1 - c_{\mathrm{r}})}{2} \frac{\dot{y}}{\dot{y}_0} \right), \tag{7.28}$$

with coefficient of restitution c_{r}, surface stiffness k_{s}, and initial contact velocity $\dot{y}_0$.

Since the contact event occurs with friction, for the friction model, an approximation of the Coulomb force using a regularized friction coefficient is given by

$$F_{\mathrm{f}} \triangleq \begin{cases} -\mu \left(\frac{\|\dot{x}\|}{10^{-4}} \right) F_{\mathrm{c}} \operatorname{sgn}(\dot{x}), & 0 \leq \frac{\|\dot{x}\|}{10^{-4}} \leq 1, \\ -\mu F_{\mathrm{c}} \operatorname{sgn}(\dot{x}), & 1 < \frac{\|\dot{x}\|}{10^{-4}}, \end{cases} \tag{7.29}$$

where μ is the coefficient of friction [88].

7.2 Control Architecture

The control architecture for the contact phase is shown in Figure 7.2. The controller consists of three components, a feedback linearization controller, a nominal robust controller, and an adaptive controller augmentation using Predictive Cost Adaptive Control. The ascent and descent control follows the method given in [83]. A summary of the control algorithm for the contact phase is given in Algorithm 3.

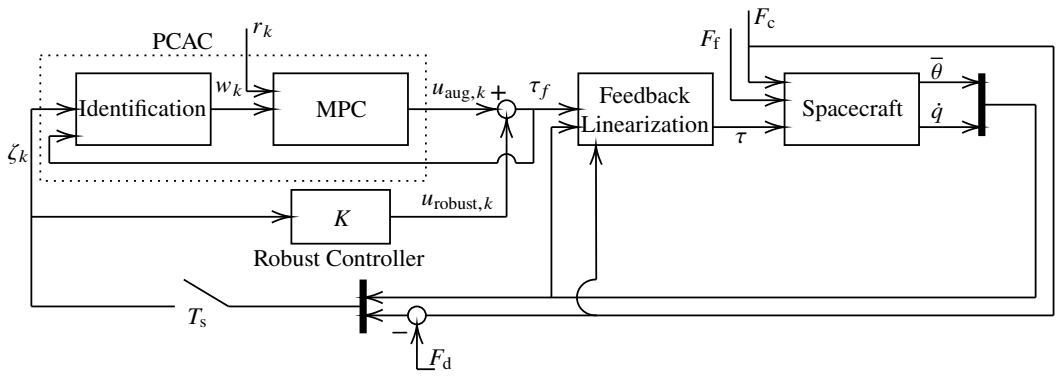

Figure 7.2: Adaptive force control architecture for small celestial body sampling.

7.2.1 Feedback Linearization Controller

The mass and damping matrices can be decomposed into the following 2×2 partitions

$$M(q) = \begin{bmatrix} M_1(\bar{\theta}) & M_2(\bar{\theta}) \\ M_2^{\mathrm{T}}(\bar{\theta}) & m_0 I_2 \end{bmatrix},$$
$$D(q, \dot{q}) = \begin{bmatrix} D_1(\bar{\theta}, \dot{q}) & D_2(\bar{\theta}, \dot{q}) \\ D_2^{\mathrm{T}}(\bar{\theta}, \dot{q}) & 0_2 \end{bmatrix}, \quad \bar{\theta} \triangleq \begin{bmatrix} \theta_1 \\ \theta_2 \end{bmatrix}, \tag{7.30}$$

where $m_0 \triangleq m_{\mathrm{sc}} + m_1 + m_2 + m_{\mathrm{s}}$. Since θ_1, θ_2, $\dot{\theta}_1$, $\dot{\theta}_2$, $\dot{x}$, $\dot{y}$, and F_{c} are assumed to be measured, the following feedback linearization controller can be used

$$\begin{bmatrix} \tau_1 \\ \tau_2 \end{bmatrix} = L^{-1}[(D_1(\bar{\theta}, \dot{q}) - M_1(\bar{\theta}) M_2^{-\mathrm{T}}(\bar{\theta}) D_2^{\mathrm{T}}(\bar{\theta}, \dot{q})) \begin{bmatrix} \dot{\theta}_1 \\ \dot{\theta}_2 \end{bmatrix} + D_2(\bar{\theta}, \dot{q}) \begin{bmatrix} \dot{x} \\ \dot{y} \end{bmatrix}$$
$$+ M_1(\bar{\theta}) M_2^{-\mathrm{T}} \begin{bmatrix} 0 \\ 1 \end{bmatrix} F_{\mathrm{c}} + (M_2(\bar{\theta}) - M_1(\bar{\theta}) M_2^{-\mathrm{T}}(\bar{\theta}) m_0 I_2) \begin{bmatrix} \tau_{1,f} \\ \tau_{2,f} \end{bmatrix}], \tag{7.31}$$

where $\tau_{1,f}$ and $\tau_{2,f}$ are the feedforward portion of the feedback linearization controller to be given by a combination of the robust controller (see subsection 7.2.2) and PCAC (see subsection 7.2.3), and $L \triangleq \begin{bmatrix} 1 & 1 \\ 0 & 1 \end{bmatrix}$. For the feedback linearization controller, we assume that the contact force is of the linear form given by (7.27). Let the desired contact force be F_{d} and define the contact force error by

$$e \triangleq F_{\mathrm{c}} - F_{\mathrm{d}} = -k_{\mathrm{s}} y - c_{\mathrm{s}} \dot{y} - F_{\mathrm{d}}, \tag{7.32}$$

Substituting (7.31) into (7.1) and taking the derivative of (7.32) leads to the following dynamics in state-space form

$$\dot{\zeta} = A(\overline{\theta}, \dot{q})\zeta + B(\overline{\theta})\tau_f + E(\overline{\theta})F_{\mathrm{f}}, \tag{7.33}$$

$$\zeta \triangleq \begin{bmatrix} \dot{\theta}_1 \\ \dot{\theta}_2 \\ \dot{x} \\ \dot{y} \\ e \end{bmatrix}, \quad \tau_f \triangleq \begin{bmatrix} \tau_{1,f} \\ \tau_{2,f} \end{bmatrix} \tag{7.34}$$

$$A(\overline{\theta}, \dot{q}) \triangleq \begin{bmatrix} -M_2^{-\mathrm{T}}(\overline{\theta})D_2^{\mathrm{T}}(\overline{\theta}, \dot{q}) & \begin{matrix} 0 & 0 \\ 0 & 0 \end{matrix} & M_2^{-\mathrm{T}}(\overline{\theta}) \begin{bmatrix} 0 \\ 1 \end{bmatrix} \\ \begin{matrix} 0 & 0 \\ 0 & 0 \\ 0 & 0 \end{matrix} & \begin{matrix} 0 & 0 \\ 0 & 0 \\ 0 & -k_{\mathrm{s}} \end{matrix} & \begin{matrix} 0 \\ 0 \\ 0 \end{matrix} \end{bmatrix}, \tag{7.35}$$

$$B(\overline{\theta}) \triangleq \begin{bmatrix} M_2^{-\mathrm{T}}(\overline{\theta})m_0 I_2 \\ \begin{matrix} 1 & 0 \\ 0 & 1 \\ 0 & -c_{\mathrm{s}} \end{matrix} \end{bmatrix}, \tag{7.36}$$

$$E(\overline{\theta}) \triangleq \begin{bmatrix} M_2^{-\mathrm{T}}(\overline{\theta}) \begin{bmatrix} 1 \\ 0 \end{bmatrix} \\ \xi(\overline{\theta}) \begin{bmatrix} 1 \\ 0 \end{bmatrix} \\ -c_{\mathrm{s}} \begin{bmatrix} 0 & 1 \end{bmatrix} \xi(\overline{\theta}) \begin{bmatrix} 1 \\ 0 \end{bmatrix} \end{bmatrix}, \tag{7.37}$$

$$\xi(\overline{\theta}) \triangleq \left(M_2(\overline{\theta}) - M_1(\overline{\theta})M_2^{-\mathrm{T}}(\overline{\theta})m_0 I_2\right)^{-1} M_1(\overline{\theta})M_2^{-\mathrm{T}}(\overline{\theta}). \tag{7.38}$$

7.2.2 Robust Controller

We seek to regulate the sampler velocity and error states of (7.35)-(7.36). It can be seen that the states $\dot{x}$, $\dot{y}$, and e are decoupled from the sampling arm angular rates $\dot{\theta}_1$ and $\dot{\theta}_2$. Therefore, we focus on the block entries of (7.35)-(7.36) containing the states $\chi = \begin{bmatrix} \dot{x} & \dot{y} & e \end{bmatrix}^{\mathrm{T}}$ where

$$\overline{A} \triangleq \begin{bmatrix} 0 & 0 & 0 \\ 0 & 0 & 0 \\ 0 & -k_\mathrm{s} & 0 \end{bmatrix}, \quad \overline{B} \triangleq \begin{bmatrix} 1 & 0 \\ 0 & 1 \\ 0 & -c_\mathrm{s} \end{bmatrix}. \tag{7.39}$$

The goal is to find a discrete-time controller of the form $\tau_{f,k} = K\chi_k$ that is robust for values of k_s in the range $[k_1, k_2]$ and values of c_s in the range $[c_1, c_2]$. Let $A_{\mathrm{d},i}$ and $B_{\mathrm{d},j}$ be (7.39) discretized using a zero-order hold at the sample rate T_s, and stiffness and damping coefficients k_i and c_j. The control gain K that exponentially stabilizes the system for the range of stiffness and damping coefficients must satisfy the following set of Lyapunov equations

$$\begin{aligned} &(A_{\mathrm{d},i} + B_{\mathrm{d},j}K)Q(A_{\mathrm{d},i} + B_{\mathrm{d},j}K)^\mathrm{T} - e^{-2\lambda T_\mathrm{s}}Q \leq 0 \quad \text{for } i = 1,2 \text{ and } j = 1,2, \\ &Q > 0, \end{aligned} \tag{7.40}$$

where Q is a positive-definite matrix, and λ is a tuning parameter representing the slowest desired exponential decay rate of the closed-loop system for all combinations of stiffness and damping parameters in the range $[k_1, k_2]$, and $[c_1, c_2]$ [89]. Using the Schur complement, defining $Y \triangleq KQ$, and incorporating a slack variable s, (7.40) can be rewritten as a set of LMI constraints in the following optimization problem

$$\begin{aligned} \min_{Q,Y} \quad & s \\ \text{s.t.} \quad & \begin{bmatrix} e^{-2\lambda T_\mathrm{s}}Q & (A_{\mathrm{d},i}Q + B_{\mathrm{d},j}Y) \\ (A_{\mathrm{d},i}Q + B_{\mathrm{d},j}Y)^\mathrm{T} & Q \end{bmatrix} \geq \begin{bmatrix} sI_3 & 0_3 \\ 0_3 & 0_3 \end{bmatrix} \quad \text{for } i = 1,2 \text{ and } j = 1,2, \\ & Q \geq sI_3 \\ & s \geq 0, \end{aligned} \tag{7.41}$$

which can be solved using CVX [90, 91]. The resulting robust controller is then given by $K = YQ^{-1}$.

7.2.3 Predictive Cost Adaptive Control

PCAC combines online identification using recursive least squares with a forgetting factor, and a model predictive controller in two separate steps [32]. For the purposes of augmenting the nominal robust controller for surface sampling, PCAC is modified so that the identification portion attempts to identify the feedback-linearized system without the robust controller instead of the full system model. The identified model is then augmented with the robust controller and sent to the MPC portion of PCAC. The MPC controller outputs a torque augmentation that is added to the torque

command produced by the robust controller.

7.2.3.1 Online Identification

Consider the MIMO input-output model

$$\hat{y}_k = -\sum_{i=1}^{\hat{n}} \hat{F}_i y_{k-i} + \sum_{i=1}^{\hat{n}} \hat{G}_i \tau_{f,k-i}, \tag{7.42}$$

where $k \geq 0$ is the time step, $\hat{n} \geq 1$ is the identification data window, $\hat{F}_i \in \mathbb{R}^{p\times p}$ and $\hat{G}_i \in \mathbb{R}^{p\times m}$ are the estimated model coefficients, and $\tau_{f,k} \in \mathbb{R}^{m\times 1}$, $y_k \in \mathbb{R}^{p\times 1}$, and $\hat{y}_k \in \mathbb{R}^{p\times 1}$ are the inputs, outputs, and predicted outputs at step k, respectively.

To estimate the coefficients $\hat{F}_i$ and $\hat{G}_i$ online, we use RLS with variable-rate forgetting [45]. RLS minimizes the cumulative cost

$$J_k(\hat{w}) = \sum_{i=0}^{k} \frac{\rho_i}{\rho_k} z_i^{\mathrm{T}}(\hat{w}) z_i(\hat{w}) + \frac{1}{\rho_k}(\hat{w} - w_0)^{\mathrm{T}} P_0^{-1}(\hat{w} - w_0), \tag{7.43}$$

where $\rho_k \triangleq \prod_{j=0}^{k} \lambda_j^{-1} \in \mathbb{R}$, $\lambda_k \in (0, 1]$ is the forgetting factor, $P_0 \in \mathbb{R}^{[\hat{n}p(m+p)]\times[\hat{n}p(m+p)]}$ is positive-definite, and $w_0 \in \mathbb{R}^{[\hat{n}p(m+p)]\times 1}$ is the initial estimate of the coefficient vector. The performance variable $z_i(\hat{w}) \in \mathbb{R}^{p\times 1}$ is defined as

$$z_k(\hat{w}) \triangleq y_k + \sum_{i=1}^{\hat{n}} \hat{F}_i y_{k-i} - \sum_{i=1}^{\hat{n}} \hat{G}_i \tau_{f,k-i}, \tag{7.44}$$

where the vector $\hat{w} \in \mathbb{R}^{[\hat{n}p(m+p)]\times 1}$ of coefficients to be estimated is defined by

$$\hat{w} \triangleq \mathrm{vec}\begin{bmatrix} \hat{F}_1 & \cdots & \hat{F}_{\hat{n}} & \hat{G}_1 & \cdots & \hat{G}_{\hat{n}} \end{bmatrix}. \tag{7.45}$$

Defining the regressor matrix $\phi_k \in \mathbb{R}^{p\times[\hat{n}p(m+p)]}$ by

$$\phi_k \triangleq \begin{bmatrix} -y_{k-1}^{\mathrm{T}} & \cdots & -y_{k-\hat{n}}^{\mathrm{T}} & \tau_{f,k-1}^{\mathrm{T}} & \cdots & \tau_{f,k-\hat{n}}^{\mathrm{T}} \end{bmatrix} \otimes I_p, \tag{7.46}$$

the performance variable can be written as

$$z_k(\hat{w}) = y_k - \phi_k \hat{w}. \tag{7.47}$$

The global minimizer $w_{k+1} \triangleq \operatorname{argmin}_{\hat{w}} J_k(\hat{w})$ is computed by RLS as

$$P_{k+1} = \lambda_k^{-1} P_k - \lambda_k^{-1} P_k \phi_k^{\mathrm{T}} (\lambda_k I_p + \phi_k P_k \phi_k^{\mathrm{T}})^{-1} \phi_k P_k \tag{7.48}$$

$$w_{k+1} = w_k + P_{k+1} \phi_k^{\mathrm{T}} (y_k - \phi_k \hat{w}), \tag{7.49}$$

where $w_{k+1} = \operatorname{vec} \begin{bmatrix} \hat{F}_{1,k+1} & \cdots & \hat{F}_{\hat{n},k+1} & \hat{G}_{1,k+1} & \cdots & \hat{G}_{\hat{n},k+1} \end{bmatrix}$.

The VRF factor λ_k is developed in [49] and given by

$$\lambda_k = \frac{1}{1 + \eta g(z_{k-\tau_{\mathrm{d}}}, \ldots, z_k) \mathbf{1}[g(z_{k-\tau_{\mathrm{d}}}, \ldots, z_k)]}, \tag{7.50}$$

where $\mathbf{1} : \mathbb{R} \to \{0, 1\}$ is the unit step function, and

$$g(z_{k-\tau_d}, \ldots, z_k) \triangleq \sqrt{\frac{\tau_{\mathrm{n}}}{\tau_{\mathrm{d}}} \frac{\operatorname{tr}\left(\Sigma_{\tau_{\mathrm{n}}}(z_{k-\tau_{\mathrm{n}}}, \ldots, z_k) \Sigma_{\tau_{\mathrm{d}}}(z_{k-\tau_{\mathrm{d}}}, \ldots, z_k)^{-1}\right)}{c}} - \sqrt{f}, \tag{7.51}$$

where $\eta > 0$ and $p \leq \tau_{\mathrm{n}} < \tau_{\mathrm{d}}$ represent numerator and denominator window lengths, respectively. In (7.51), $\Sigma_{\tau_{\mathrm{n}}}$ and $\Sigma_{\tau_{\mathrm{d}}} \in \mathbb{R}^{p \times p}$ are the sample variances of the respective window lengths, c is a constant given by

$$\begin{aligned} a &\triangleq \frac{(\tau_{\mathrm{n}} + \tau_{\mathrm{d}} - p - 1)(\tau_{\mathrm{d}} - 1)}{(\tau_{\mathrm{d}} - p - 3)(\tau_{\mathrm{d}} - p)}, \; b \triangleq 4 + \frac{(p\tau_{\mathrm{n}} + 2)}{(a - 1)}, \\ c &\triangleq \frac{p\tau_{\mathrm{n}}(b - 2)}{b(\tau_{\mathrm{d}} - p - 1)}, \end{aligned} \tag{7.52}$$

$f \triangleq F^{-1}_{p\tau_{\mathrm{n}}, b}(1 - \alpha)$ is a thresholding constant, where $F^{-1}_{p\tau_{\mathrm{n}}, b}(x)$ is the inverse cumulative distribution function of the F-distribution with degrees of freedom $p\tau_{\mathrm{n}}$ and b, and α is the significance level [55].

For model predictive control, the input-output model (7.42) is written as the BOCF state-space realization augmented by the robust controller

$$\begin{aligned} x_{1|k} &\triangleq \hat{A}_k \hat{x}_k + \hat{B}_k u_{\mathrm{aug},k}, \\ y_k &= \hat{C} \hat{x}_k, \end{aligned} \tag{7.53}$$

where $x_{1|k} \in \mathbb{R}^{\hat{n}p}$ is the one-step predicted state, $\hat{x}_k \triangleq \begin{bmatrix} \hat{x}_{1,k}^{\mathrm{T}} & \cdots & \hat{x}_{\hat{n},k}^{\mathrm{T}} \end{bmatrix}^{\mathrm{T}} \in \mathbb{R}^{\hat{n}p}$ is the state estimate,

and

$$\hat{x}_{1,k} \triangleq y_k, \tag{7.54}$$

$$\hat{x}_{i,k} \triangleq -\sum_{j=1}^{\hat{n}-i+1} \hat{F}_{i+j-1,k+1} y_{k-j} + \sum_{j=1}^{\hat{n}-i+1} \hat{G}_{i+j-1,k+1} \tau_{f,k-j}, \quad i = 2, \ldots, \hat{n} \tag{7.55}$$

$$\hat{A}_k \triangleq \begin{bmatrix} -\hat{F}_{1,k+1} & I_p & \cdots & \cdots & 0_{p\times p} \\ \vdots & 0_{p\times p} & \ddots & & \vdots \\ \vdots & \vdots & \ddots & \ddots & 0_{p\times p} \\ \vdots & \vdots & & \ddots & I_p \\ -\hat{F}_{\hat{n},k+1} & 0_{p\times p} & \cdots & \cdots & 0_{p\times p} \end{bmatrix} + \begin{bmatrix} \hat{G}_{1,k+1} \\ \hat{G}_{2,k+1} \\ \vdots \\ \hat{G}_{\hat{n},k+1} \end{bmatrix} K, \tag{7.56}$$

$$\hat{B}_k \triangleq \begin{bmatrix} \hat{G}_{1,k+1} \\ \hat{G}_{2,k+1} \\ \vdots \\ \hat{G}_{\hat{n},k+1} \end{bmatrix}, \ \hat{C} \triangleq \begin{bmatrix} I_p & 0_{p\times p} & \cdots & 0_{p\times p} \end{bmatrix}, \tag{7.57}$$

7.2.3.2 Model Predictive Control

The ℓ-step predicted output of (7.53) for a sequence of ℓ future controls is given by

$$Y_{1|k,l} = \hat{\Gamma}_{k,\ell} x_{1|k} + \hat{T}_{k,\ell} U_{1|k,\ell}, \tag{7.58}$$

where

$$Y_{1|k,\ell} \triangleq \begin{bmatrix} y_{1|k} \\ \vdots \\ y_{\ell|k} \end{bmatrix} \in \mathbb{R}^{\ell p}, \quad U_{1|k,\ell} \triangleq \begin{bmatrix} u_{1|k} \\ \vdots \\ u_{\ell|k} \end{bmatrix} \in \mathbb{R}^{\ell m}, \tag{7.59}$$

and $\hat{\Gamma}_{k,\ell} \in \mathbb{R}^{\ell p \times \hat{n} p}$ and $\hat{T}_{k,\ell} \in \mathbb{R}^{\ell p \times \ell m}$ are

$$\hat{\Gamma}_{k,\ell} \triangleq \begin{bmatrix} \hat{C} \\ \hat{C}\hat{A}_k \\ \vdots \\ \hat{C}\hat{A}_k^{\ell-1} \end{bmatrix}, \quad \hat{T}_{k,\ell} \triangleq \begin{bmatrix} 0_{p\times m} & \cdots & \cdots & \cdots & 0_{p\times m} \\ \hat{H}_{k,1} & 0_{p\times m} & \cdots & \cdots & 0_{p\times m} \\ \hat{H}_{k,2} & \hat{H}_{k,1} & \ddots & \cdots & 0_{p\times m} \\ \vdots & \vdots & \ddots & \ddots & \vdots \\ \hat{H}_{k,\ell-1} & \hat{H}_{k,\ell-2} & \cdots & \hat{H}_{k,1} & 0_{p\times m} \end{bmatrix},$$

where $\hat{H}_{k,i} \in \mathbb{R}^{p\times m}$ is defined by $\hat{H}_{k,i} \triangleq \hat{C}\hat{A}_k^{i-1}\hat{B}_k$.

Let $\mathcal{R}_{k,\ell} \triangleq \begin{bmatrix} r_{k+1}^{\mathrm{T}} \cdots r_{k+\ell}^{\mathrm{T}} \end{bmatrix}^{\mathrm{T}} \in \mathbb{R}^{\ell p_{\mathrm{t}}}$ be the vector of ℓ future commands, $C_{\mathrm{t},\ell} \triangleq I_\ell \otimes C_{\mathrm{t}} \in \mathbb{R}^{\ell p_{\mathrm{t}} \times \ell p}$, where $C_{\mathrm{t}} y_{i|k}$ creates the tracking outputs from $y_{i|k}$, let $Y_{\mathrm{t},1|k,\ell} \triangleq C_{\mathrm{t},\ell} Y_{1|k,\ell}$ be the ℓ-step predicted tracking output, and define $\Delta U_{1|k,\ell} \in \mathbb{R}^{\ell m \times 1}$ as

$$\Delta U_{1|k,\ell} \triangleq \begin{bmatrix} (u_{1|k} - u_k)^{\mathrm{T}} & \cdots & (u_{\ell|k} - u_{\ell-1|k})^{\mathrm{T}} \end{bmatrix}^{\mathrm{T}}. \tag{7.60}$$

The receding horizon optimization problem is then given by

$$\begin{aligned} \min_{U_{1|k,\ell}} \quad & \left(Y_{\mathrm{t},1|k,\ell} - \mathcal{R}_{k,\ell}\right)^{\mathrm{T}} Q \left(Y_{\mathrm{t},1|k,\ell} - \mathcal{R}_{k,\ell}\right) + \Delta U_{1|k,\ell}^{\mathrm{T}} R \Delta U_{1|k,\ell} \\ \text{s.t.} \quad & U_{\min} \leq U_{1|k,\ell} \leq U_{\max} \\ & \Delta U_{\min} \leq \Delta U_{1|k,\ell} \leq \Delta U_{\max}, \end{aligned} \tag{7.61}$$

where $Q \in \mathbb{R}^{\ell p_{\mathrm{t}} \times \ell p_{\mathrm{t}}}$ is the positive-definite tracking weight, $R \in \mathbb{R}^{\ell m \times \ell m}$ is the positive-definite control move-size weight, $U_{\min} \triangleq 1_{\ell \times 1} \otimes u_{\min} \in \mathbb{R}^{\ell m}$, $U_{\max} \triangleq 1_{\ell \times 1} \otimes u_{\max} \in \mathbb{R}^{\ell m}$, $\Delta U_{\min} \triangleq 1_{\ell \times 1} \otimes \Delta u_{\min} \in \mathbb{R}^{\ell m}$, and $\Delta U_{\max} \triangleq 1_{\ell \times 1} \otimes \Delta u_{\max} \in \mathbb{R}^{\ell m}$. The first entry of $U_{1|k,\ell}$ is then used as the control augmentation $u_{\mathrm{aug},k}$.

Algorithm 2 PCAC Identification For Adaptive Force Control

Initialize: $\hat{w}_0 \in \mathbb{R}^{[\hat{n}p(m+p)]\times 1}$, $P_0 \in \mathbb{R}^{[\hat{n}p(m+p)]\times[\hat{n}p(m+p)]}$ positive-definite, $\tau_{\mathrm{d}} > \tau_{\mathrm{n}} \geq p$, $\eta > 0$, $\alpha > 0$, $k = 0$, and a buffer of $\tau_{\mathrm{d}} + 1$ previous performance variables initialized as 0

function PCAC_ID($y_k, \tau_{f,k}$)

$z_k \leftarrow y_k - \phi_k \hat{w}_k$

Add z_k to performance variable buffer and remove oldest entry

Compute sample covariance matrices $\Sigma_{\tau_{\mathrm{n}}} \in \mathbb{R}^{p \times p}$, $\Sigma_{\tau_{\mathrm{d}}} \in \mathbb{R}^{p \times p}$ from previous $\tau_{\mathrm{n}}+1$ and $\tau_{\mathrm{d}}+1$ errors from buffer

if $k \geq \tau_{\mathrm{d}} + 1$ **then**

Compute a, b, and c using (5.6)

$g \leftarrow$ (5.7)

else

$g \leftarrow 0$

end if

$\beta_k \leftarrow 1 + \eta g \mathbf{1}[g]$

$L_k \leftarrow \beta_k P_k$

$w_{k+1} \leftarrow w_k + P_{k+1} \phi_k^{\mathrm{T}} (y_k - \phi_k w_k)$

$P_{k+1} \leftarrow L_k - L_k \phi_k^{\mathrm{T}} (I_p + \phi_k L_k \phi_k^{\mathrm{T}})^{-1} \phi_k L_k$

$\phi_{k+1} \leftarrow$ Update regressor ϕ_k with current measurement and input

end function

Algorithm 3 Adaptive Force Control Augmentation

Initialize: $p = 5$, $m = 2$, Sample rate T_s, Solve (7.41) to get K, $\tau_{f,0} = 0_{m\times 1}$, $k = 0$

while In contact phase **do**

Measure $\theta_1, \theta_2, \zeta_k = \begin{bmatrix}\dot{\theta}_1 & \dot{\theta}_2 & \dot{x} & \dot{y} & e\end{bmatrix}^{\mathrm{T}} \in \mathbb{R}^{p\times 1}$, and $\chi_k = \begin{bmatrix}\dot{x} & \dot{y} & e\end{bmatrix}^{\mathrm{T}} \in \mathbb{R}^{p-2\times 1}$

Start Robust Controller

$u_{\text{robust},k} \leftarrow K\chi_k$

End Robust Controller

Start PCAC Identification

$y_k \leftarrow \zeta_k$ State measurement

$w_{k+1} \leftarrow \text{PCAC\_ID}(y_k, \tau_{f,k})$

End PCAC Identification

$\hat{x}_k \leftarrow w_{k+1}, y_k$ from (7.54)-(7.55)

$K \leftarrow \begin{bmatrix}0_2 & K\end{bmatrix}$

$\hat{A}_k, \hat{B}_k, \hat{C} \leftarrow w_{k+1}, K$ from (7.56)-(7.57)

Start PCAC MPC

$U_{1|k,\ell} \leftarrow$ Solve (7.61)

$u_{\text{aug},k} \leftarrow \begin{bmatrix}I_m & 0_{m\times(\ell-1)m}\end{bmatrix} U_{1|k,\ell}$

End PCAC MPC

$\tau_{f,k} \leftarrow u_{\text{robust},k} + u_{\text{aug},k}$

Start Feedback Linearization

$\tau_f \leftarrow \tau_{f,k}$

$\begin{bmatrix}\tau_1 & \tau_2\end{bmatrix}^{\mathrm{T}} \leftarrow \tau_f$ from (7.31)

End Feedback Linearization

$k \leftarrow k + 1$

end while

7.3 Numerical Examples

To demonstrate the advantage of the adaptive augmentation method we compare the algorithm to the nominal robust controller for a variety of surface properties including linear and nonlinear contact models. We also demonstrate a double sampling maneuver where the sampler mass increases by an unknown amount after obtaining a surface sample from the first maneuver before descending onto the surface again to obtain additional material. In these examples, the spacecraft in Figure 7.1 descends onto the surface at a speed of $0.1\,\frac{\mathrm{m}}{\mathrm{s}}$ starting from a height of 0.2 m. There are seven sensors measuring θ_1, θ_2, $\dot{\theta}_1$, $\dot{\theta}_2$, $\dot{x}$, $\dot{y}$, and F_c. Once contact is made, the controller attempts to regulate the sampler's contact force to $F_\mathrm{d} = 25\,\mathrm{N}$ and its x and y velocity to 0 before departing the surface after 2 s.

The spacecraft parameters are $m_\mathrm{sc} = 420\,\mathrm{kg}$, $m_1 = m_2 = m_\mathrm{s} = 1\,\mathrm{kg}$, $L_1 = L_2 = 2\,\mathrm{m}$, $R_1 = R_2 = 1\,\mathrm{m}$, $\bar{I}_1 = \bar{I}_2 = \frac{1}{3}\,\frac{\mathrm{kg}}{\mathrm{m}^2}$, $\theta_{1,0} = \frac{\pi}{4}$, and $\theta_{2,0} = \frac{\pi}{2}$. The surface coefficient of friction is taken to be $\mu = 0.5$. The robust controller parameters were taken to be $\lambda = 0.05$, $k_1 = 300\,\frac{\mathrm{N}}{\mathrm{m}}$, $k_2 = 2.7 \times 10^5\,\frac{\mathrm{N}}{\mathrm{m}}$, $c_1 = 0.35\,\frac{\mathrm{N\,s}}{\mathrm{m}}$, and $c_2 = 10^3\,\frac{\mathrm{N\,s}}{\mathrm{m}}$. PCAC is initialized with $p = 5$, $m = 2$, $\hat{n} = 1$, $P_0 = 10 I_{35}$, $\eta = 0.1$, $\tau_\mathrm{n} = 40$, $\tau_\mathrm{d} = 200$, $\alpha = 0.001$, $\ell = 50$, $Q = I_\ell \otimes \mathrm{diag}(1000, 100, 1)$, $R = 1 I_{\ell m}$, $C_\mathrm{t} = \begin{bmatrix} 0_{3\times 2} & I_3 \end{bmatrix}$, $u_\mathrm{max} = -u_\mathrm{min} = 100$, and $\mathcal{R}_{k,\ell} = 1_{3\times\ell} \otimes \begin{bmatrix} 0 & 0 & 0 \end{bmatrix}^\mathrm{T}$. The initial PCAC model coefficients w_0 are initialized to match the zero-order-hold discretized model of (7.35)-(7.36), with the linear surface contact model $k_\mathrm{s} = 100\,\frac{\mathrm{N}}{\mathrm{m}}$ and $c_\mathrm{s} = 10^3\,\frac{\mathrm{N\,s}}{\mathrm{m}}$, and $\overline{\theta}$, $\dot{q}$ being set to their respective values at contact. This makes w_0 a 35 parameter vector. The controller runs in a sample-data feedback loop at 2 kHz.

7.3.1 Linear Contact Model

Assuming the surface has the linear Kelvin-Voigt contact model (7.27) we compare the performance of the robust controller and augmented robust controller with PCAC for stiffness coefficients between $300\,\frac{\mathrm{N}}{\mathrm{m}}$ and $2.7 \times 10^5\,\frac{\mathrm{N}}{\mathrm{m}}$, and damping coefficients $0.35\,\frac{\mathrm{N\,s}}{\mathrm{m}}$ and $10^3\,\frac{\mathrm{N\,s}}{\mathrm{m}}$. Figure 7.3 shows the median contact force over the 2 second contact period over the range of surface properties. Notice that the nominal robust controller has difficulty reaching the desired contact force for low surface stiffness coefficients while the augmented controller consistently reaches the desired contact force for all tested surface properties. Figure 7.4 shows the contact force, sampler velocity, actuator torques, and PCAC model coefficients for the surface properties $k_\mathrm{s} = 2 \times 10^5\,\frac{\mathrm{N}}{\mathrm{m}}$ and $c_\mathrm{s} = 5\,\frac{\mathrm{N\,s}}{\mathrm{m}}$. Notice that the PCAC augmented controller quickly reaches the desired contact force while the nominal robust controller on its own takes most of the 2 second contact period to reach the desired contact force of 25 N.

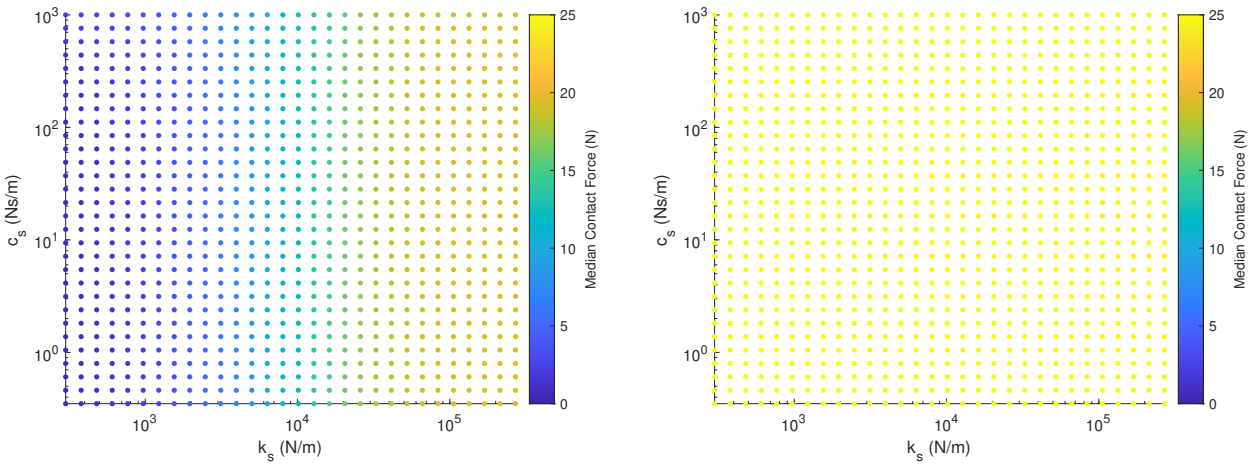

(a) Robust controller

(b) PCAC augmented controller

Figure 7.3: Median contact force for various surface stiffness k_s and damping c_s values using the linear Kelvin-Voigt contact model (7.27).

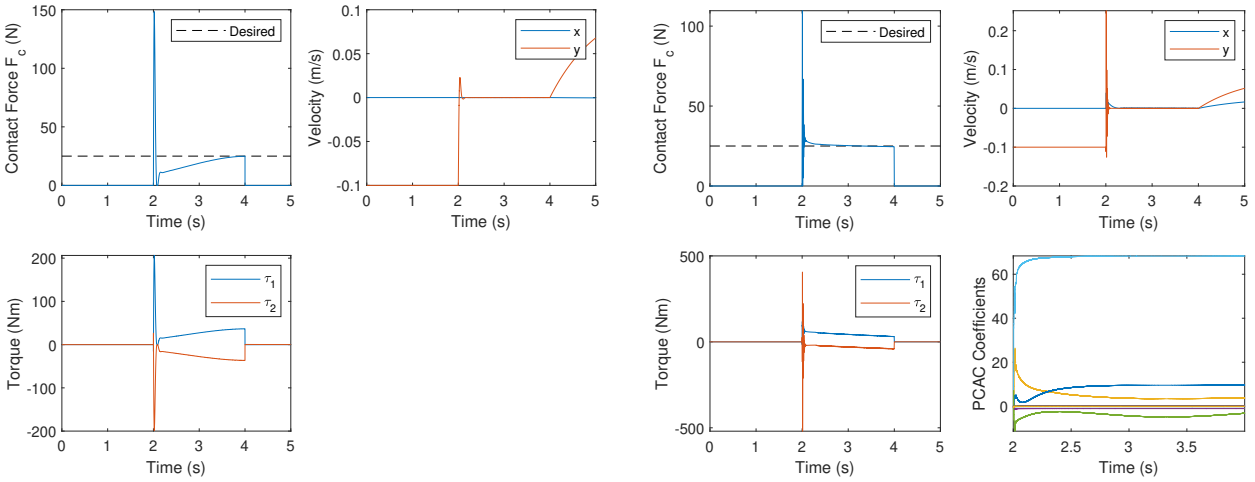

(a) Robust controller

(b) PCAC augmented controller

Figure 7.4: Contact force, sampler velocity, actuator torques, and PCAC model coefficients for the linear contact model (7.27) with $k_s = 2 \times 10^5 \frac{\text{N}}{\text{m}}$ and $c_s = 5 \frac{\text{Ns}}{\text{m}}$.

7.3.2 Nonlinear Contact Model

Assuming the surface has the nonlinear Hunt-Crossley contact model (7.28) we compare the performance of the robust controller and augmented robust controller with PCAC for stiffness coefficients between $300 \frac{\text{N}}{\text{m}}$ and $2.7 \times 10^5 \frac{\text{N}}{\text{m}}$, and coefficient of restitution between 0.1 and 1. Figure 7.5 shows the median contact force over the 2 second contact period over the range of surface

properties. Notice that the nominal robust controller's median contact force has difficulty reaching even half of the desired 25 N while the augmented controller consistently reaches the desired contact force for all tested surface properties except for situations where there is low stiffness combined with a high coefficient of restitution. Figure 7.6 shows the contact force, sampler velocity, actuator torques, and PCAC model coefficients for the surface properties $k_s = 2\times10^5 \frac{N}{m}$ and $c_r = 0.9$. Notice that the PCAC augmented controller quickly reaches the desired contact force while the nominal robust controller never does.

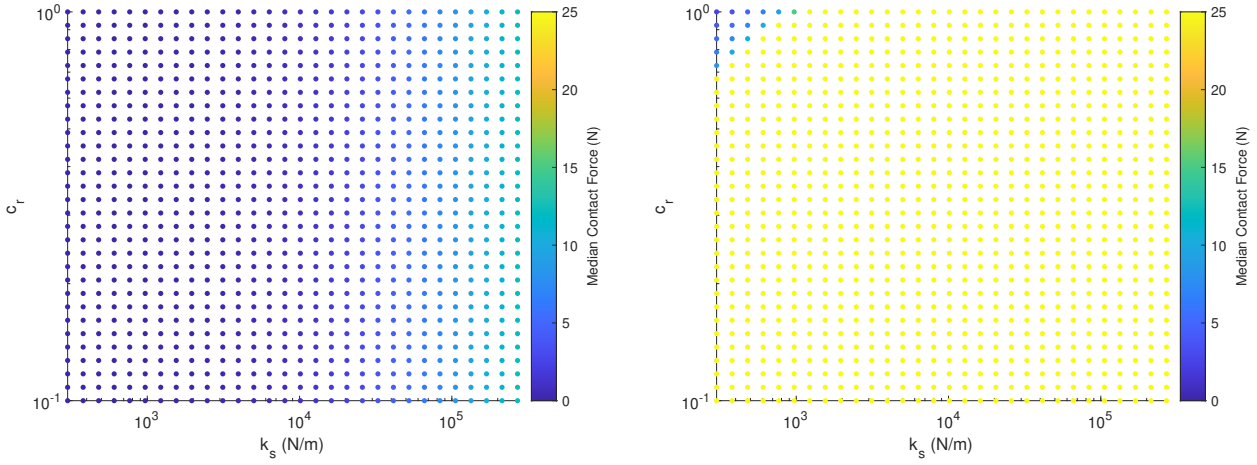

(a) Robust controller

(b) PCAC augmented controller

Figure 7.5: Median contact force for various surface stiffness k_s and damping c_s values using the nonlinear Hunt-Crossley contact model (7.28).

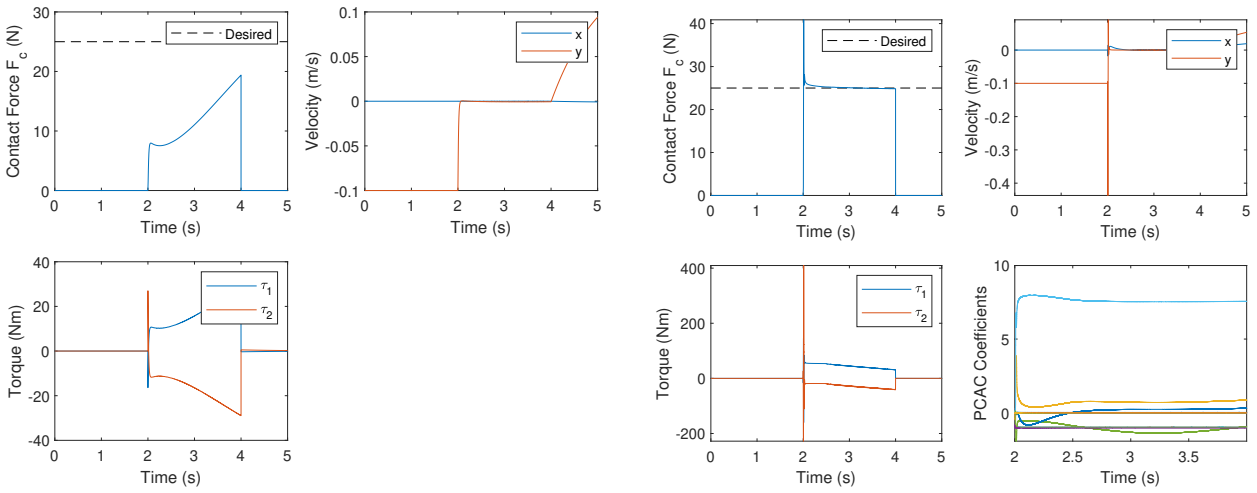

(a) Robust controller

(b) PCAC augmented controller

Figure 7.6: Contact force, sampler velocity, actuator torques, and PCAC model coefficients for the nonlinear contact model (7.28) with $k_s = 2 \times 10^5 \frac{N}{m}$ and $c_r = 0.9$.

7.3.3 Double Sampling Maneuver with Linear Contact Model

We now consider a double sampling maneuver where after descending onto the surface and collecting a sample, the spacecraft then descends again onto a different region of the celestial body to collect additional material. The amount of material collected on the first maneuver is chosen to be 0.5 kg and is unknown to the spacecraft. Assuming the surface has the linear Kelvin-Voigt contact model (7.27), the surface on the first maneuver has properties $k_s = 2 \times 10^5 \frac{N}{m}$ and $c_s = 5 \frac{Ns}{m}$, and the surface on the second maneuver has $k_s = 200 \frac{N}{m}$ and $c_s = 500 \frac{Ns}{m}$. Figure 7.7 shows that the desired contact force is reached for both maneuvers. Notice that on contact with the new surface at 8 s the RLS VRF factor λ_k automatically decreases, enabling forgetting of the old surface properties and causing an increase in the trace of the RLS covariance $\text{tr}(P_k)$ to allow for fast identification of a new surface contact model.

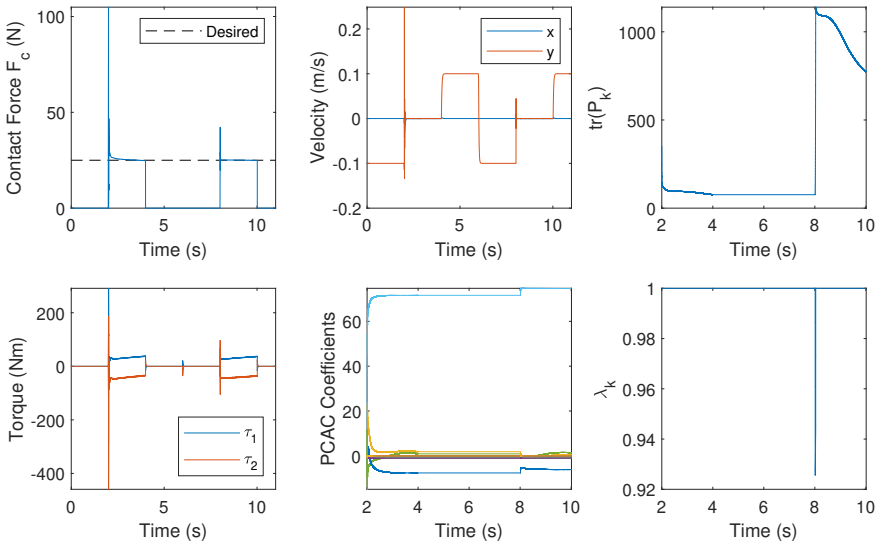

Figure 7.7: Contact force, sampler velocity, actuator torques, and PCAC model coefficients for a double sampling maneuver with the linear contact model (7.27) with $k_s = 2 \times 10^5 \frac{N}{m}$ and $c_s = 5 \frac{Ns}{m}$ for the first maneuver and $k_s = 200 \frac{N}{m}$ and $c_s = 500 \frac{Ns}{m}$ for the second maneuver. Note that the forgetting factor drops immediately when the sampler contacts a different surface.

7.3.4 Double Sampling Maneuver with Nonlinear Contact Model

For the double sampling maneuver, assuming the surface has the nonlinear Hunt-Crossley contact model (7.28), the surface on the first maneuver has properties $k_s = 2 \times 10^5 \frac{N}{m}$ and $c_r = 0.9$, and the surface on the second maneuver has $k_s = 300 \frac{N}{m}$ and $c_r = 0.2$. Figure 7.8 shows that the desired contact force is reached for both maneuvers. Notice that on contact with the new surface at 8 s the RLS VRF factor λ_k automatically decreases, enabling forgetting of the old surface properties and causing an increase in the trace of the RLS covariance $\text{tr}(P_k)$ to allow for fast identification of a new surface contact model.

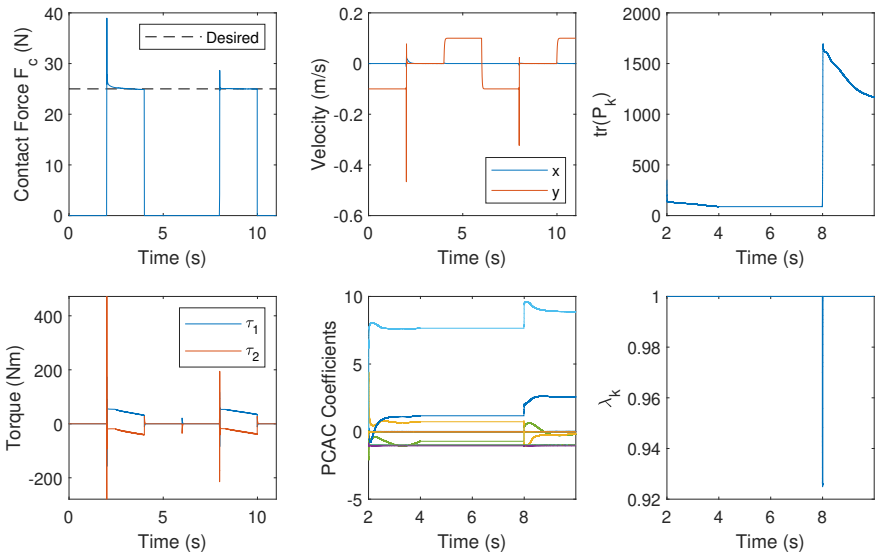

Figure 7.8: Contact force, sampler velocity, actuator torques, and PCAC model coefficients for a double sampling maneuver with the nonlinear contact model (7.28) with $k_s = 2 \times 10^5 \frac{\text{N}}{\text{m}}$ and $c_r = 0.9$ for the first maneuver, and $k_s = 300 \frac{\text{N}}{\text{m}}$ and $c_r = 0.2$ for the second maneuver.

7.4 Conclusions

This chapter developed and investigated the performance of an adaptive force control augmentation algorithm for spacecraft sampling maneuvers on small celestial bodies. The algorithm consisted of a nominal robust controller with an adaptive augmentation using PCAC combined with feedback linearization to maintain a desired contact force during the sampling maneuver. PCAC uses output-feedback model predictive control without an estimator and with concurrent online identification. Both linear and nonlinear contact models were used to investigate the controller's performance under various surface properties. Additionally, a double sampling maneuver was investigated where the spacecraft collected an unknown amount of material from an initial maneuver before ascending and descending and then sampling from a different region of the celestial body with different surface properties. The controller was shown to reach the desired contact force over a wide range of surface properties and outperformed the nominal robust controller in all cases. For the double sampling maneuver, PCAC was able to identify a new model of the surface and successfully adjust the control input to reach the desired contact force on the second surface.

CHAPTER 8

Conclusions and Future Work

8.1 Conclusions

This dissertation presented and applied retrospective cost adaptive control (RCAC) and predictive cost adaptive control (PCAC) to problems representative of spacecraft disturbance rejection and asteroid sample gathering scenarios. It was demonstrated that a dereverberated transfer function (DTF) can be used as the modeling information for RCAC for disturbance rejection of lightly damped structures and two methods for constructing a dereverberated transfer function (DTF) were presented. Additionally, a new adaptive control method, retrospective cost model reference adaptive control (RC-MRAC), and a new variable-rate forgetting (VRF) factor for recursive least squares (RLS) using the F-test were developed.

First, two methods for identifying DTFs were formulated. A DTF that captures the phase and magnitude trend but not the detailed peaks and notches of the system was used as the target model for RCAC. It was shown numerically and in a lab experiment that RCAC with a DTF target model could be used for harmonic disturbance rejection of lightly damped systems where the frequency, amplitude, and phase of the harmonic disturbances are unknown. In addition, it was demonstrated that RCAC with a DTF target model was robust to errors in the damping ratio of the model used to construct the DTF. For the lab experiment, a gradient-based version of RCAC was developed and implemented at 8-kHz for a noise rejection problem. This variant of RCAC could be implemented for real-time control of large space structures such as telescopes.

Next, RC-MRAC was developed and compared to Elliot's adaptive pole placement control (APPC). If the leading numerator coefficient, relative degree, system order, and nonminimum-phase (NMP) zeros are known then RC-MRAC is able to place the closed-poles of the system such that they match the closed-loop poles of a desired reference model. RC-MRAC was then demonstrated to require little persistency in the reference command for accurate model following. With a slight modification, RC-MRAC was shown to be able to reject harmonic disturbances which is a vital aspect for the control of systems such as robotic arms. For minimum-phase systems,

RC-MRAC outperforms APPC without the need for persistency, and NMP systems, RC-MRAC performs better than APPC at lower persistency levels at the price of knowledge of the NMP zeros and slower convergence times.

Next, to improve the performance of RLS for tracking time-varying parameters, a new VRF factor for RLS which uses the F-test was developed and investigated. The new method uses a ratio of covariances of a short and long horizon of one-step prediction errors combined with the F-test to determine whether the underlying system parameters have changed. To deal with MIMO systems, a multivariate approximation of the F-test was used. Compared to the standard constant-rate forgetting and the original VRF factor used in PCAC, the new F-test method outperformed the former methods in system identification scenarios with noiseless and noisy measurements, and nonpersistently exciting inputs. For noisy measurements, the *F-test* prevented forgetting from occurring due to noise, and for nonpersistently exciting inputs, the method kept RLS from forgetting when it was not needed, which kept the eigenvalues of the RLS covariance matrix bounded and stable.

Next, the performance of PCAC was investigated for disturbance rejection of large flexible structures. Large structures such as those present in space telescopes are subject to unknown disturbances which excite the lightly damped modes in the structure. These excitations degrade the line-of-sight performance of the space telescope and would need to be suppressed to maximize imaging performance. To demonstrate the performance of PCAC for a line-of-sight disturbance rejection scenario, a model of a large truss structure was developed and was subject to unknown harmonic and broadband disturbances. Additionally, the effects of aliasing and modal folding were considered. PCAC was demonstrated to suppress the disturbances in all cases without a priori knowledge of the dynamics or disturbance spectra.

Finally, PCAC was used in a spacecraft surface sampling scenario of a small celestial body. PCAC augmented a nominal controller which consisted of a feedback linearization controller combined with a robust controller developed through a set of linear matrix inequalities (LMIs). To model the surface of the celestial body, both linear and nonlinear spring-damping contact models were investigated. The augmented controller reached the desired surface contact force over a wide range of tested surface properties and outperformed the nominal controller in all cases. In order to demonstrate the F-test forgetting method, a double sampling maneuver was investigated where the spacecraft collected an unknown amount of material from an initial maneuver before ascending, descending, then sampling from a different region of the celestial body with different surface properties. PCAC with F-test forgetting enabled forgetting on contact with the new surface and quickly identified a new model and adjusted the contact force to successfully grab a new sample.

8.2 Future Work

Future work will extend RC-MRAC to the MIMO case following a similar development for RCAC given in [23]. Additionally, a key challenge is the development of stability results for RC-MRAC. Given the development of stability results for similar algorithms [19, 66], a stability result for RC-MRAC will closely follow established arguments.

For the VRF factor using the F-test, the F-test is known to be sensitive to non-normality of the data used to compute the sample variances. Situations such as nonwhite and heavy-tailed noise sources will need to be investigated in order to determine the extent of this sensitivity for variable-rate forgetting. Additionally, it is preferred to use a method of computing sample variances such that no buffer of past errors is needed for memory and computational performance reasons. Incorporating a weighted moving average of errors with a weighted sum of squares of errors as in [92] with a modified version of the F-test would allow faster computation of the forgetting factor.

The controller provided by MPC and PCAC is the result of a receding-horizon optimization and is not necessarily a linear time-invariant control law. For structural control problems, the Bode sensitivity integral constraints are an important factor in achieving the best disturbance rejection performance. The relevance of these constraints to vibration suppression is considered in [10] for SISO systems for the case of linear time-invariant controllers. It is interesting to determine the extent to which the Bode sensitivity integral constraints [93] apply to the "loop transfer function." for time-variant control law. Additionally, analysis of PCAC via Bode integrals in the MIMO case could be used to guide sensor/actuator placement.

During the first few steps of PCAC, the controller tends to bang on control constraints, and exceed desired measurement constraints while attempting to identify a sufficient model. To prevent this from occurring, the RLS covariance matrix P_k could be used in the MPC portion of RCAC to incorporate more "cautious" control action when model uncertainty is high. Additionally, an approximation of the RLS covariance matrix update can be included as a constraint in the MPC portion to help guide control inputs to those that would provide greater excitation. This would allow PCAC to incorporate "dual" control action which could improve model identification speed during the initial steps and after system changes.

For the celestial body surface sampling problem, when contact is first made with the surface, there is an initially large transient force exerted on the sampler. This can be mitigated using a combination of the proposed control algorithm and passive damping of the sampling arm. The inclusion of passive damping lessens the total required control input. Additionally, investigation of more accurate surface contact models is of interest. Complementarity contact models and high-fidelity, particle-based soil-contact models are possible avenues for improving the simulation accuracy of the sampling maneuver.

BIBLIOGRAPHY

[1] C. R. Fuller and A. H. von Flotow, "Active control of sound and vibration," *IEEE Contr. Sys. Mag.*, vol. 15, no. 6, pp. 9–19, 1995.

[2] A. Preumont, *Vibration Control of Active Structures: An Introduction*, 4th ed. Springer, 2018.

[3] R. L. Clark, W. R. Saunders, and G. P. Gibbs, *Adaptive Structures: Dynamics and Control*. Wiley, 2001.

[4] Z. R. Wani, M. Tantray, E. Noroozinejad Farsangi, N. Nikitas, M. Noori, B. Samali, and T. Yang, "A critical review on control strategies for structural vibration control," *Annual Reviews in Control*, vol. 54, pp. 103–124, 2022.

[5] P. A. Nelson and S. J. Elliot, *Active Control of Sound*. Academic Press, 1992.

[6] S. M. Kuo and D. R. Morgan, *Active Noise Control Systems: Algorithms and DSP Implementations*. Wiley, 1995.

[7] D. Abramovitch and G. Franklin, "A brief history of disk drive control," *IEEE Control Systems Magazine*, vol. 22, no. 3, pp. 28–42, 2002.

[8] M. Balas, "Trends in large space structure control theory: fondest hopes, wildest dreams," *IEEE Trans. Autom. Contr.*, vol. 27, no. 3, pp. 522–535, 1982.

[9] R. Curtain and K. Morris, "Transfer functions of distributed parameter systems: A tutorial," *Automatica*, vol. 45, no. 5, pp. 1101–1116, 2009.

[10] J. Hong and D. S. Bernstein, "Bode Integral Constraints, Colocation, and Spillover in Active Noise and Vibration Control," *IEEE Trans. Contr. Sys. Tech.*, vol. 6, pp. 111–120, 1998.

[11] A. May, B. Sutter, T. Linn, B. Bierhaus, K. Berry, and R. Mink, "Osiris-rex touch-and-go (tag) mission design for asteroid sample collection," *Int. Astronaut. Congr.*, vol. 65, pp. 1–11, 2014.

[12] T. Ajluni, D. Everett, T. Linn, R. Mink, W. Willcockson, and J. Wood, "Osiris-rex, returning the asteroid sample," in *IEEE Aerosp. Conf.*, 2015, pp. 1–15.

[13] M. B. Quadrelli, P. Backes, W. K. Wilkie, L. Giersch, U. Quijano, J. Keim, D. Scharf, R. Mukherjee, S. C. Bradford, and M. McKee, "Investigation of phase transition-based tethered systems for small body sample capture," *Acta Astronaut.*, vol. 68, no. 7, pp. 947–973, 2011.

[14] M. B. Quadrelli, M. Ono, and A. Jain, "Modeling of active tether system concepts for planetary exploration," *Acta Astronaut.*, vol. 138, pp. 512–529, 2017.

[15] J. Biele, S. Ulamec, M. Maibaum, R. Roll, and et al., "The landing(s) of philae and inferences about comet surface mechanical properties," *Science*, vol. 349, no. 6247, pp. 1–6, 2015.

[16] P. A. Ioannou and J. Sun, *Robust Adaptive Control*. Prentice-Hall, 1996.

[17] G. C. Goodwin and K. S. Sin, *Adaptive Filtering, Prediction, and Control*. Prentice Hall, 1984.

[18] K. J. Astrom and B. Wittenmark, *Adaptive Control*, 2nd ed. Addison-Wesley, 1995.

[19] G. Goodwin, P. Ramadge, and P. Caines, "Discrete-time multivariable adaptive control," *IEEE Trans. Autom. Contr.*, vol. 25, no. 3, pp. 449–456, 1980.

[20] J. B. Hoagg and D. S. Bernstein, "Nonminimum-Phase Zeros: Much to Do about Nothing," *IEEE Control Systems Magazine*, vol. 27, no. June, pp. 45–57, 2007.

[21] K. J. Åström, P. Hagander, and J. Sternby, "sampled systems," *Automatica*, vol. 20, no. 1, pp. 31–38, 1984.

[22] R. Venugopal and D. Bernstein, "Adaptive disturbance rejection using ar-markov/toeplitz models," in *Proceedings of the 1997 American Control Conference (Cat. No.97CH36041)*, vol. 3, 1997, pp. 1657–1661 vol.3.

[23] Y. Rahman, A. Xie, and D. S. Bernstein, "Retrospective Cost Adaptive Control: Pole Placement, Frequency Response, and Connections with LQG Control," *IEEE Control Systems Magazine*, vol. 37, no. October, pp. 85–121, 2017.

[24] N. Mohseni and D. S. Bernstein, "Retrospective cost adaptive harmonic disturbance rejection using dereverberated target models," in *Proceedings of the 2021 American Control Conference (ACC)*, 2021, pp. 2449–2454.

[25] ——, "Retrospective cost adaptive harmonic disturbance rejection using dereverberated target models," *Journal of Sound and Vibration*, vol. 523, 2022.

[26] ——, "Retrospective-cost-based model reference adaptive control of nonminimum-phase systems," *Proceedings of the 2023 American Control Conference*, 2023.

[27] ——, "Retrospective-cost-based model reference adaptive control of nonminimum-phase systems," *International Journal of Adaptive Control and Signal Processing*, Submitted.

[28] T. Leman, E. Xargay, G. Dullerud, N. Hovakimyan, and T. Wendel, "L1 adaptive control augmentation system for the X-48B aircraft," *Proc. AIAA Guid. Nav. Contr. Conf.*, 2012.

[29] Z. T. Dydek, A. M. Annaswamy, and E. Lavretsky, "Adaptive control of quadrotor UAVs: A design trade study with flight evaluations," *IEEE Trans. Contr. Syst. Tech.*, vol. 21, no. 4, pp. 1400–1406, 2013.

[30] G. Chowdhary, H. A. Kingravi, J. P. How, and P. A. Vela, "Bayesian nonparametric adaptive control using gaussian processes," *IEEE Trans. Neural Networks Learning Sys.*, vol. 26, no. 3, pp. 537–550, 2015.

[31] Z. T. Dydek, A. M. Annaswamy, and E. Lavretsky, "Adaptive control and the nasa x-15-3 flight revisited," *IEEE Control Systems Magazine*, vol. 30, no. 3, pp. 32–48, 2010.

[32] T. W. Nguyen, S. A. U. Islam, D. S. Bernstein, and I. V. Kolmanovsky, "Predictive cost adaptive control: A numerical investigation of persistency, consistency, and exigency," *IEEE Control Systems Magazine*, vol. 41, no. 6, pp. 64–96, 2021.

[33] N. Mohseni, T. W. Nguyen, S. A. Ul Islam, I. V. Kolmanovsky, and D. S. Bernstein, "Active noise control for harmonic and broadband disturbances using rls-based model predictive control," in *Am. Control Conf.*, 2020, pp. 1393–1398.

[34] E. F. Camacho and C. Bordons, *Model Predictive Control*, 2nd ed. Springer, 2007.

[35] W. Kwon and S. Han, *Receding Horizon Control: Model Predictive Control for State Models*. Springer, 2006.

[36] J. B. Rawlings, D. Q. Mayne, and M. M. Diehl, *Model Predictive Control: Theory, Computation, and Design*, 2nd ed. Nob Hill Publishing, LLC, 2017.

[37] S. V. Raković and W. S. Levine, *Handbook of Model Predictive Control*. Birkhäuser, 2019.

[38] J. A. Rossiter, *Model-Based Predictive Control: A Practical Approach*. CRC, 2017.

[39] A. H. Sayed, *Fundamentals of Adaptive Filtering*. New Jersey: Wiley, 2003.

[40] L. Ljung, *System Identification: Theory for the User*. USA: Prentice-Hall, Inc., 1986.

[41] A. Goel, A. L. Bruce, and D. S. Bernstein, "Recursive least squares with variable-direction forgetting: Compensating for the loss of persistency [lecture notes]," *IEEE Control Systems Magazine*, vol. 40, no. 4, pp. 80–102, 2020.

[42] T. Fortescue, L. Kershenbaum, and B. Ydstie, "Implementation of self-tuning regulators with variable forgetting factors," *Automatica*, vol. 17, no. 6, pp. 831–835, 1981.

[43] S.-H. Leung and C. So, "Gradient-based variable forgetting factor rls algorithm in time-varying environments," *IEEE Transactions on Signal Processing*, vol. 53, no. 8, pp. 3141–3150, 2005.

[44] L. Ljung and T. Söderström, *Theory and Practice of Recursive Identification*, ser. The MIT Press Series in Signal Processing, Optimization, and Control. MIT Press, 1983, no. 4.

[45] A. L. Bruce, A. Goel, and D. S. Bernstein, "Convergence and consistency of recursive least squares with variable-rate forgetting," *Automatica*, vol. 119, p. 109052, 2020.

[46] C. Elisei-Iliescu, C. Paleologu, J. Benesty, C. Stanciu, C. Anghel, and S. Ciochină, "A decomposition-based rls algorithm with variable forgetting factors," in *13th International Conference on Communications*, 2020, pp. 43–48.

[47] H. Shin and H. Lee, "A new exponential forgetting algorithm for recursive least-squares parameter estimation," *CoRR*, vol. abs/2004.03910, 2020.

[48] S. Drašković, Ž. Durović, and V. Petrović, "Absolute finite differences based variable forgetting factor rls algorithm," *IET Signal Processing*, vol. 16, no. 1, pp. 80–91, 2022.

[49] N. Mohseni and D. S. Bernstein, "Recursive least squares with variable-rate forgetting based on the f-test," in *2022 American Control Conference (ACC)*, 2022, pp. 3937–3942.

[50] S. A. U. Islam, T. W. Nguyen, I. V. Kolmanovsky, and D. S. Bernstein, "Data-driven retrospective cost adaptive control for flight control applications," *Journal of Guidance, Control, and Dynamics*, vol. 44, no. 10, pp. 1732–1758, 2021.

[51] N. Mohseni and D. S. Bernstein, "Predictive cost adaptive control of flexible structures with harmonic and broadband disturbances," in *2022 American Control Conference (ACC)*, 2022, pp. 3198–3203.

[52] N. Mohseni, D. S. Bernstein, and M. B. Quadrelli, "Adaptive force control for small celestial body sampling," in *2022 American Control Conference (ACC)*, 2022, pp. 2515–2520.

[53] ——, "Adaptive force control for small celestial body sampling," in *Journal of Guidance Navigation and Control*, Submitted.

[54] S. A. U. Islam and D. S. Bernstein, "Recursive Least Squares for Real-Time Implementation," *IEEE Control Systems Magazine*, vol. 39, no. 3, pp. 82–85, 2019.

[55] J. J. McKeon, "F approximations to the distribution of Hotelling's T_0^2," *Biometrika*, vol. 61, no. 2, pp. 381–383, 08 1974.

[56] S. Dai, Z. Ren, and D. S. Bernstein, "Adaptive control of nonminimum-phase systems using shifted laurent series," *International Journal of Control*, vol. 90, pp. 409–422, 2017.

[57] D. G. MacMartin and S. R. Hall, "Broadband control of flexible structures using statistical energy analysis concepts," *Journal of Guidance, Control, and Dynamics*, vol. 17, pp. 361–369, 1994.

[58] E. Skudrzyk, "The mean-value method of predicting the dynamic response of complex vibrators," *Journal of the Acoustical Society of America*, vol. 67, pp. 1105–1135, 1980.

[59] A. S. Purekar and D. J. Pines, "Detecting damage in non-uniform beams using the dereverberated transfer function response," *Smart Materials and Structures*, vol. 9, pp. 429–444, 2000.

[60] J. Ma and D. J. Pines, "Concept of dereverbation and its application to damage detection in civil structures," in *Proceedings SPIE*, vol. 3988, 2000, pp. 127 – 134.

[61] K. Matsuda and H. A. Fujii, "Analysis of the dereverberated transfer function in finite dimensions," *Journal of Guidance, Control, and Dynamics*, vol. 19, pp. 91–98, 1996.

[62] D. G. Mac Martin and S. R. Hall, "Control of uncertain structures using an H(infinity) power flow approach," *Journal of Guidance, Control, and Dynamics*, vol. 14, no. 3, pp. 521–530, 1991.

[63] C. H. Hodges and J. Woodhouse, "Theories of noise and vibration transmission in complex structures," *Reports on Progress in Physics*, vol. 49, pp. 107–170, 1986.

[64] M. Sidman, F. Verghese, and D. G.C., "Parametric system identification on logarithmic frequency response data," *IEEE Transactions on Automatic Control*, vol. 36, pp. 1065–1070, 1991.

[65] T. McKelvey, H. Akcay, and L. Ljung, "Subspace-based multivariable system identification from frequency response data," *IEEE Trans. Autom. Contr.*, vol. 41, no. 7, pp. 960–979, Jul 1996.

[66] H. Elliott, R. Cristi, and M. Das, "Global stability of adaptive pole placement algorithms," *IEEE Transactions on Automatic Control*, vol. 30, no. 4, pp. 348–356, 1985.

[67] H. Elliott, "Direct Adaptive Pole Placement with Application to Nonminimum Phase Systems," *IEEE Transactions on Automatic Control*, vol. 27, no. 3, pp. 720–722, 1982.

[68] D. Janecki, "Stability analysis of elliott's direct adaptive pole placement," *Systems & Control Letters*, vol. 11, no. 1, pp. 19–26, 1988.

[69] A. Pyrkin, R. Ortega, V. Gromov, A. Bobtsov, and A. Vedyakov, "A globally convergent direct adaptive pole-placement controller for nonminimum phase systems with relaxed excitation assumptions," *International Journal of Adaptive Control and Signal Processing*, vol. 33, no. 10, pp. 1491–1505, 2019.

[70] S. A. U. Islam, T. W. Nguyen, I. V. Kolmanovsky, and D. S. Bernstein, "Data-driven retrospective cost adaptive control for flight control applications," *AIAA J. Guid. Contr. Dyn.*, vol. 44, no. 10, pp. 1732–1758, 2021.

[71] J. B. Hoagg and D. S. Bernstein, "Retrospective cost model reference adaptive control for nonminimum-phase discrete-time systems, part 1: The adaptive controller," *Proceedings of the 2011 American Control Conference*, pp. 2933–2938, 2011.

[72] ——, "Retrospective cost model reference adaptive control for nonminimum-phase discrete-time systems, part 2: Stability analysis," *Proc. Amer. Contr. Conf.*, pp. 2927–2932, 2011.

[73] ——, "Retrospective Cost Model Reference Adaptive Control for Nonminimum-Phase Systems," *AIAA J. Guid. Contr. Dyn.*, vol. 35, pp. 1767–1786, 2012.

[74] G. W. Snedecor, *Statistical Methods*, 4th ed. Wiley, 1948.

[75] R. Mickey and A. C. Rencher, *Methods of Multivariate Analysis*. Wiley, 1998, vol. 93, no. 443.

[76] R. R. Rhinehart, "Automated steady and transient state identification in noisy processes," in *American Control Conference*, 2013, pp. 4477–4493.

[77] U. Forssell and L. Ljung, "Closed-loop identification revisited," *Automatica*, vol. 35, no. 7, pp. 1215–1241, 1999.

[78] K. F. Aljanaideh and D. S. Bernstein, "Closed-loop identification of unstable systems using noncausal FIR models," *Int. J. Contr.*, vol. 90, no. 2, pp. 168–185, 2017.

[79] F. Sobolic, K. F. Aljanaideh, and D. S. Bernstein, "A numerical investigation of direct and indirect closed-loop architectures for estimating nonminimum-phase zeros," *Int. J. Contr.*, vol. 93, no. 6, pp. 1251–1265, 2020.

[80] L. Ljung, "Prediction Error Estimation Methods," *Circ., Sys. Sig. Proc.*, vol. 21, no. 1, pp. 11–21, 2002.

[81] D. J. McTavish and P. C. Hughes, "Modeling of linear viscoelastic space structures," *Journal of Vibration and Acoustics, Transactions of the ASME*, vol. 115, no. 1, pp. 103–110, 1993.

[82] T. R. Sutter and H. G. Bush, "A Comparison of Two Trusses for the Space Station Structure," NASA, Tech. Rep. March, 1989.

[83] B. Acikmese, M. Quadrelli, and L. Phan, "A force control algorithm for small celestial body surface sampling," *AIAA Guid. Nav. Contr. Conf.*, pp. 1–15, 2007.

[84] J. Brewer, "Kronecker products and matrix calculus in system theory," *IEEE Transactions on Circuits and Systems*, vol. 25, no. 9, pp. 772–781, 1978.

[85] P. Flores, "Compliant contact force approach for forward dynamic modeling and analysis of biomechanical systems," *Procedia IUTAM*, vol. 2, pp. 58–67, 2011.

[86] K. H. Hunt and F. R. E. Crossley, "Coefficient of Restitution Interpreted as Damping in Vibroimpact," *Journal of Applied Mechanics*, vol. 42, no. 2, pp. 440–445, 1975.

[87] S. R. Schwartz, P. Michel, D. C. Richardson, and H. Yano, "Low-speed impact simulations into regolith in support of asteroid sampling mechanism design i: Comparison with 1-g experiments," *Planetary and Space Science*, vol. 103, pp. 174–183, 2014.

[88] A. M. Castro, A. Qu, N. Kuppuswamy, A. Alspach, and M. Sherman, "A transition-aware method for the simulation of compliant contact with regularized friction," *IEEE Robot. Autom. Lett.*, vol. 5, no. 2, pp. 1859–1866, 2020.

[89] S. Boyd, L. El Ghaoui, E. Feron, and V. Balakrishnan, *Linear Matrix Inequalities in System and Control Theory*. Society for Industrial and Applied Mathematics, 1994. [Online]. Available: https://epubs.siam.org/doi/abs/10.1137/1.9781611970777

[90] M. Grant and S. Boyd, "CVX: Matlab software for disciplined convex programming, version 2.1," http://cvxr.com/cvx, Mar. 2014.

[91] ——, "Graph implementations for nonsmooth convex programs," in *Recent Advances in Learning and Control*, ser. Lecture Notes in Control and Information Sciences, V. Blondel, S. Boyd, and H. Kimura, Eds. Springer-Verlag Limited, 2008, pp. 95–110, http://stanford.edu/~boyd/graph_dcp.html.

[92] Songling Cao and R. Russell Rhinehart, "An efficient method for on-line identification of steady state," *Journal of Process Control*, vol. 5, no. 6, pp. 363–374, 1995.

[93] M. M. Seron, J. H. Braslavsky, and G. C. Goodwin, *Fundamental Limitations in Filtering and Control*. New York: Springer, 1997.